

**TEMPLATE-ASSISTED MULTILAYER ELECTRODEPOSITION:  
AN APPROACH TO TOP-DOWN DESIGNABLE,  
SURFACE/VOLUMETRIC HIERARCHICAL NANOSTRUCTURES**

A Dissertation  
Presented to  
The Academic Faculty

by

Min Soo Kim

In Partial Fulfillment  
of the Requirements for the Degree  
Doctor of Philosophy in the  
School of Electrical and Computer Engineering

Georgia Institute of Technology  
May 2016

**COPYRIGHT 2016 BY MIN SOO KIM**

**TEMPLATE-ASSISTED MULTILAYER ELECTRODEPOSITION:  
AN APPROACH TO TOP-DOWN DESIGNABLE,  
SURFACE/VOLUMETRIC HIERARCHICAL NANOSTRUCTURES**

Approved by:

Dr. Mark G. Allen, Advisor  
School of Electrical and Computer  
Engineering  
*Georgia Institute of Technology*

Dr. Ali Fatih Sarioglu  
School of Electrical and Computer  
Engineering  
*Georgia Institute of Technology*

Dr. Oliver Brand  
School of Electrical and Computer  
Engineering  
*Georgia Institute of Technology*

Dr. Paul A. Kohl  
School of Chemical and Biomolecular  
Engineering  
*Georgia Institute of Technology*

Dr. Albert B. Frazier  
School of Electrical and Computer  
Engineering  
*Georgia Institute of Technology*

Date Approved: [December 9, 2015]

*To my grandfather.*

## ACKNOWLEDGEMENTS

I am honored and thankful to have an opportunity to acknowledge all those who helped me finish this thesis.

First, I would like to thank Dr. Mark Allen for being my advisor. I am very lucky to be exposed to his incredible knowledge and wisdom throughout my doctoral study; he was always there when I needed his intellectual guidance and support.

I would like to thank Dr. Oliver Brand, Dr. Albert Frazier, Dr. Ali Fatih Sarioglu, and Dr. Paul Kohl for serving my thesis committee. I appreciate their advices and comments on my research.

I would like to thank all members of MicroSensors and MicroActuators, both from GaTech and University of Pennsylvania. In particular, I appreciate Dr. Seong-Hyok Kim for inviting me to this wonderful lab. I thank Dr. Jooncheol Kim for being my best friend as well as the very best collaborator. The days we spent together in GaTech cleanroom will never be forgotten. Richard Shafer is the best engineer/technician I know so far; I could not have finished this work without his technical assistances. Dr. Florian Herrault and Dr. Jungkwun Kim's managements on the GaTech/UPenn labs have been critical for successfully finishing my research. It has been a great pleasure to have everyone as my colleague, although I cannot list them all one by one.

I would like to thank Dr. Pil-Sung Cho and Gaoxiang Wu at UPenn. They were kind enough to let me use some of their tools that were indispensable for my research.

I would like to thank all my friends I met during this 5 years of study; in particular, I would like to give a big hug to the members of Hypen-Nine.

Finally, my deepest appreciation goes to my parents, grandparents, and my sister for their support, sacrifice, and love.

## TABLE OF CONTENTS

|  | Page |
|--|------|
| LIST OF TABLES   | ix   |
| LIST OF FIGURES  | x    |
| LIST OF SYMBOLS  | xiii |
| LIST OF ABBREVIATIONS  | xv   |
| SUMMARY  | xvi  |
| <br><u>CHAPTER</u>   |      |
| 1 INTRODUCTION   | 1    |
| 1.1 Motivation   | 1    |
| 1.2 Top-Down/Top-Down Fabrication Approaches                 | 6    |
| 1.3 Bottom-Up/Bottom-Up Fabrication Approaches               | 9    |
| 1.4 Hybrid Fabrication Approaches                            | 11   |
| 1.5 Hybrid Approaches Based on Multilayer Electrodeposition  | 14   |
| 1.6 Research Objective and Organization of the Thesis        | 16   |
| 2 TEMPLATE-ASSISTED MULTILAYER ELECTRODEPOSITION (TAME)      | 18   |
| 2.1 Process Overview   | 18   |
| 2.2 Multilayer Electrodeposition for TAME Process            | 23   |
| 2.2.1 Automated Dual-Bath Electrodeposition of Nickel/Copper | 23   |
| 2.2.2 Deposition Parameters and Deposition Baths             | 28   |
| 2.2.3 Other Conditions                                       | 30   |
| 2.2.4 Examples of Fabricated Multilayers                     | 32   |
| 2.3 Multilayer Growth Modeling                               | 37   |
| 2.3.1 Ideal Growth Model                                     | 37   |

|       |  |    |
|-------|--|----|
| 2.3.2 | Growth Modeling Using Morphological Dilation                           | 39 |
| 2.3.3 | Non-Ideal Deposition   | 42 |
| 2.4   | Summary  | 46 |
| 3     | TAME-BASED SURFACE HIERARCHICAL STRUCTURES                             | 47 |
| 3.1   | Backgrounds and Motivation   | 47 |
| 3.2   | Structures Based on Three-Dimensional Electrodeposition                | 48 |
| 3.3   | Application: Nanoscale Pattern Transfer                                | 55 |
| 3.2.1 | Backgrounds and Motivation   | 55 |
| 3.2.2 | Nanoimprinting   | 56 |
| 3.2.3 | Replica Molding  | 60 |
| 3.3.4 | Summary  | 66 |
| 3.4   | Application: Superhydrophobic Surfaces                                 | 66 |
| 3.4.1 | Backgrounds and Motivation   | 66 |
| 3.4.2 | Design and Fabrication   | 70 |
| 3.4.3 | Role of Structural Hierarchy on Non-Wetting Properties                 | 72 |
| 3.4.4 | PDMS Superhydrophobic Surfaces with Uncompromised Optical Transparency | 78 |
| 3.4.5 | Improved Hydrophobicity of Silane-Treated Metallic TAME Structures     | 81 |
| 3.5   | Summary  | 83 |
| 4     | TAME-BASED VOLUMETRIC STRUCTURES: NANOLAMINATIONS                      | 85 |
| 4.1   | Backgrounds and Motivation   | 85 |
| 4.2   | Nanolamination Process   | 90 |
| 4.2.1 | TAME Process and Polymer Anchor Fabrication                            | 90 |
| 4.2.2 | Selective Copper Removal and Sample Drying                             | 93 |
| 4.2.3 | Polymer Infiltration Processes   | 99 |

|   |     |
|---|-----|
| 4.3 Application: Magnetic Materials for High Frequency High Flux Operation                  | 104 |
| 4.3.1 Electrical Characterization of the Inductors With Various Interlamination Insulations | 104 |
| 4.3.2 High Frequency High Flux (HFHF) Inductor Characterization and Loss Analysis           | 110 |
| 4.4 Summary   | 115 |
| 5 TAME-BASED MICRODEVICE: INTEGRATED ON-CHIP MICROINDUCTORS WITH LAMINATED CORES            | 116 |
| 5.1 Backgrounds and Motivation  | 116 |
| 5.2 Monolithic Integration of Microwindings and Laminated Cores                             | 117 |
| 5.3 Design and Fabrication  | 120 |
| 5.3.1 Inductor Design   | 120 |
| 5.3.2 Materials   | 121 |
| 5.3.3 Fabrication Process   | 122 |
| 5.3.4 Fabrication Results   | 125 |
| 5.4 Inductor Characterization   | 127 |
| 5.5 Summary   | 133 |
| 6 CONCLUSION  | 135 |
| 6.1 Summary of Conducted Research   | 135 |
| 6.2 Suggestions for Future Research   | 137 |
| 6.2.1 Patterning in Smaller Scale   | 137 |
| 6.2.2 Improving Structural Diversity with Extended TAME Process                             | 138 |
| 6.2.3 Other Pattern Transfer Techniques   | 141 |
| 6.2.4 Potential Applications  | 141 |
| REFERENCES  | 144 |



## LIST OF TABLES

|  | Page |
|--|------|
| Table 1.1: Micro- and nanofabrication techniques   | 3    |
| Table 1.2: Fabrication approaches to hierarchical structures: Top-down/top-down, bottom-up/bottom-up, and hybrid | 3    |
| Table 1.3: Fabrication and structural details of various hierarchical structures                                 | 5    |
| Table 2.1: Studies on dual-bath electrodeposition  | 24   |
| Table 2.2: Composition of electrodeposition baths  | 28   |
| Table 3.1: Mechanical properties of soft and hard PDMS   | 63   |
| Table 3.2: Calculated static angle using Wenzel and Cassie model   | 75   |
| Table 5.1: Specification of the inductors  | 132  |
| Table 6.1: Achievable TAME structures and their functionalities  | 142  |

## LIST OF FIGURES

|   | Page |
|---|------|
| Figure 1.1: Top-down/top-down fabrication approaches  | 7    |
| Figure 1.2: Bottom-up/bottom-up approaches  | 10   |
| Figure 1.3: Hybrid approaches   | 12   |
| Figure 1.4: Superlattice nanowire pattern transfer  | 15   |
| Figure 1.5: Thesis outline  | 17   |
| Figure 2.1: Schematic illustration for TAME-based processes   | 19   |
| Figure 2.2: Automated, dual-bath multilayer electrodeposition system  | 27   |
| Figure 2.3: AFM and SEM images of the multilayers fabricated based on different copper electrolytes   | 31   |
| Figure 2.4: Thick multilayers   | 32   |
| Figure 2.5: Multilayers with the thinnest individual layers   | 34   |
| Figure 2.6: Multilayers with multiscale periodicities   | 35   |
| Figure 2.7: Pictorial depiction of the multilayer growth modeling ( $n=3$ )   | 38   |
| Figure 2.8: Original SEM images for modeling  | 39   |
| Figure 2.9: Image processing using Figure 2.8(b)  | 40   |
| Figure 2.10: Comparison between $I_n$ (light green) and $A_n$ (red) for both images, Figure 2.8 (b), (c)  | 41   |
| Figure 2.11: Spatiotemporal characteristics of multilayer growth  | 43   |
| Figure 2.12: Cross-sectional SEM image of a multiscale multilayer structure   | 44   |
| Figure 3.1: Surface structures fabricated based on electrodeposited multilayers   | 48   |
| Figure 3.2: TAME process based on three-dimensional multilayer electrodeposition  | 49   |
| Figure 3.3: Widths of the growth rings as a function of individual layer deposition time; etched copper thickness as a function of etching time | 51   |

|  |    |
|--|----|
| Figure 3.4: Planar surface relief structures based on TAME process using a Type 1 template             | 52 |
| Figure 3.5: Non-planar TAME structures   | 53 |
| Figure 3.6: Vertically-aligned nanowalls   | 54 |
| Figure 3.7: Thermal nanoimprinting   | 57 |
| Figure 3.8: Room temperature nanoimprinting  | 59 |
| Figure 3.9: PDMS molding using planar TAME structures  | 61 |
| Figure 3.10: Molding results with conventional soft PDMS and h-PDMS                                    | 63 |
| Figure 3.11: AFM scan of dual-scale h-PDMS structures  | 65 |
| Figure 3.12: Examples of superhydrophobic surfaces   | 68 |
| Figure 3.13: Superhydrophobic structures prepared in this experiment                                   | 71 |
| Figure 3.14: A droplet in Wenzel and Cassie states   | 73 |
| Figure 3.15: Static contact angle comparison between planar, single-scale, and hierarchical structures | 75 |
| Figure 3.16: Contact angle hysteresis  | 76 |
| Figure 3.17: Contact angle hysteresis measured from a hierarchical structure                           | 77 |
| Figure 3.18: SCA and CAH of various h-PDMS structures with different designs                           | 79 |
| Figure 3.19: UV-vis spectroscopy of the samples with different nanostructure fill-factors              | 80 |
| Figure 3.20: Wetting properties of TFOCS-treated metallic TAME structures                              | 82 |
| Figure 4.1: Magnetic materials exposed to a time varying magnetic field                                | 86 |
| Figure 4.2: Transformer built from Westinghouse, circa 1885  | 86 |
| Figure 4.3: Examples of the state-of-the-art lamination processes                                      | 87 |
| Figure 4.4: Polymer anchoring process  | 91 |
| Figure 4.5: Selective copper removal   | 93 |
| Figure 4.6: Cross-section view of a multilayer sidewall after the SU-8 anchoring                       | 94 |

|  |     |
|--|-----|
| Figure 4.7: <i>In-situ</i> weight measurement result for 9 samples with different designs  | 95  |
| Figure 4.8: Multilayers packaged into the polymeric bobbins, forming inductors   | 96  |
| Figure 4.9: <i>In-situ</i> electrical measurement result for a multilayer sample   | 98  |
| Figure 4.10: Parylene-deposited, air-insulated laminations   | 99  |
| Figure 4.11: PVA-infiltrated laminations   | 100 |
| Figure 4.12: PDMS-infiltrated laminations  | 102 |
| Figure 4.13: Inductor under an impedance measurement   | 106 |
| Figure 4.14: Measured normalized core inductance of fabricated laminated structures and its theoretical calculation for various lamination thicknesses, at 5 MHz | 108 |
| Figure 4.15: Characterization of two inductors at 2 mT   | 109 |
| Figure 4.16: Schematic of the high flux measurement setup  | 110 |
| Figure 4.17: Measured volumetric core loss of a sample   | 113 |
| Figure 5.1: Definition of winding density and core fill-factor   | 118 |
| Figure 5.2: Drop-in core integration   | 118 |
| Figure 5.3: Inductor design  | 121 |
| Figure 5.4: Fabrication sequence   | 124 |
| Figure 5.5: SEM pictures of the fabricated samples   | 128 |
| Figure 5.6: Optical images of the integrated inductors   | 127 |
| Figure 5.7: Inductance and $Q$ of a pair of integrated inductors sharing the same laminated core   | 128 |
| Figure 5.8: Inductor resistance versus the sample immersion time in the copper etchant   | 131 |
| Figure 6.1: Extended TAME process based on a seed layer with initially isolated conductors   | 139 |
| Figure 6.2: Isotropic nickel structures formed by an extended TAME process   | 140 |

## LIST OF SYMBOLS

|            |  |                                 |
|------------|--|---------------------------------|
| $w_{Ni}$   |  | Width of a Nickel Layer         |
| $w_{Cu}$   |  | Width of a Copper Layer         |
| $t_{Ni}$   |  | Thickness of a Nickel Layer     |
| $t_{Cu}$   |  | Thickness of a Copper Layer     |
| $n$        |  | Sequence of Deposition          |
| $G_{Ni}$   |  | Estimated Growth Rate of Nickel |
| $G_{Cu}$   |  | Estimated Growth Rate of Copper |
| $I_n$      | Modeled Growth Ring of the Deposited Multilayer at $n$ th Deposition |                                 |
| $A_n$      |  | Modeled Growth Ring             |
| $p$        |  | Periodicity of a Multilayer     |
| $w$        | Width of a Protrusion within a Surface Relief Structure              |                                 |
| $g$        | Width of a Trench within a Surface Relief Structure                  |                                 |
| $h$        | Etched Groove Depth of a Surface Relief Structure                    |                                 |
| $\theta_0$ |  | Young's Angle                   |
| $\theta^w$ | Static Contact Angle based on Wenzel Model                           |                                 |
| $\theta^c$ | Static Contact Angle based on Cassie Model                           |                                 |
| $\theta_a$ |  | Advancing Angle                 |
| $\theta_r$ |  | Receding Angle                  |
| $\delta$   |  | Skin depth                      |
| $\omega$   |  | Angular Frequency               |
| $\mu_0$    |  | Permeability of Vacuum          |
| $\mu_r$    |  | Relative Permeability           |

|                     |   |
|---------------------|---|
| $\sigma$            | Electrical Conductivity                           |
| $L$                 | Total Inductance Measured From an Inductor        |
| $R$                 | Total Resistance Measured From an Inductor        |
| $L_{\text{core}}$   | Core Inductance                                   |
| $L_{\text{air}}$    | Air-Core Inductance                               |
| $R_{\text{core}}$   | Core Resistance                                   |
| $R_{\text{air}}$    | Air-Core Resistance                               |
| $L_{\text{n,meas}}$ | Normalized Core Inductance                        |
| $L_{\text{n,theo}}$ | Theoretical Value of a Normalized Core Inductance |
| $2b$                | Thickness of a Magnetic Layer                     |
| $N$                 | Number of Turns                                   |
| $C$                 | Capacitance                                       |
| $R_c$               | Parasitic Resistance of a Capacitor               |
| $P_{\text{core}}$   | Magnetic Core Power Loss                          |
| $P_{\text{v,core}}$ | Core Loss Per Volume                              |
| $B_{\text{core}}$   | Magnetic Flux Density within a Core Material      |

## LIST OF ABBREVIATIONS

|        |  |
|--------|--|
| EBL    | Electron Beam Lithography                      |
| FIB    | Focused Ion Beam                               |
| SEM    | Scanning Electron Microscope                   |
| CFL    | Capillary Force Lithography                    |
| AFM    | Atomic Force Microscopy                        |
| GMR    | Giant Magnetoresistance                        |
| SNAP   | Superlattice Nanowire Pattern Transfer         |
| TAME   | Template Assisted Multilayer Electrodeposition |
| MEMS   | Microelectromechanical Systems                 |
| s-PDMS | Soft Polydimethylsiloxane                      |
| h-PDMS | Hard Polydimethylsiloxane                      |
| SCA    | Static Contact Angle                           |
| CAH    | Contact Angle Hysteresis                       |

## SUMMARY

A versatile nanofabrication technology that enables scalable, yet controllable realization of multiscale (20 nm~1  $\mu\text{m}$ ), multidimensional structures without the use of standard nanolithography (e.g. electron-beam lithography) is developed, and its utility is validated through selected example applications.

Driven by the emerging interest in the design and realization of structures with co-existing micro- and nanoscale features, various nanofabrication approaches are being developed. We show that the selective, conformal growth of a multilayer structure is a promising route for the controlled realization of various structures with size-hierarchy, including both surface structures (i.e. the structures of which functionalities are characterized by the interaction between their surface and external systems, such as self-cleaning, superhydrophobic substrates with dual-scale topography), and volumetric structures (i.e. composite materials of which functionalities rely on the intrinsic properties of nanostructures distributed throughout their volume, such as giantmagneto-resistance sensors).

This concept is realized based on a sequential multilayer electrodeposition guided by an insulating substrate with predesigned topography (i.e. template), referred to as the template-assisted multilayer electrodeposition (TAME) process. In order to validate the utility of the TAME-based nanofabrication approaches, several key tasks are accomplished. First, a theoretical model for the TAME process is developed. By assuming a constant, isotropic growth of multilayers, the final TAME structures can be predicted from initial process parameters. Second, various multiscale, multidimensional surface and volumetric



hierarchical structures are demonstrated of which size scale of the nanostructures are defined by the individual layer deposition parameters, while their position and overall geometries are defined by the template. These structures include (1) large area ( $> 1 \text{ cm}^2$ ), planar, or non-planar surfaces comprised of anisotropic, nanoscale surface relief structures of wide-ranging size scale ( $10 \text{ nm} \sim 1 \text{ }\mu\text{m}$ ); and (2) thick ( $10 \sim 100 \text{ }\mu\text{m}$ ), volumetric composite material in which individual metallic layers of micron, or submicron scale thicknesses are electrically insulated from the adjacent layers by interlamination insulating layers of similar thicknesses, i.e., nanolaminations.

The utility of the fabricated structures is evaluated in a few potential application domains, i.e., nanolithography, non-wetting surfaces, and magnetics. First, nanoscale pattern transfer techniques are demonstrated using TAME-based, planar surface reliefs as master molds. The patterns achieved within the metallic TAME structures can be transferred to desired materials (i.e. polymer resins, silicon substrate). Second, superhydrophobic surfaces are demonstrated using the TAME-based, non-planar surface reliefs. Based on a single-step replica molding from the TAME-structures, an economic fabrication of dual-scale, elastomeric surface structures is enabled. The fabricated structures exhibit superhydrophobicity that results from their structural hierarchy. Third, inductors are realized using the nanolaminations as a magnetic core material. The nanolaminated magnetic cores are operated at high frequency ( $> 1 \text{ MHz}$ )/high magnetic flux ( $> 0.1 \text{ T}$ ) while the eddy current losses being completely suppressed, showing a potential for DC-DC switched mode, miniaturized converter application. In addition, a monolithic fabrication procedure is developed to enable a co-fabrication of microwindings

and laminated cores on a single substrate; a TAME-based device, i.e., fully-miniaturized, integrated microinductors, is presented and characterized.

The principal contributions of this work include: the demonstration of a scalable, yet controllable nanofabrication technology that does not rely on standard nanolithography; the demonstration of various structures that can stem from this technology; the usefulness of the fabricated structures in related application areas (i.e. nanofabrication, self-cleaning, magnetics). Further development of the process will lead to an improved versatility, stimulating the nanoapplication researches in the field of electrochemistry (e.g. battery, supercapacitor), optics (e.g. subwavelength gratings, X-ray diffraction grating), biology (e.g. directed cell growth), mechanics (e.g. compliant electrodes), and thermodynamics (e.g. boiling heat transfer).

# CHAPTER 1

## INTRODUCTION

### 1.1 Motivation

Size-hierarchical structures, in which micro- and nanoscale structures coexist, have been of great interest due to their distinct structural properties that cannot be extrapolated from structures of singular scale. The nanostructures (defined here as structures of characteristic size along at least one axis that is smaller than 1  $\mu\text{m}$ ) are mainly responsible for the desired properties, while the microstructures (that are larger than the nanostructures) provide mechanical support for the nanostructures, as well as define the overall geometry of the systems, and thereby, “bridge” between the nano- and macroscale structures.

In general, size-hierarchical structures can be categorized into two types. The first is referred to as surface hierarchical structures, in which properties can be characterized by physical/optical/chemical interaction between the “surface” of the devices and external systems, e.g., liquid droplets, light, and electrolytes. The structures that exhibit self-cleaning [1], surface enhanced Raman scattering [2], and amplified electrochemical energy storage capacity due to high surface-to-volume ratio [3] correspond to this category. The second type is referred to as the volumetric hierarchical structures of which properties result from the combination of the “intrinsic” material characteristics of the individual nanostructures arranged within the volume of larger-scale structures (e.g. giant magnetoresistance based on the periodic arrangement of ferro- and non-magnetic thin films [4] and nacre mimicked mechanical properties using brick-and-mortar architecture [5]), rather than a surface interaction.

To harness such useful properties in an economic manner, a controlled, yet scalable realization of hierarchical structures with desired functional materials is critical. In general, beam-based direct writing techniques (e.g. electron-beam lithography (EBL) and focused ion beam (FIB) lithography) have been regarded as general approaches for creating nanostructured features in a designed manner. These techniques possess an arbitrary pattern generation capability on a planar substrate at the expense of higher equipment complexity and lower throughput. UV photolithography has been a primary method to transfer the “written” patterns to multiple substrates. However, these processes are usually limited in realizing the hierarchical structures of which (1) nanostructures that are smaller than UV wavelengths, (2) structures patterned on non-planar topography, or (3) those extended through the volume of larger-scale structures (e.g. three-dimensional nanostructures with high lateral/vertical aspect ratio). Alternatively, there has been considerable efforts to combine conventional microfabrication (which is still effective in creating the larger-scale structures) with so-called “unconventional” nanofabrication approaches to define hierarchical structures without employing standard nanolithography [5] (Table 1.1). In general, the unconventional nanofabrication approaches are categorized into “top-down” and “bottom-up”. The top-down approaches typically rely on a physical contact between a master stamp and a target material, thereby, achieving a pattern transfer [6-8]. Multiple copies of well-defined, nanoscale structures can be created in batch scale although the fabrication of the stamp may demand the use of standard nanolithography. The realization of three-dimensional structures is rather limited, since a conformal contact between the stamp and the substrate material is required during the patterning processes.

Table 1.1 Micro- and nanofabrication techniques.

| <b>Conventional microfabrication</b>   | <b>Nanofabrication</b>  |   |
|--|---|---|
|  | <b>Conventional</b>   | <b>Unconventional</b>   |
| <ul style="list-style-type: none"> <li>- 1:1 UV photolithography</li> <li>- Replication from microstructures (e.g. injection molding, embossing)</li> <li>- Laser machining</li> <li>- Printing</li> </ul> | <ul style="list-style-type: none"> <li>- Beam-based writing (e.g. electron-beam, focused-ion beam writing)</li> </ul> | <ul style="list-style-type: none"> <li>- Top-down (e.g. nanoimprinting, capillary force lithography, soft lithography)</li> <li>- Bottom-up (e.g. wrinkling, cracking, nanostructure growth)</li> </ul> |

On the contrary, the bottom-up approaches rely on the self-organization of small structural units, such as wrinkles [9], cracks [10], nanowires [11], colloidal spheres [12], and block copolymers [13-15], thereby enabling a facile, economic realization of multidimensional assemblages; however, precise control over the orientation and registration of the individual structures is often difficult due to the stochastic nature of the self-organization processes.

Table 1.2 Fabrication approaches to hierarchical structures: Top-down/top-down, bottom-up/bottom-up, and hybrid.

| <b>Micro \ Nano</b>                | <b>Conventional nanofabrication</b> | <b>Unconventional nanofabrication</b> |                                   |
|------------------------------------|-------------------------------------|---------------------------------------|-----------------------------------|
|                                    |                                     | <b>Top-down</b>                       | <b>Bottom-up</b>                  |
| <b>Conventional micromachining</b> | Top-down/top-down (First type)      |                                       | Hybrid (Third type)               |
| <b>Bottom-up</b>                   | Hybrid (Fourth type)                |                                       | Bottom-up/bottom-up (Second type) |

Upon review, the fabrication procedures reported in the previous literature citations can be categorized into four types (Table 1.2). The first type, “Top-down/top-down”, refers to approaches relying on the use of projection lithography-based, standard microfabrication and the top-down nanofabrication techniques to define micro- and nanostructures, respectively. The second type, “Bottom-up/bottom-up,” relies on self-organization processes to form multiscale structures. The third and fourth type, “hybrid,” combine the advantages of top-down and bottom-up approaches; a bottom-up, self-organization of nanoscale structures is spurred by top-down micromachining (the third type), or vice versa (the fourth type).

Among the studies related to hybrid processes, a larger portion is focused on the third type, since the main motivation of a hybrid process is to create controlled nanostructures without depending on direct writing techniques while simultaneously maintaining much of their design flexibility. Hence, the hybrid processes that are discussed in this thesis are mostly the third type. The examples of surface and volumetric hierarchical structures that are fabricated based on the three types of approaches are shown in Table 1.3. Further details regarding the fabrication approaches is follows in Chapter 1.2.

Table 1.3 Fabrication and structural details of various hierarchical structures.

|                                 |                                    | Microstructures                |   |   | Nanostructures               |   |   | Functionality   |   |
|---------------------------------|------------------------------------|--------------------------------|---|---|------------------------------|---|---|---|---|
|                                 |                                    | Process                        | Materials   | Details   | Process                      | Materials   | Details                                     |   |   |
| Surface hierarchical structures | Top-down/Top-down                  | Microlithography + Replication | Polystyrene (PS), Polymethylmethacrylate (PMMA)     | Grating (Pitch = 4 μm)  | Nanoimprinting               | PS, PMMA  | Grating (Pitch = 500 nm)                    | Anisotropic wetting [16]                                  |   |
|                                 |                                    | Microlithography               | UV-curable polyurethane                             | Pillars (Aspect ratio, AR: 5, Diameter, D: 5 μm)              | Capillary force lithography  | UV-curable polyurethane                             | Slanted pillars (AR: 6, D: 500 nm)          | Dry adhesion [8]  |   |
|                                 | Bottom-up/Bottom-up                | Anisotropic etch               | Silicon   | Pyramidal (D: 1 ~ 10 μm)                                      | Anisotropic etch             | Silicon   | Pyramidal (D > 20 nm)                       | Superhydrophobicity [1]                                   |   |
|                                 |                                    | Spontaneous wrinkling          | Polydimethylsiloxane (PDMS)                         | Sinusoidal groove (Pitch: 1~100 μm)                           | Spontaneous wrinkling        | PDMS  | Sinusoidal groove (Pitch: Down to 100 nm)   | Filtration [9]  |   |
|                                 |                                    | Hydrothermal nanowire growth   | ZnO   | Vertically-grown nanowires (2~8 μm long, 130 nm < D < 200 nm) | Hydrothermal nanowire growth | ZnO   | Nanowires (2~10 μm long, 30 nm < D < 50 nm) | Improved light harvesting [11]                            |   |
|                                 | Hybrid                             | Electrodeposition              | Ni  | Semihemisphere (D~100 μm)                                     | Colloidal assembly           | PS  | Opal (D~500 nm)                             | Battery electrodes with high surface to volume ratio [17] |   |
|                                 |                                    | Projection nanolithography     | Negative photoresist                                | Stripes (Pitch: 1.5 μm)                                       | Block copolymer assembly     | PS-b-PMMA   | Lamellar                                    | optical birefringence [18]                                |   |
|                                 |                                    | Polymer wrinkling              | PDMS  | Sinusoidal groove (Pitch: 10~25 μm)                           | Replica molding in nanoscale | PDMS  | Sinusoidal groove (Pitch: 420, 800, 844 nm) | Potential for anisotropic wetting [19]                    |   |
|                                 | Volumetric hierarchical structures | Bottom-up/Bottom-up            | Self-assembly by exposure to vacuum + sample drying | Aligned montmorillonite                                       | Plate-like bricks            | Self-assembly by exposure to vacuum + sample drying | PVA (polyvinyl alcohol)                     | thin "mortar"   | Nacre-mimicking hardness /strength [5]                  |
|                                 |                                    | Hybrid                         | Wire bonding + Micromachining                       | Au  | Bridge                       | Multilayer electrodeposition                        | Cu/NiFe                                     | Layered structure (Individual thicknesses ~ 100 nm)       | Low conductor loss due to eddy current suppression [20] |

The work presented in this thesis is dedicated to the development of a hybrid approach based on the combination of conventional micromachining and multilayer electrodeposition. This enables a scalable, yet controllable realization of various surface and volumetric hierarchical structures. In the following subchapters, representative top-down/top-down, bottom-up/bottom-up, and hybrid approaches to hierarchical structures are introduced. This leads to the demonstration of the developed hybrid process, which is referred to as “template-assisted multilayer electrodeposition”, or simply TAME.

## **1.2 Top-Down/Top-Down Fabrication Approaches**

A top-down/top-down fabrication procedure typically begins by patterning desired microstructures (i.e. larger-scale structures) on a substrate, based on a conventional micromachining such as 1:1 projection lithography, or replica molding from the lithographically-defined microstructures. Then, the desired nanostructures are defined by a subsequent top-down nanofabrication approach, such as nanoimprinting [6] and capillary force lithography [7, 8]. Nanoimprinting transfers the pattern predefined within a master stamp, to the microstructures by making physical contact with the structures under proper pressure and temperature conditions (Figure 1.1(a)). Figures 1.1(b), (c) show a dual-scale, hierarchical surface structures that exhibit anisotropic wetting (i.e. different wettability with respect to the orthogonal axes); the nanostructures observed in the picture is defined by a nanoimprinting on the pre-defined, microscale polymer grating. Note that the microstructures shown in Figure 1(b) are slightly deformed by the pressure induced by the stamp.



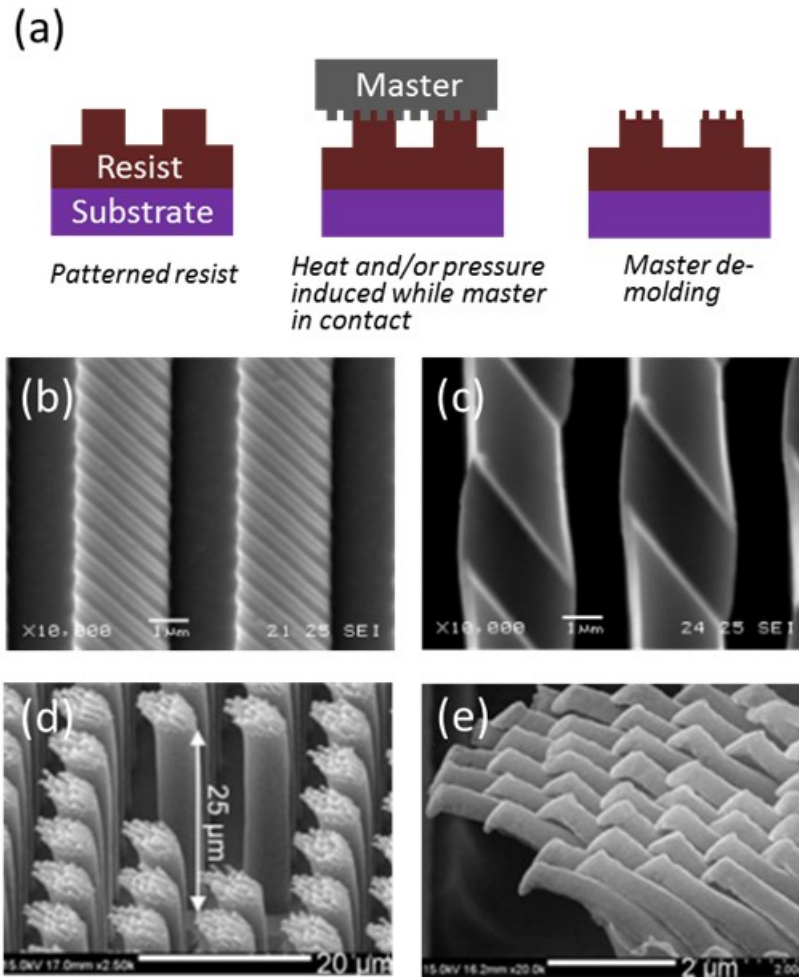


Figure 1.1 Top-down/top-down fabrication approaches [8, 19]. (a) A generalized schematic for top-down/top-down hierarchical structure fabrication procedures. (b), (c) Scanning electron microscope (SEM) images of dual-scale, polymethylmethacrylate (PMMA) nanoimprinted structures. (d), (e) Polyurethane (PU) hierarchical structures of which nanostructures are defined by a UV-assisted capillary force lithography.

To pattern mechanically fragile nanostructures (e.g. pillars and bridges with high aspect ratio) without deforming the predefined microstructures, capillary force lithography (CFL) was developed. The original CFL relies on the capillary force between a “soft” stamp with low surface energy (i.e. polydimethylsiloxane (PDMS) stamp) and a heated thermoplastic resist in its liquid state; the liquid resist is filled within the recessed region of the master without significant pressure being induced to the system. The master is separated after the resist is cooled below the glass transition temperature of the material, leaving the solid, molded nanostructures patterned on the predefined microstructures. A UV-curable photoresist that exhibits a liquid phase even at room temperature, can be used as the resist to alleviate process temperature issues. CFL is utilized to create gecko foot-mimicking dry adhesives comprised of nanoscale, high aspect-ratio (higher than 5:1) “hairs” on pre-defined microscale pillars (Figure 1(d),(e)).

Based on top-down/top-down approaches, both micro- and nanostructures of a desired hierarchical structure can be defined in a controlled manner although the preparation of the master molds still demands the use of conventional nanolithography. In general, top-down/top-down approaches are limited in creating three-dimensional structures. Since typical silicon, or metal imprint stamps are not sufficiently flexible to make conformal contact with non-planar topographies (such as the angled, or rounded topography of pre-defined microstructures), the projection of the nanostructures to such surfaces is difficult. Moreover, the realization of nanostructures with high structural aspect ratios is challenging. The polymer molded into the master can be easily deformed, or even destroyed during the de-molding process due to the low mechanical stiffness of the molded structures.

### 1.3 Bottom-up/Bottom-up Fabrication Approaches

A bottom-up/bottom-up approach relies on the spontaneous self-organization of small building blocks (i.e., molecules, colloids, wrinkles) to construct multiscale structures. By inducing a compressive force against a deformable, composite thin film comprised of a stiff skin and a soft substrate, periodic wrinkles can be produced within the surface of the film. Hierarchical surface structures comprising 4~5 generations of which size scale spans from tens-of-nanometers to hundreds-of-micrometers can be created simultaneously [9]. The structural periodicities of each generation are defined by the thicknesses of the stiff and soft layer and the stiffness ratio between the two layers. Figure 1.2(a), (b) shows an example of such hierarchical structure. A size-dependent particle separation is demonstrated as an application.

Multi-step etching [1], or deposition processes [11] are regarded as bottom-up/bottom processes. A two step, anisotropic potassium hydroxide etching of single crystalline silicon results in hierarchical structures with randomly distributed, micro- and nanoscale pyramids on the substrate (Figure 1.2(c), (d)). The dual-scale structures exhibit superhydrophobicity (i.e., static water contact angle  $> 150^\circ$ , contact angle hysteresis  $< 10^\circ$ ). “Forest-like” multiscale structures are synthesized by a multi-step, hydrothermal process as shown in Figure 2 (e). The first step creates microscale ZnO tree “trunks” while their nanoscale “branches” are formed by subsequent, cyclic processes.

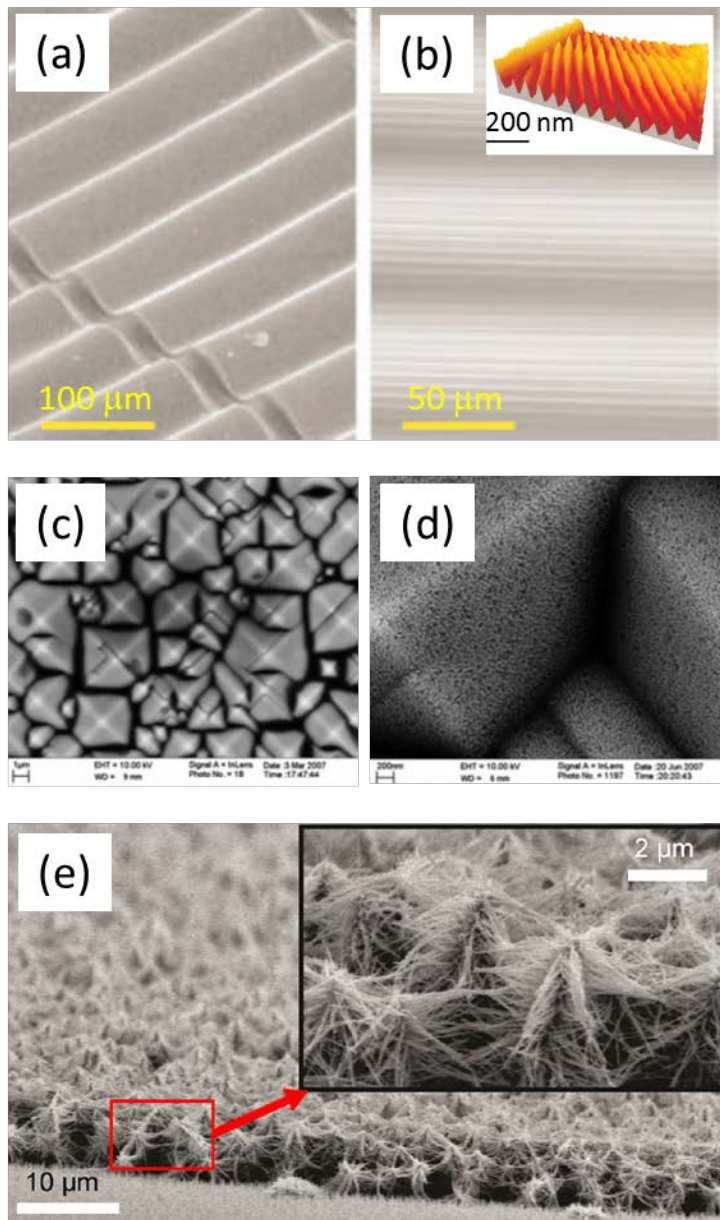


Figure 1.2. Bottom-up/bottom-up approaches. (a), (b) Hierarchical polydimethylsiloxane (PDMS) wrinkles [9]. (b) is a magnified, top-view of (a). The inset is an atomic force microscope (AFM) image of the 4<sup>th</sup> generation wrinkles. (c), (d) Hierarchical surface structures based on two-step silicon etching [1]. (e) Multiscale, ZnO nanoforests [11]. The inset shows the “nanotrees.” Nanoscale “branches” are grown on the tree “trunks.”

These structures are characterized by very high broadband light absorptivity due to their randomly-oriented, multiscale structural nature with high surface-to-volume ratio. Such structures are useful in improving the efficiency of a solar cell.

Compared to top-down approaches, the fabrication procedure for a bottom-up/bottom-up process is simple and easy to scale up. Facile realization of complex, multiscale three-dimensional structures is feasible; however, the orientation and registration of the individual structures through these approaches are difficult to be controlled.

#### **1.4 Hybrid Fabrication Approaches**

A hybrid process combines top-down lithography and bottom-up self-organization to form a hierarchical structure. Unlike the fabrication results of typical bottom-up/bottom-up approaches, the overall geometry and the position of a nanostructure assembly are controlled by top-down micromachining. An inverted opal, bicontinuous metallic structure has been realized by electrodeposition through a predefined mold created by a colloidal assembly [17] (Figure 1.3(a)). While the opal structure is defined by the size and the lattice structure of the assembled particles, the interdigitated electrode design is defined by the geometry of the predefined gold electrodes (Figure 3(b)). This structure is used to as a high surface area electrode for the batteries with rapid charging/discharging rates.

Sequential deposition of two (or more) different materials, combined with top-down micropatterning, results in various volumetric hierarchical structures. A giantmagnetoresistance (GMR) magnetic force sensor is an example [4]. Alternating layers of thin ferromagnetic and nonmagnetic layers may exhibit antiparallel spin alignment due to the exchange coupling between the neighboring ferromagnetic layers. The electrical

resistance of the layered material changes as an external magnetic field alters the spin alignment. Figure 3(c), (d) shows an array of the bar-type sensors of which overall geometries are defined by top-down microlithography.

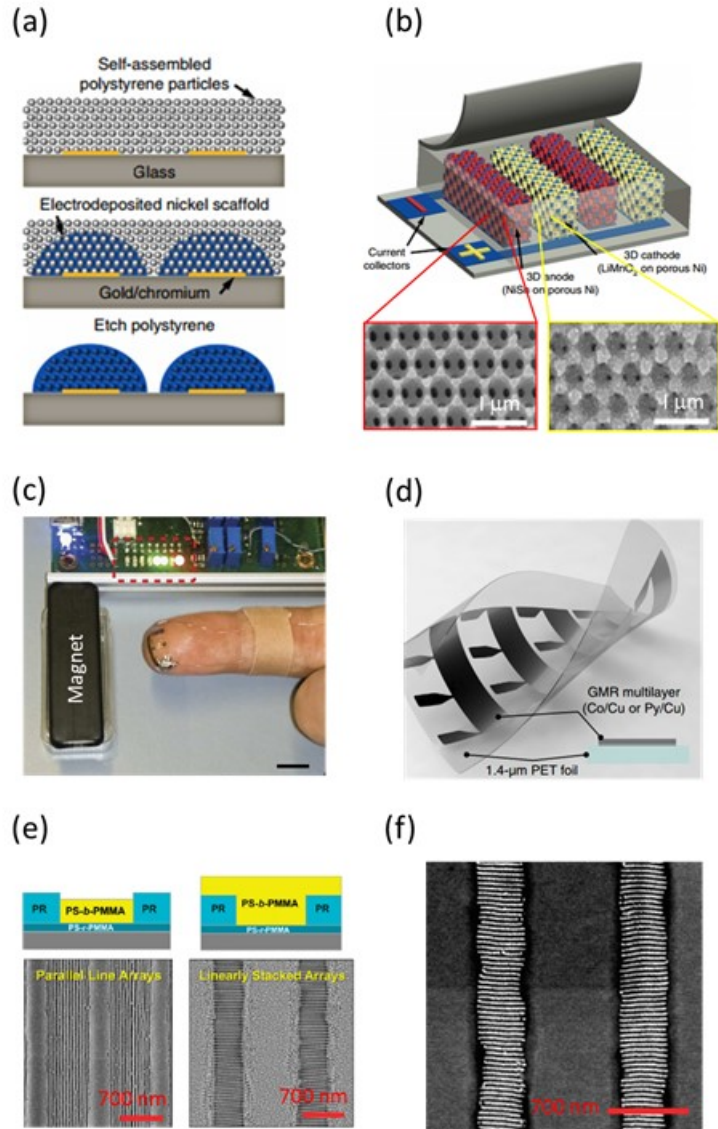


Figure 1.3. Hybrid approaches. (a) Fabrication sequence of the inverted opal electrodes. (b) Overall battery structures [17]. (c) GMR sensor patterned on a polyethylene terephthalate (PET) [4]. As the finger approaches the magnet, the proximity indicator (dotted lines) is lighted. (d) is the schematic of the sensor. (e) Self-ssembled, (Polystyrene-b-Polymethylmethacrylate) block copolymers. (f) is the gold nanowire array created by a lift-off process [18].

In some approaches, the nanostructure self-organization processes are “spurred” by the pre-fabricated microstructures. Block copolymer self-assembly can be controlled by lithographically-defined [13] (or inkjet-printed [21]) templates to achieve structures with designed morphologies (e.g. lamellar, cylinders, gyroids [22]) within selected regions. The surface chemistry of a template is designed to exhibit a stronger affinity to either block of the copolymer, so that a stable boundary condition for an energetically-favorable, yet well-ordered assembly is provided. Figure 3(e) shows that the morphologies of the block-copolymer assemblies can be controlled by changing the height difference between the template and the copolymer film. Well-ordered gold nanowire arrays are fabricated of which microscale periodicity is defined by the template size while the nanoscale periodicity defined by the molecular size of the copolymer blocks (Figure 1.3(f)). Due to the structural hierarchy, a strong optical anisotropy (i.e. polarization-dependent transmittance) is observed from the diffracted light.

In summary, the advantages of top-down/top-down and bottom-up/bottom-up approaches are combined within hybrid approaches. Bottom-up nanofabrication with improved controllability enables the scalable realization of size-controlled hierarchical structures with designed functionalities. Moreover, the integration of such structures into external devices or systems (of which characteristic lengths are usually larger than a micrometer) is relatively straightforward, since the position and overall geometry of the structures are well-defined by standard lithography. However, it should be noted that a single hybrid approach alone does not possess arbitrary pattern generation capability. It is only useful in creating specific types of patterns of which geometries and sizes are closely tied to the bottom-up nanofabrication approach it employs. Hence, a large portion of the

process development effort is dedicated to the improvement of achievable structural and material diversity.

### **1.5 Hybrid Approach Based On Multilayer Electrodeposition**

Traditionally, fabrication of multilayer structures (i.e. structures comprising alternating layers of heterogeneous materials) is regarded as a bottom-up, non-lithographic route to nanostructures. A significant portion of the study has been dedicated to the realization of patterned composites of which useful mechanical [23], optical [24], electromagnetic [4] properties stem from the precisely-controlled, nanoscale structural periodicities. On the other hand, there has been a continuous attempt to translate such structures into nanoscale surface reliefs by cutting and/or polishing various multilayers formed by different techniques (e.g. molecular beam epitaxy [25-28], electrodeposition [29], and sequential sputtering and anodization [30]), and subsequently selectively etching a material from the revealed superlattice structures. Further, a “superlattice nanowire pattern transfer,” or SNAP process is developed [25], where a desired material is deposited on the etched multilayer structures with a proper angle to create isolated nanowires on the protruded portion of the multilayers (Figure 1.4(a)); the deposited wires are transferred to a separate substrate by a subsequent printing process (Figure 1.4(b)). The SNAP process is useful in producing sub-50 nm pitch nanowire structures for many applications (e.g. nanomechanical resonators [25], ring oscillators [27], and chemical sensors [28] (Figure 1.4(c))). Although the achievable size scale and pattern density through this approach are comparable to that of conventional nanolithography based on an electron-beam writer, the achievable structures are usually limited by the simple geometry of the polished multilayer superlattice, i.e., one-dimensional, straight features distributed within a narrow, planar



surface defined by the total thickness of the deposited multilayer which is typically only a few tens of micrometers.

In this study, we demonstrate a hybrid process, template-assisted multilayer electrodeposition (TAME), which significantly improves the achievable structural diversity of multilayer-based approaches. Sequential electrodeposition is selected as the multilayer deposition method primarily because its deposition reaction is highly selective to electrically conductive surfaces and also controllable to form relatively thick ( $>100\ \mu\text{m}$ ) multilayers with nanoscale individual layers of designed thicknesses at room temperature without employing vacuum tools. Combined with a top-down, lithography-based template fabrication, the multilayer electrodeposition leads to the controlled realization of various surface and volumetric hierarchical structures of which nanostructures (10 nm- 1000 nm) are defined by both deposition control and template geometry design.

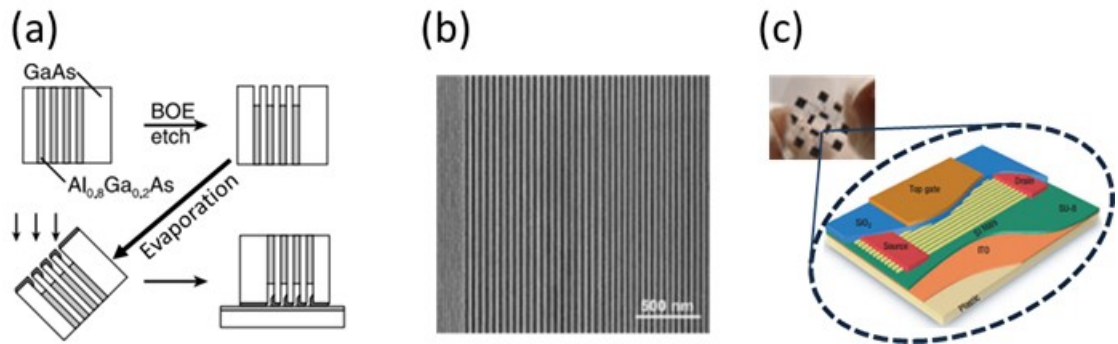


Figure 1.4. Superlattice nanowire pattern transfer. (a) Fabrication sequence using GaAs/AlGaAs multilayers. After the last sequence, the multilayer stack is removed by a wet etch, leaving the patterned, evaporated nanowires on the substrate. (b) SEM image of silicon nanowires; the 40 wires, 20 nm wide with 60 nm pitch. (c) Silicon nanowire transistor chemical sensors on a flexible, Mylar substrate.

## 1.6 Research Objective and Organization of the Thesis

The objective of the research is to develop a versatile hybrid fabrication approach that enables the controlled realization of multiscale (10 nm-1  $\mu\text{m}$ ) surface and volumetric hierarchical structures without using relatively complex nanolithographic approaches (e.g. EBL and FIB), and illustrate the utility of this technology through selected example applications. As an approach to achieve this goal, we demonstrate the TAME process based on sequential multilayer electrodeposition (i.e. layer-by-layer deposition of alternating, heterogeneous metallic layers) from top-down designed, conventionally defined initial templates of planar, or nonplanar geometry. Based on the development of the TAME process, (1) controllable realization of multiscale surface and/or volumetric hierarchical structures, as well as (2) evaluation of the fabricated structures in diverse applications will be presented.

The outline of the thesis is designed accordingly. First, the TAME process based on dual-bath electrodeposition will be introduced (Figure 1.5(a)). Second, mathematical modeling will be developed (Figure 1.5(b)), which is essential in designing initial process parameters to create desired structures based on the TAME process. Third, diverse multiscale surface (Figure 1.5(c)) and volumetric (Figure 1.5(d)) hierarchical nanostructures will be demonstrated based on the developed TAME process. These structures will include large area ( $>1\text{ cm}^2$ ), (1) planar, or (2) non-planar surfaces comprised of anisotropic, nanoscale surface relief structures of wide-ranging size scale (10 nm-1 $\mu\text{m}$ ); and (2) thick (10-100  $\mu\text{m}$ ) volumetric composite material in which individual metallic layers of micron, or submicron scale thicknesses are electrically insulated from the adjacent layer by interlamination insulating layers of similar thicknesses. Fourth, the utility of the

fabricated surface and volumetric structures will be evaluated in a variety of applications including nanoscale pattern transfer, superhydrophobic surface, laminated magnetic material for high frequency high flux operation, and miniaturized on-chip inductors (Figure 1.5(e)-(h)).

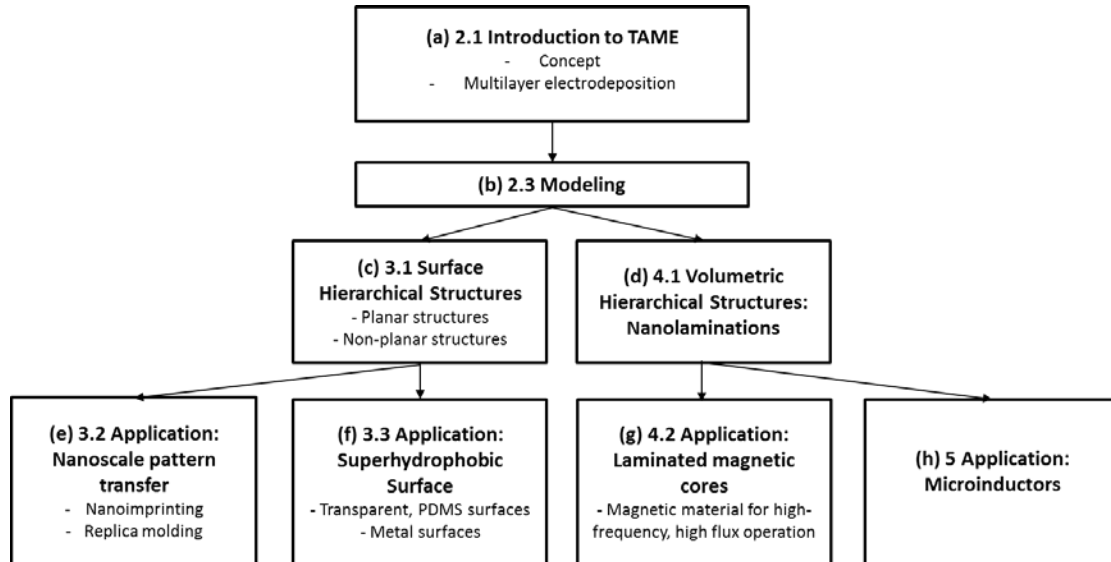


Figure 1.5 Thesis outline.

## CHAPTER 2

### TEMPLATE-ASSISTED MULTILAYER ELECTRODEPOSITION

#### (TAME)

#### 2.1 Process Overview

The TAME process enables a controllable, yet scalable realization of various hierarchical structures by combining conventional micromachining and multilayer electrodeposition. The TAME process is comprised of top-down MEMS-based template preparation processes, bottom-up sequential multilayer electrodeposition processes, and related post processes performed after the deposition, i.e., post-deposition processes.

The TAME process begins with fabrication of a template comprising an electrically insulating substrate, and a lithographically-patterned conductive seed layer (i.e. Ti/Cu/Ti) on the substrate (Figure. 2.1(a)). Typically, the substrate is a polished silicon wafer coated with a non-conducting material (i.e. silicon dioxide, PMMA); this additional layer is referred to as a “sacrificial layer.” The substrate may possess micromachined, pre-defined topographies (not shown in the figure).

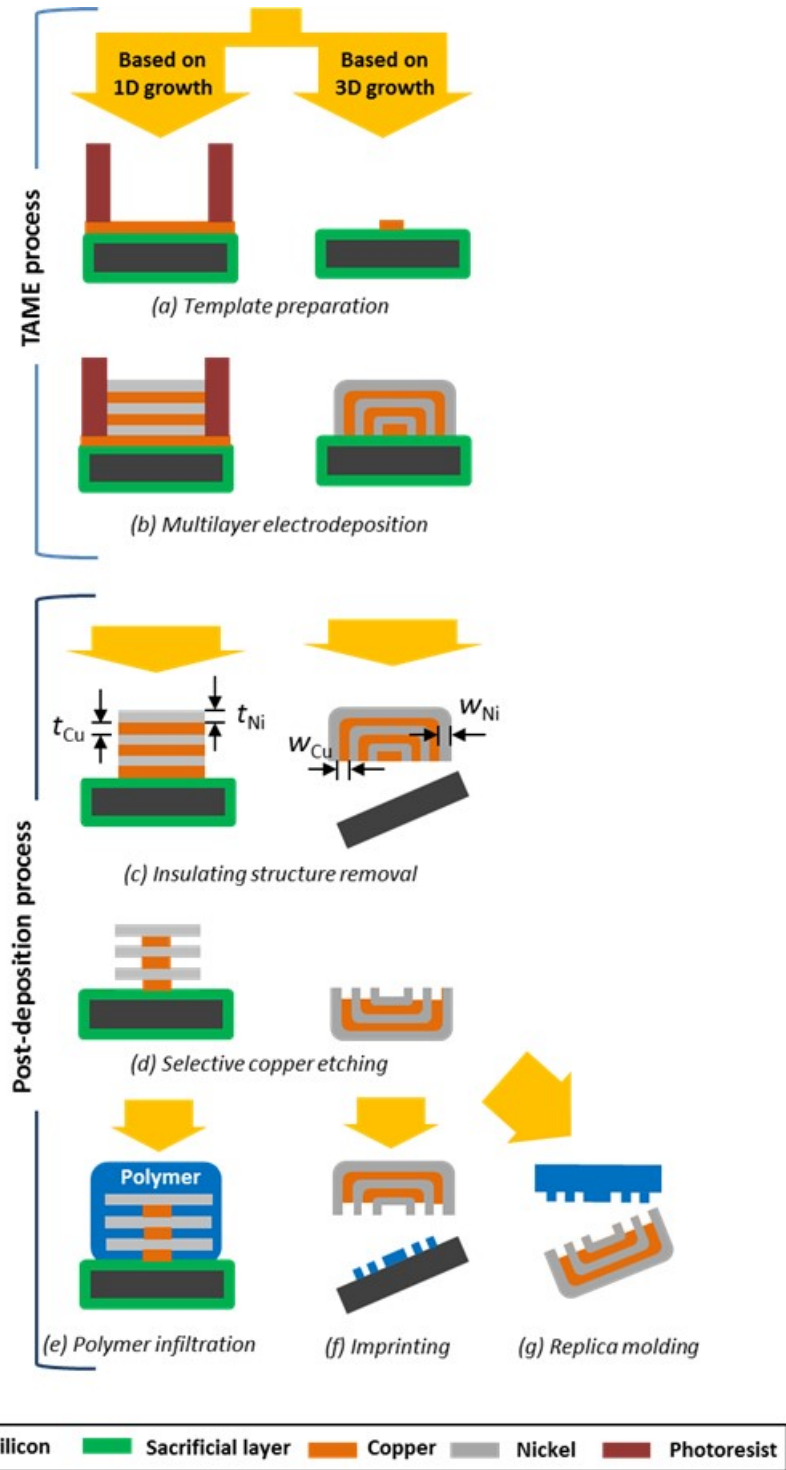


Figure. 2.1 Schematic illustration for TAME-based processes. The first column depicts the processes based on one-dimensionally grown multilayer structures, whereas the second column represents the processes based on three-dimensionally grown structures.

An electrodeposited multilayer structure is selectively and sequentially grown from the patterned seed layer, while its conformal growth is topographically guided by the insulating substrate (Figure 2.1(b)). Note that the multilayer structure may grow in one dimension (Figure 2.1(b), first column), or in three dimensions (Figure 2.1(b), second column) depending on the arrangement of the template. The three-dimensional growth of the multilayer begins not only from the top surface of the seed layer, but also from its sidewalls. The realization of surface hierarchical structures presented in the thesis relies on the three-dimensionally grown multilayer structures, while that of volumetric structures on the one-dimensionally grown multilayers, as will be discussed in the following sections.

In general, electrodeposition methods as well as layer materials should be properly chosen to fabricate multilayer structures with smooth, uniform metallic films of superior contrast and controlled individual layer thicknesses. Deposition of a multilayer structure is performed by using a customized automated dual-bath electrodeposition tool. A sample wafer is transferred from bath to bath using a robotic arm to deposit alternating layers of heterogeneous metals; each single electrodeposition sequence results in a layer, and structures can be fabricated from multiple layers of multiple materials. To illustrate the TAME process, nickel (or nickel-based alloys such as permalloy ( $\text{Ni}_{80}\text{Fe}_{20}$ ), all referred to as "nickel" unless specified) and copper are selected as multilayer materials, and are deposited in alternating pairs. When interpreting the presented results, we utilize the convention of the first layer (deposited within the first sequence of deposition,  $n = 1$ ) being nickel; hence, subsequent odd-numbered layers are nickel while their even-numbered counterparts are copper.

The thicknesses of individual layers of nickel and copper ( $t_{\text{Ni}}$ ,  $t_{\text{Cu}}$ ) are controllable both by deposition time and deposition current density; in this work, the deposition current was held constant and the layer thickness was determined by deposition time. Note that the increasing surface area of a three-dimensionally growing multilayer may decrease the current density, and therefore, the growth rate, correspondingly (Figure 2.1(b), second column). However, this has been suppressed to a negligible level ( $< 10\%$ ) by proper layout design of patterned seed layers; alternatively, a continuously adjustable current that maintains constant current density could be utilized. The reasoning behind the use of dual-bath galvanostatic deposition, use of specific material pairs (i.e. Ni/Cu), detailed operation of an automated system, as well as the limitation of the multilayer electrodeposition are discussed in the following chapter.

In order to transform the fabricated multilayer structure into surface reliefs, or volumes of laminated structures, a series of post-deposition processes has been developed. The insulating structures (i.e. patterned photoresist mold and/or sacrificial layers) are removed from the substrate, either chemically or physically, to reveal the edges of the deposited alternating nickel/copper layers (Figure 2.1(c)); this process is performed without damaging the deposited multilayer structure. The patterns comprising the revealed edges, referred to as "growth ring patterns," represent the spatiotemporal growth of the multilayer structure. After the process, the multilayer structure is completely separated, or in other words, "released" from the substrate.

A selective copper etching process follows, in order to define topographic features, i.e., surface relief structures, within the fabricated multilayer structure (Figure 2.1(d)). Two types of etchants are employed: thiourea-based etchant (1 M thiourea solution with pH

tuned to 1 using hydrochloric acid (HCl), etch rate: ~100 nm/min [31]) and ammoniacal etchant (concentrated ammonium hydroxide (NH<sub>4</sub>OH) solution saturated with copper sulfate, etch rate: 0.5~1 μm/min [32]). The former is used to etch less than 1 μm of copper; otherwise, the latter is employed. The selective copper etching may extend through a significant portion of the multilayer volume, resulting in the structures comprised of free-standing, high aspect ratio nickel films (Figure 2.1(d), left).

It is particularly interesting that the orientation of the surface relief structures can be controlled by the pre-defined geometry of the insulating surface of a template; for example, the relief structures may face upward (or, in other words, their surface normal vector being upward), as shown in Figure 2.1(d), right column. In the ideal case, where the multilayer deposition is spatially isotropic, the widths of nickel and copper are identical to the thicknesses of the corresponding layers.

$$w_{Ni} = t_{Ni}, w_{Cu} = t_{Cu} \quad (2.1)$$

Such relief patterns can be relatively easily transferred to other materials (e.g. polymer resists) via imprinting or replica molding (Figure 2.1(f), (g)). In addition, the voids left after the selective etching can be filled by completely different materials (e.g. electrically-insulating thermoplastics and elastomers) (Figure 2.1(e)). The pattern transfer and trench infiltration techniques extend the achievable material diversity of TAME, thereby substantially improving the versatility of the process.

The structures stemming from the multilayer electrodeposition are referred to as “TAME structures,” or “TAME-based structures.” The TAME structures are (1) batch-fabricated (because the electrodeposition is performed in batch-scale); while their (2)



nanostructure dimensions are defined by the deposition parameters without relying on expensive conventional nanolithography; and (3) their overall geometries and positions are controlled by projection lithography. The discussion about the multilayer electrodeposition follows since it is the central process shared by all TAME processes. Characterization and theoretical modeling of the three-dimensional multilayer growth then follow, so as to assist with the prediction of final TAME structures from initial parameters.

## **2.2 Multilayer Electrodeposition for the TAME Process**

In order to validate the TAME process, it is important to employ a deposition technique that can achieve multilayer structures with arbitrary individual layer thicknesses at reasonable process throughput. In particular, this technique should be able to rapidly produce nickel/copper multilayers with wide-ranging (1) periodicities (e.g. from tens-of-nanometers to over a micron) and (2) material thickness ratios (e.g. 99:1, nickel to copper, or vice versa), while (3) achieving superior compositional contrast between nickel and copper. Also, the individual layers should be (4) smooth with sufficiently (5) low built-in stress, so that a thick multilayer deposit with well-defined individual layers can be fabricated. The details as well as reasoning behind the automated setup, electrodeposition bath, and deposition parameters will be presented.

### **2.2.1 Automated Dual-Bath Electrodeposition of Nickel/Copper**

In general, there are two ways to perform a multilayer electrodeposition. Both dual-bath electroplating and single-bath electroplating have been reported for the fabrication of various multilayers comprising two materials [33].

Table 2.1 Studies on dual-bath electrodeposition.

| Material       | Periodicity (nm)    | Electrolytes                          | Methods                  | Application   | Ref.      |
|----------------|---------------------|---------------------------------------|--------------------------|---|-----------|
| Ni/Cu          | 70000               | Ni sulfate, Cu sulfate                | Manual                   | Improved tensile strength                                       | [34]      |
| Cu/Ag          | 24000               | Cu sulfate, Ag cyanide                | Manual                   |   | [34]      |
| Ni/Cu          | 8                   | Ni sulphamate, Cu sulfate             | Manual, galvanostatic    |   | [36]      |
| Zn/Ni          | 1400 (< 10 pairs)   | Zn sulfate, Ni sulphamate             | Manual, galvanostatic    | Improved corrosion resistance                                   | [37]      |
| Zn/Ni          | ~500                | Zn sulfate, Ni sulfate                | Manual, potentiostatic   |   | [38]      |
| Sn/Ni          | ~30000, 3 pairs     |                                       |                          | Inhibited fatigue growth  | [39]      |
| Zn/Co          | 600 (20 pairs)      | Zn sulfate, Co sulfate                | Unknown, galvanostatic   | Improved corrosion resistance                                   | [40]      |
| Zn/Co          | 6 (50 pairs)        | Zn sulfate, Co sulfate                | Unknown                  | GMR   | [41]      |
| Co/Pt          | 10                  | Co sulfate, Pt chloride               | Unknown, potentiostatic  |   | [42]      |
| NiFe/Cu        | ~1000               | NiFe sulfate, Cu sulfate              | Manual, galvanostatic    |   | [43]      |
| CoPtP/Cu       | 120                 | Co sulfate, Pt chloride, Cu sulfate   | Unknown, galvanostatic   | Uncompromised magnetic properties                               | [44]      |
| NiFe/Cu        | 2000                | Ni sulfate, Cu sulfate                | Manual, galvanostatic    | Suppressed eddy current   | [45]      |
| NiFe/Cu        | 2000                | Ni sulfate, Cu sulfate                | Automated, galvanostatic | Electrolytic supercapacitor                                     | [32]      |
| Ni/Cu, NiFe/Cu | 30 (Over 180 pairs) | Ni sulfate, Commercial Cu electrolyte | Automated, galvanostatic | Pattern transfer, Non-wetting surfaces, Suppressed eddy current | This work |

The former approach [34] uses two independent electroplating baths where a sample is transferred from one bath to the other in order to electroplate alternating layers of two materials. The latter approach [35] utilizes a single bath containing parent metals for both deposits, and relies on changes in current density, or deposition potential to deposit the respective metals.

Although it results in additional equipment complexity, a dual-bath electrodeposition technique is employed for our application as it yields higher compositional contrast between the alternating layers and possesses a larger process window resulting from the complete independence of the two cathodic deposition reactions. Since the two depositions can be controlled independently, there is a higher degree-of-freedom in selecting electrodeposition solutions for the deposition of desired materials.

Nickel and copper are chosen as the multilayer materials to meet the criteria for uniform, smooth deposits. Dual-bath electrodeposition of various couples has been investigated as presented in Table 2.1. A displacement reaction between the less noble metal and the parent ions of the more noble metal may take place immediately after a sample is immersed into the deposition bath (of the more noble metal). This inhibits a formation of smooth multilayers as described in the literature citations. The onset of such reaction is difficult to predict through the nominal deposition potential difference between the two materials, because the reaction is attributed to various aspects of the electrolyte (e.g. pH, parent metal concentration, types of anions). It is known that Ni/Cu deposition using acidic electrolytes is relatively free from such undesirable reaction due to the self-passivation of nickel in an acidic copper electrolyte that prevents the surface of nickel from

being dissolved in the electrolyte [36]. Multilayers with very small structural periodicities ( $< 10$  nm) have been already demonstrated (Table 2.1). Using the Ni/Cu multilayer is well suited for the TAME process also because the electrochemistry of the deposition reactions is relatively well studied; it is feasible to choose the deposition baths of nickel and copper among various options to meet the TAME process requirements.

An automated, dual-bath electrodeposition setup is developed correspondingly. The system consists of a series of baths (a nickel electrodeposition bath (1~5 L) with a nickel anode, a copper deposition bath (1~5 L) with a copper anode, and four rinsing baths comprising two deionized water baths (5 L each), a nickel electrolyte bath (1 L), and a copper electrolyte bath (1 L)), two current supplies each connected to an anode to control nickel and copper electrodeposition independently, and a computer-controlled robotic arm which moves a sample from bath to bath (Figure 2.2). The sequential multilayer electrodeposition is performed as follows: In the first sequence, i.e.,  $n = 1$ , of the multilayer electrodeposition, the sample is moved to the nickel electrodeposition bath to deposit the first layer of nickel (Figure 2.2(a)). Then, the sample is sequentially rinsed through two rinsing baths containing deionized water in order to remove the plating solutions that may remain on the sample surface. Afterwards, the sample is briefly rinsed in the copper electrolyte bath, which is compositionally identical to the copper electrodeposition bath (Figure 2.2(b)). The purpose of this process is to substitute the rinsing water that may remain on the sample surface to the copper electrolyte, and thereby prevent the subsequent copper deposit from being porous due to the hydrolysis of water [36]. Unless this process is included, the surface roughness of the multilayers with short ( $\sim 100$  nm) periodicities tends to increase during the deposition process (and a portion of the multilayer surfaces

turn matte; this can be observed by the naked eye). The second sequence of the deposition, i.e.,  $n = 2$ , then follows in the copper electrodeposition bath (Figure 2.1(a)). The sample is sequentially rinsed through two deionized rinsing baths and the nickel electrolyte bath before the third sequence of the deposition in the nickel electrodeposition bath. This process is repeated to build a multilayer structure with the desired number of nickel and copper layers with predesigned individual thicknesses.

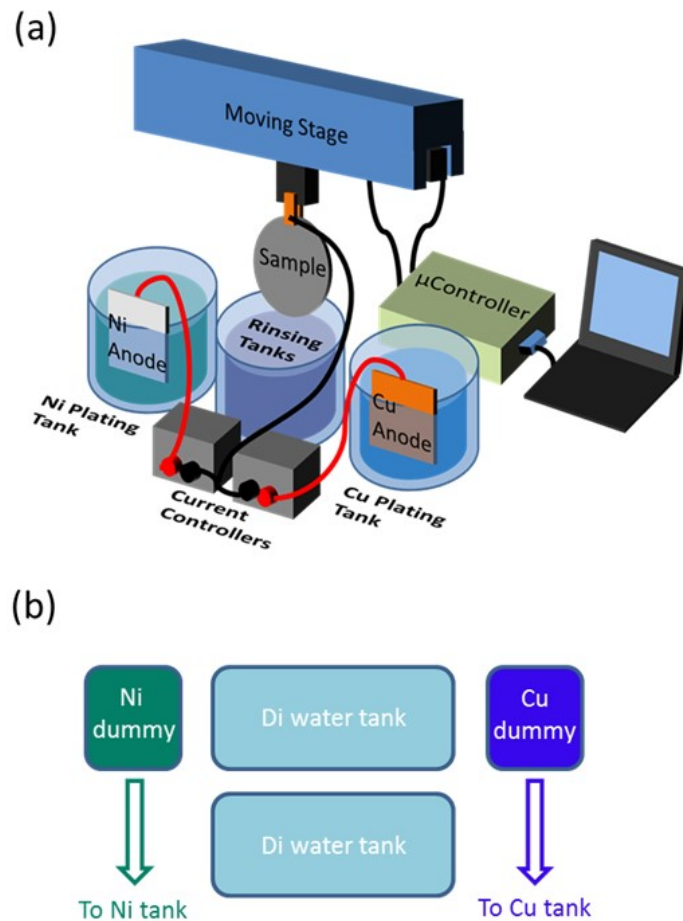


Figure 2.2 Automated, dual-bath multilayer electrodeposition system. Note that (a) is describing the overall system, while (b) is a schematic that describes the configuration of the rinsing baths.

### 2.2.2 Deposition Parameters and Deposition Baths

The thicknesses of individual metal layers can be defined either potentiostatically (i.e. deposition at a fixed potential with respect to a third reference electrode), or galvanostatically (i.e. deposition based on a constant electrical current induced between the anode and cathode). The latter is chosen for the experiments since it allows us to estimate the deposition rate at a specific current density; the designed individual layer thicknesses can be achieved by controlling the individual layer deposition time while the current density is held constant. The typical current densities of nickel and copper deposition are set within the range of 10~20 mA/cm<sup>2</sup> considering the trade-off between the productivity (i.e. deposition rate) and built-in stress of the deposited materials.

Table. 2.2 Composition of the electrodeposition baths.

| <b>Watts Ni Bath</b>                          | <b>Permalloy (Ni<sub>80</sub>/Fe<sub>20</sub>) bath</b> | <b>Sulfate-based Cu bath</b>                  |
|---|---|---|
| NiSO <sub>4</sub> ·6H <sub>2</sub> O, 200 g/L | NiSO <sub>4</sub> ·6H <sub>2</sub> O, 200 g/L           | CuSO <sub>4</sub> ·5H <sub>2</sub> O, 200 g/L |
| NiCl <sub>2</sub> ·6H <sub>2</sub> O, 5g/L    | FeSO <sub>4</sub> ·7H <sub>2</sub> O, 8g/L              | Sulfuric acid<br>(98 wt%, 20 mL/L)            |
| Boric acid, 25 g/L                            | NiCl <sub>2</sub> ·6H <sub>2</sub> O, 5 g/L             |   |
| Saccharin, 3 g/L                              | Boric acid, 25 g/L                                      |   |
|   | Saccharin, 3 g/L  |   |

The electrodeposition baths for nickel and copper are chosen to meet the TAME criteria. The Watts type bath (Table 2.2) is selected as the nickel bath, since the built-in stress is low enough to deposit thick (~100  $\mu\text{m}$ ) deposits with small surface roughness (~10 nm). The pH of the as-prepared bath is 1.8, so sodium hydroxide is added until the pH becomes at least 3.5. At pH lower than 2, the nickel deposition current efficiency (i.e. the ratio between the actual volume of the deposit to the theoretical estimation assuming all the electrons delivered to the working electrode being used up for the reduction of the nickel ions) drops below 60%; this results in a decrease of the deposition rate, as well as an increased “pitting” on the deposits resulting from the increased hydrogen ion reduction. After the pH is changed to 3.5, the current efficiency increases to over 80% (10  $\mu\text{m}/\text{hour}$  at 10  $\text{mA}/\text{cm}^2$ ). For the deposition of nickel/iron alloy, an iron salt (i.e. iron sulfate, 8 g/L) can be added (Table 2.2).

A commercially-available copper plating solution with brighteners and levelers (Clean Earth<sup>TM</sup> Mirror Copper Solution, Grobet USA) is utilized for the copper deposition. As an initial attempt, the deposition is performed using a bath comprising copper sulfate and sulfuric acid dissolved in deionized water (Table 2.2). It is observed that the roughness of the multilayer increased with respect to the increasing number of nickel/copper pairs, or in other words, increasing total thickness of the deposit. On the contrary, the surface roughness of the multilayer based on the commercial bath is even comparable with that of the sputtered seed layer (500 nm, or 1000 nm of Cu/30 nm-thick Ti). This is quantified by comparing the two multilayer samples comprised of 40 pairs of permalloy ( $\text{Ni}_{80}\text{Fe}_{20}$ )/copper using two different copper electrolytes; all the metals are electrodeposited at a current density of 10  $\text{mA}/\text{cm}^2$ . Atomic force microscope

measurements of the roughness of the topmost permalloy layer (40th layer) of the multilayer structures formed from the sulfate-based, and the commercial copper bath are 171 and 7 nm, respectively (Figures 2.3(a), (b)). Figure 2.3(c) shows the scanning result of the sputtered seed layer as a reference.

The individual metal layers can be imaged from the cross-section, or the sidewall of the multilayers. A short period of selective copper etch is performed prior to the imaging to obtain clear contrast between permalloy and copper layers; the darker layers correspond to the etched copper layers, while the brighter layers are permalloy layers. It is observed that the roughness of the layers continually increases with respect to the layer count for the sample deposited using the sulfate-based copper bath (Figure 2.3(d)), while the layers from the sample plated with the commercial, bright copper bath are smooth and uniform throughout the deposit (Figure 2.3(e)). From these observations, the bright copper bath is selected for this work, as smooth copper deposits are essential to build thick multilayers of large total thickness ( $>100\ \mu\text{m}$ ) with smooth and uniform metal layers throughout the volume.

### **2.2.3 Other Conditions**

The multilayer electrodeposition is performed at room temperature without any agitation for consistent fabrication results, although elevated bath temperature as well as forced convection may improve deposition current efficiency and uniformity. Stirring bars are not used in the experiments, since the directional agitation may result in a significant deposition non-uniformity. The electrodeposition electrolytes are filtered (Durapore<sup>TM</sup>,  $0.22\ \mu\text{m}$ , EMD Milipore) before each use.



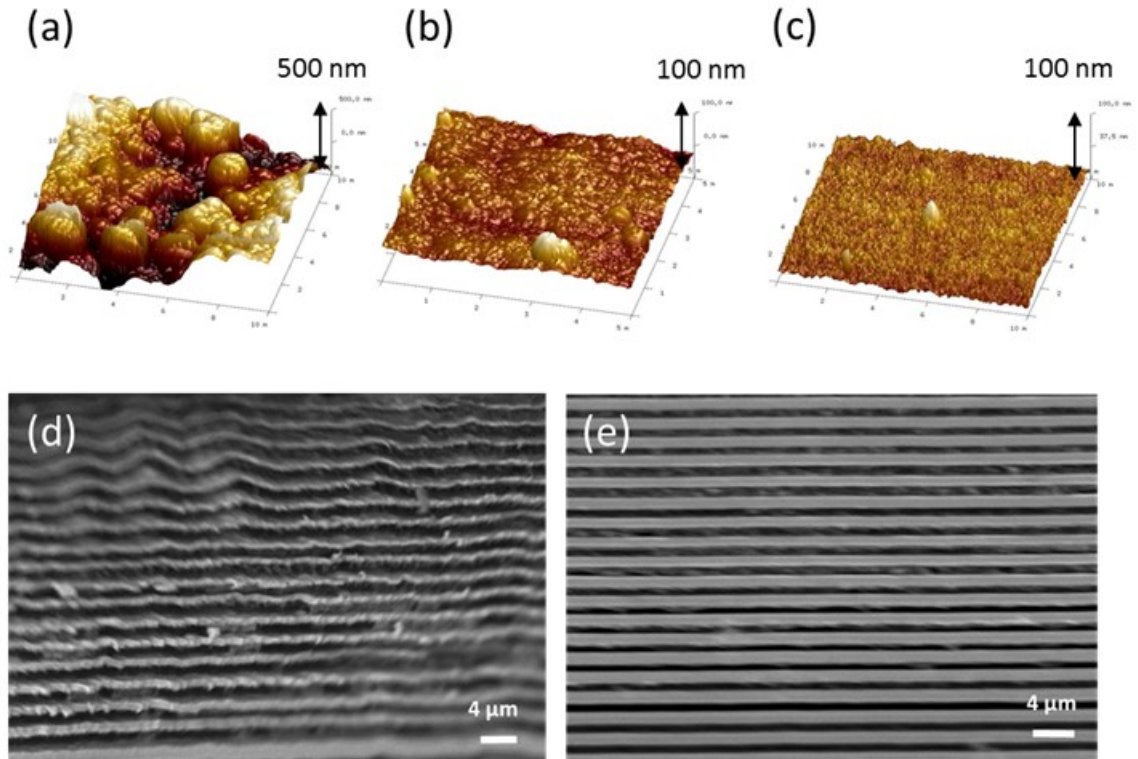


Figure 2.3 AFM ( $10\ \mu\text{m} \times 10\ \mu\text{m}$ ) and SEM images of the multilayers fabricated based on different copper electrolytes. AFM scan on the top layers of the 40<sup>th</sup> permalloy layer. Copper is deposited in the (a) sulfate-based electrolyte, and (b) commercially-available solution, respectively. (c) AFM scan of the sputtered copper seed layer ( $R_a = 7\ \text{nm}$ ). (d) Cross-sectional view of the multilayer, fabricated based on the sulfate-based copper electrolyte. (e) Image from the multilayer fabricated using the commercial copper bath.

## 2.2.4 Examples of Fabricated Multilayers

In this section, various multilayer samples are presented, demonstrating the capability of multilayer electrodeposition.

*<Thickest multilayer sample with largest layer count>*

A 180  $\mu\text{m}$ -thick multilayer structure with 300 pairs of 300 nm-thick permalloy layers and 300 nm-thick copper layers is the thickest deposit that has been fabricated (Figure 2.4). Such samples are formed through thick, patterned SU-8 molds. The multilayer is released from the SU-8 mold, by immersing the sample into boiling DI water for a sufficient amount of time; after  $\sim 1$  hour, the metal deposit is mechanically separated from the swollen SU-8.

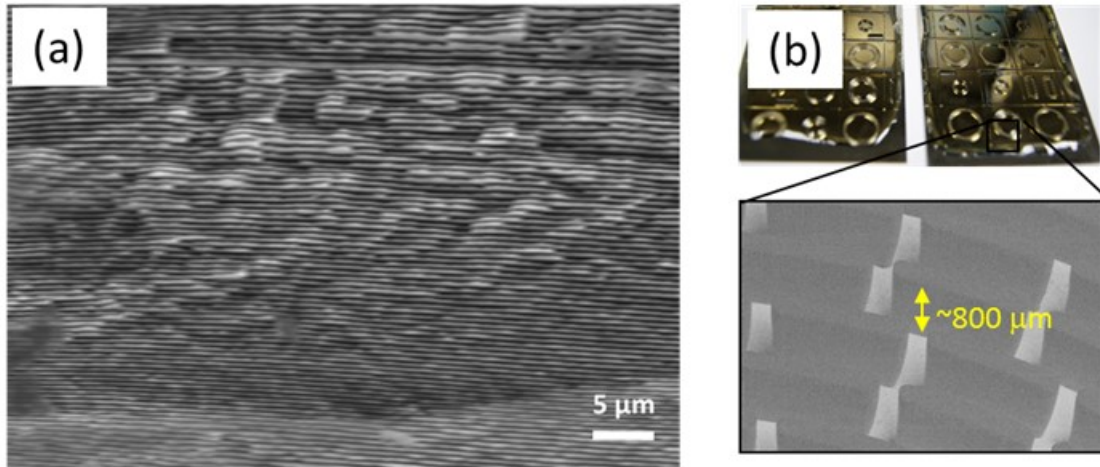


Figure 2.4 Thick multilayers. (a) Cross-sectional view of a 300 pairs of permalloy/copper multilayer sample. The deposit is electrodeposited through an 800  $\mu\text{m}$ -thick SU-8 molds shown in (b).

*<Multilayers with the thinnest layers>*

The multilayers with the thinnest individual layers (i.e. the layers with minimal thicknesses, yet continuous, and thereby, discernable through SEM imaging) are comprised of 30 nm-thick nickel/copper pairs (Figure 2.5). The sample is fabricated by depositing nickel and copper, 3 seconds each, at the current densities of 10 mA/cm<sup>2</sup> and 15 mA/cm<sup>2</sup>, respectively. Although the layers are continuous throughout the sample, the striations are rather corrugated due to the layer thicknesses being similar to the surface roughness of the deposited layers.

The surface roughness could be improved in two ways: The first is to reduce the grain sizes of nickel and copper by employing pulse, or pulse-reverse deposition [46]. The surface roughening may also result from the exchange reaction that inherently occurs in the copper deposition bath. The nickel atoms from the sample surface may randomly dissolve into the solution and be replaced by copper, thereby creating an intermixed interface with significant roughness. This issue can be addressed by adopting potentiostatic deposition; the copper layer could be initiated under potentiostatic conditions where the dissolution of nickel in the copper bath could be prevented by a proper copper deposition potential.

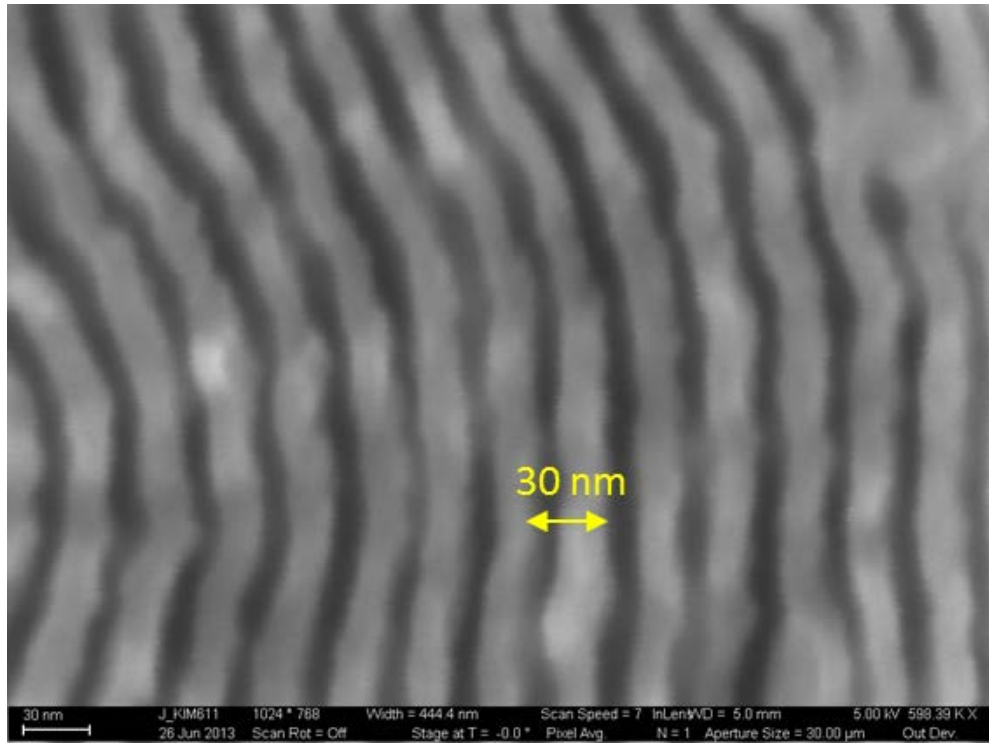


Figure 2.5. Multilayers with the thinnest individual layers.

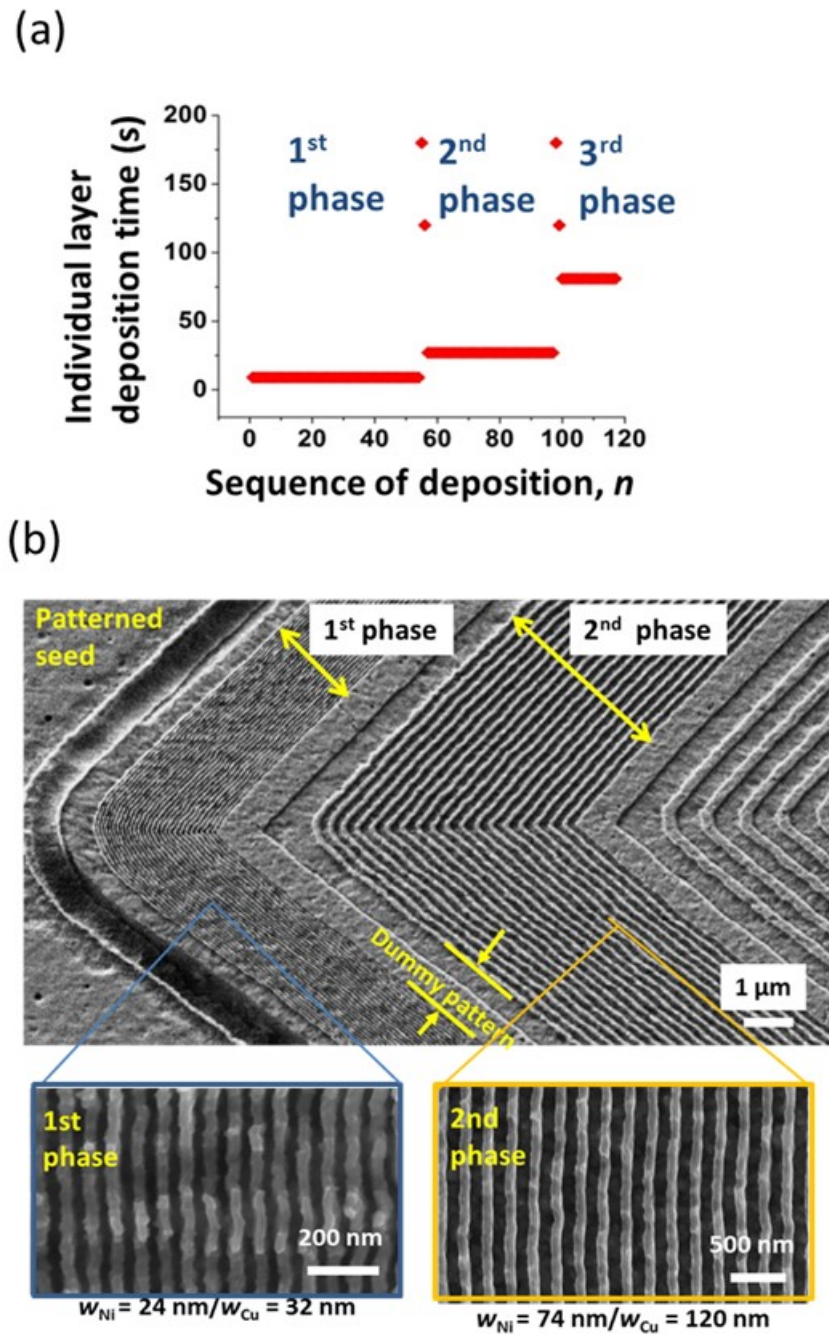


Figure 2.6. Multilayers with multiscale periodicities. (a) Deposition sequence of the sample. Note that the nickel is deposited within the odd number of sequences (including the 1<sup>st</sup> sequence), while the copper deposited within the even number of sequences. (b) Magnified view.  $w_{Ni}$ , and  $w_{Cu}$  represent the measured widths (or thicknesses) of the individual nickel, and copper layers.

*<Multilayers with multiscale periodicities>*

By changing the individual layer deposition time, the structural periodicity of the layers can be varied during a single multilayer electrodeposition. Figure 2.6 shows a multilayer structure of which periodicity ranges from 65 nm to over a single micrometer. A deposition duration sequence for the fabricated multilayer structures is also shown in Figure 2.6(a). In the 1st, 2nd, 3rd phase of the multilayer deposition, nickel and copper layer deposition times are 9, 27, 81 seconds, respectively. Between each deposition phase, a dummy pattern comprising a pair of a nickel and a copper layers ( $w_{\text{Ni}} + w_{\text{Cu}} = 1140 \text{ nm}$ ) is created in order to discern the multilayer structures with different periodicities.

This is a unique advantage of the multilayer electrodeposition compared to other types of bottom-up nanofabrication techniques. The size scale of the resulting structures from most of bottom-up assemblies (such as colloidal assembly, or block copolymer assembly) rely on the unit “building blocks” they utilize (e.g. colloidal particles, in the case of colloidal assembly); hence, it is very difficult for those processes to produce multiscale structures within a single run.

The details of an automated, dual-bath multilayer electrodeposition has been presented in this subchapter. The developed approach is suitable for batch-fabrication of thick ( $> 100 \mu\text{m}$ ) multilayer deposits of which individual layer thicknesses scale down to a few-tens-of-nanometers, thereby, satisfying the criteria for the TAME process.

## 2.3 Multilayer Growth Modeling

A key requirement of the TAME-based fabrication approaches is the ability to design the templates to result in desired multilayer structures. Thus, a theoretical calculation of the resulting structure for a given set of initial conditions including the geometries of pre-defined templates and deposition parameters (i.e., deposition rates for both metals, full sequence of individual layer deposition times) should be enabled. For one-dimensionally grown, through-mold electrodeposited multilayer structures, the prediction is relatively straightforward since the growth orientation is strictly defined in the vertical direction (with respect to the substrate); herein, we only focus on the prediction of three-dimensionally grown multilayer structures. First, a mathematical model for the multilayer growth is presented. Second, the actual growth of a multilayer is modeled and compared to the actual growth. Third, the non-ideality of the growth is discussed, which results in errors between the model and the actual growth.

### 2.3.1 Ideal Growth Model

The prediction of the surface structures obtained from the three-dimensionally grown multilayer structures is based on the theoretical estimation of the growth ring patterns of the fabricated multilayer structures. Based on the hypothesis of ideal multilayer growth (i.e. perfectly uniform, isotropic growth of both nickel and copper layers with constant growth rates throughout the process), the projection of an arbitrary sublayer surface formed at the  $n$ th deposition sequence onto the insulating surface of the substrate, which is defined as  $I_n$ , can be calculated as the locus of points equidistant from the

periphery of the patterned seed layer by  $r_n$ , i.e., the theoretical estimation of the multilayer thickness after the  $n$ th sequence:

$$r_n = \sum_{i=\text{odd}}^n G_{\text{Ni}} t_i + \sum_{i=\text{even}}^n G_{\text{Cu}} t_i \quad (2.2)$$

where  $G_{\text{Ni}}$  and  $G_{\text{Cu}}$  are the estimated growth rates of nickel and copper, respectively, and  $t_i$  is the deposition duration of the  $i$ th deposition sequence. Note that the growth of a metal is characterized by a single growth rate, and the width of a growth ring is identical to the thickness of the metal layer, as expressed in Equation 2.1.

Then, a sequenced calculation of  $I_n$  for varying  $n$  would lead to the fully-predicted growth ring pattern of a three-dimensionally grown multilayer structure. Here, a morphological dilation based on a structuring disk ( $S_n$ , radius =  $r_n$ ) is demonstrated as an example. This process is briefly depicted in Figure 2.7 for  $n=3$ . Note how  $I_3$  is defined by the nickel layer formed at the 3<sup>rd</sup> sequence, and modeled by a translation of a virtual structural disk  $S_n$  along the periphery of the seed layer (this will be further detailed in the next subchapter).

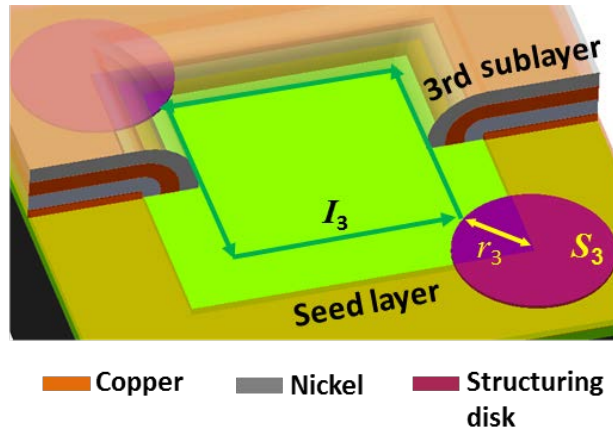


Figure 2.7 Pictorial depiction of the multilayer growth modeling ( $n = 3$ ).



### 2.3.2 Growth Modeling Using Morphological Dilation

An actual modeling process is demonstrated using binary morphological dilation [47]. First, a grey scale SEM image of a released multilayer structure (observed from the bottom of the multilayer) is prepared (Figure 2.8). Note that the copper is selectively etched before the SEM imaging to achieve a clear contrast between nickel and copper. After the contrast of the image is enhanced using proper image processing, the resulting grey scale image is converted into a corresponding binary image. Second, the outer boundaries of the patterned seed layer are taken from the image, and all the pixels within the boundaries are “filled,” or, in other words, converted to “1.” The binary image after this process is defined as the input image,  $D_0$  (Figure 2.9(a)).

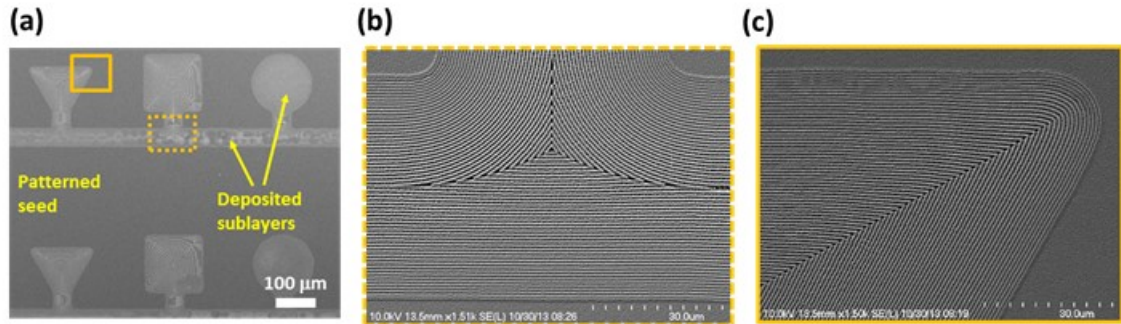


Figure 2.8 Original SEM images for modeling. Images (b), (c) are magnified views of the respective sites within (a).

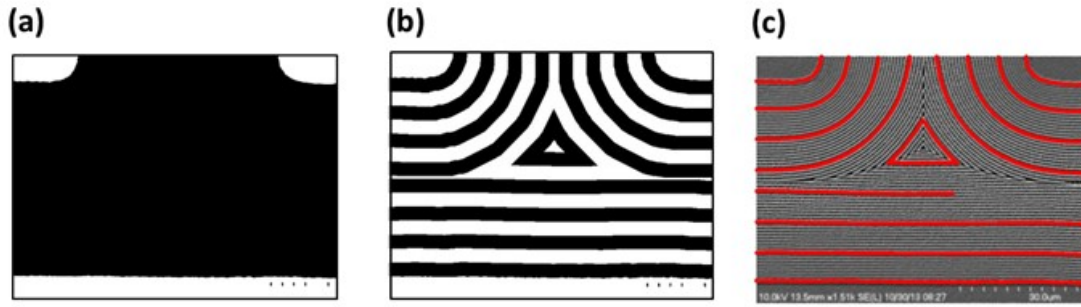


Figure 2.9 Image processing using Figure 2.8(b). (a) Input image,  $A_0$ . Detected seed layer pattern is colored in white. (b) Image obtained after multiple dilation process. The boundaries between black and white regions are  $I_n$ . (c)  $A_n$  cropped from the original SEM image.

A disk-type structuring element ( $S_n$ ) the radius of which is  $r_n$ , i.e., the total multilayer structure thickness after the  $n$ th deposition sequence, is set. Third, a dilation of  $D_0$  is performed using the structuring element. For each pixel of  $D_0$  (referred to as an “input pixel”), the center of  $S_n$  is superimposed. If at least one pixel of  $S_n$  corresponds to the filled region of  $D_0$ , then the input pixel is set to “1.” The resulting image after the entire scan is referred to as “ $D_n$ .” In other words, the filled region within  $D_n$  is the locus of  $S_n$  when the center of  $S_n$  travels inside the filled region of  $D_0$ . By an iterative calculation, a desired set of  $D$  (e.g.  $D_n, D_{2n}, D_{3n}, D_{4n} \dots$ ) is calculated, and the  $I$  of interest (e.g.  $I_n, I_{2n}, I_{3n}, I_{4n} \dots$ ) is obtained from the periphery of  $D$  (Figure 2.9(b)). Fourth, the corresponding, actual multilayer growth ring boundaries (e.g.  $A_n, A_{2n}, A_{3n}, A_{4n} \dots$ ) are detected and plotted based on the Canny edge detection method (Figure 2.9(c)). Finally, the desired  $I$  and  $A$  are overlapped on the original SEM image (Figure 2.10). MATLAB™ is used for the modeling; however, various tools (e.g. commercially-available CAD tools such as SolidWorks™ or AutoCAD™) can be also utilized to assist the process.

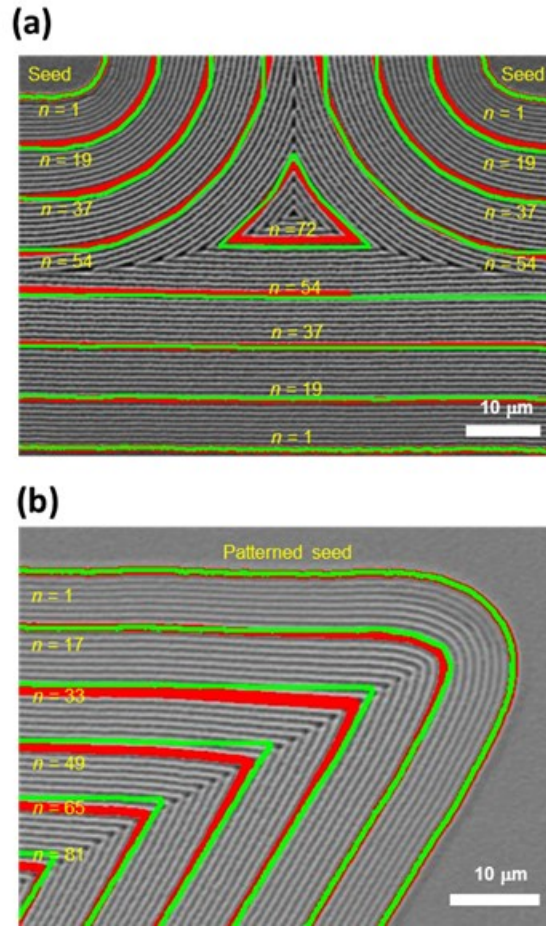


Figure 2.10 Comparison between  $I_n$  (light green) and  $A_n$  (red) for both images, Figure 2.8 (b), (c). The radius of the structuring disk is  $r_n$  [nm] =  $400n$ .  $I_n$  was calculated by using  $A_1$  as the initial seed layer periphery.

The model [47] is validated by comparing the modeled locus ( $I$ ), and the corresponding locus detected from the actual image of fabricated structures ( $A$ ). The locus  $I$  successfully models the growth rings generated from the curved corner of the seed layer forming an acute angle ( $60^\circ$ ) between the deposition sequences  $n = 17$  and  $n = 33$  (Figure 2.10(a)). Also, it models the growth ring generated from three different portions of the seed layer smoothly merging into a triangular growth ring between  $n = 54$  and  $n = 72$  (Figure

2.10(b)). The gradual geometry and position change of the growth rings throughout the deposition can be accurately modeled; this means the “ideal” growth assumption is valid, and the TAME-based nanostructure realization is highly controllable. Further development of the model may include the extension in the “third” dimension using a structuring “ball” rather than a planar disk. In addition, an “inverse operator” could be developed to assist the design of initial parameters (including deposition parameters and seed layer layout) for a given, desired final pattern.

### **2.3.3 Non-Ideal Deposition**

The discrepancy between  $I_n$  and  $A_n$  represents the accumulation of any non-ideal, spatiotemporal aspects of the multilayer growth between the first and the  $n$ th sequence. A sample wafer is analyzed of which template and the deposition process is depicted in Figure 2.11. In general, nanostructures with relatively larger feature sizes are observed in the samples deposited from the lower part of the substrate (i.e. those patterns immersed most deeply in the deposition bath as depicted in Figure 2.11(a)), since the sample substrate is immersed while the current supplies are “on.” This is observed in Figure 2.11 (c). Note that the measurements shown in Figure 2.11(c) are based on the actual surface structures with designed critical dimensions ( $w_{Ni} = 200$  nm,  $w_{Cu} = 300$  nm). Ideally, the average pitch should be 500 nm along the entire deposition sequence. However, the actual pitch of the nanostructures deviates from the average by  $\pm 15\%$ .

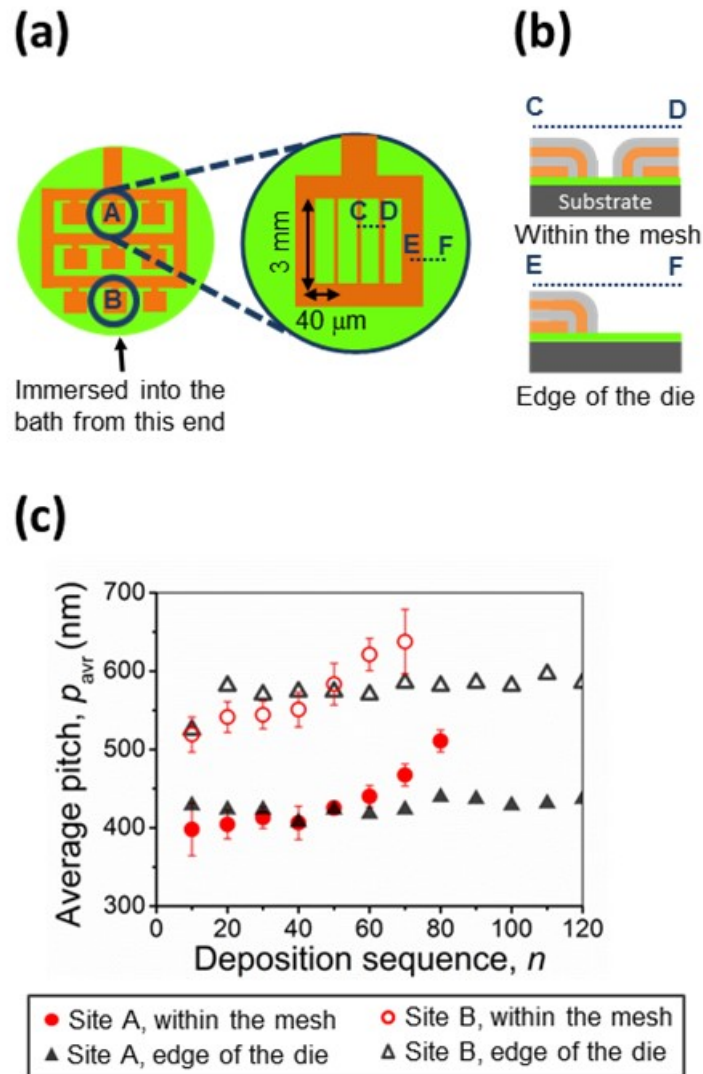


Figure 2.11 Spatiotemporal characteristics of multilayer growth. (a) Schematic top view of a seed layer (orange) patterned on an insulating substrate (green). (b) Schematic cross-sectional view for the multilayer being grown from the respective sites. (c) Average pitch ( $\overline{w_{Ni}} + \overline{w_{Cu}}$ ) as a function of deposition sequence ( $n$ ). The average pitch at  $n$  is calculated by measuring the total width of 5 pairs of nickel and copper growth rings formed between the  $(n-9)$ th sequence and the  $n$ th sequence, and dividing it by the number of pairs.

In addition, nanostructure feature sizes may vary with respect to the changing geometry of the conductive surface of the growing multilayer structure. From the results from a single site (either site A or B depicted in Figure 2.11(a)), it is observed that the measured pitches (Figure 2.11(c)) change as the deposition sequence progresses for the nanostructures formed within the meshes (Figure 2.11(b), upper), unlike the measured pitches from those sites formed at the edge of a die (Figure 2.11(b), lower), which are nearly constant.

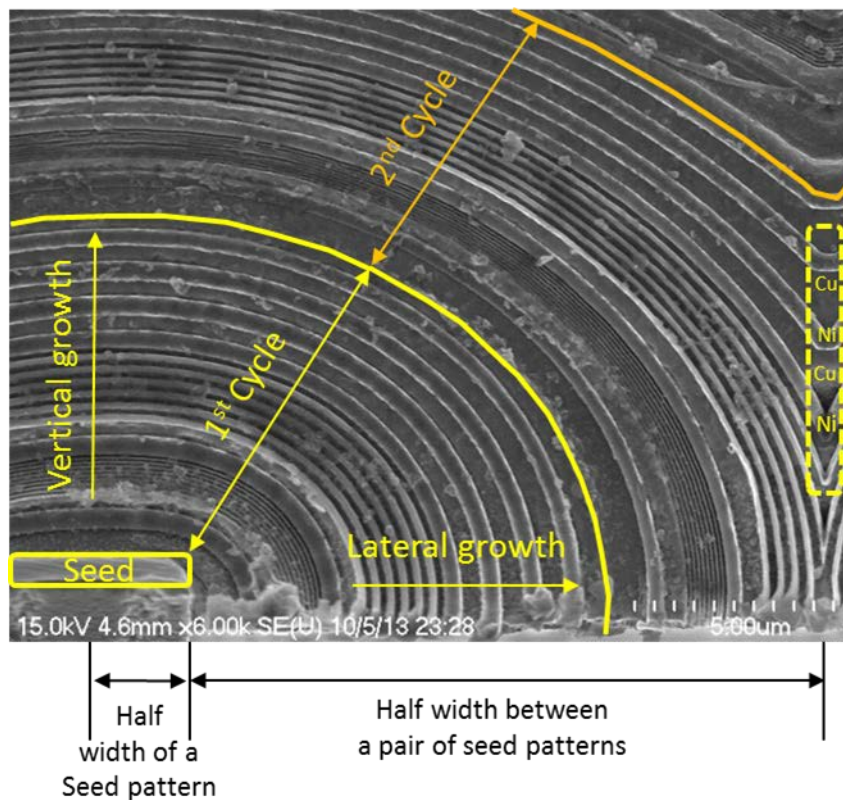


Figure 2.12 Cross-sectional SEM image of a multiscale multilayer structure.

The change reflects the increasing multilayer deposition rate in the vicinity of the insulating template surface with respect to the decreasing gap between the approaching surfaces of the growing multilayer.

This behavior is further characterized with the multiscale multilayer structures with similar material thickness ratio ( $t_{\text{Ni}}:t_{\text{Cu}} \sim 1:1$ ), of which structural periodicities are repeated through multiple cycles (Figure 2.12). A cross-sectional image from the multilayer is utilized for the characterization. The temporal change of the lateral/vertical growth rates of the metals (either nickel or copper) are estimated by measuring widths/thicknesses of the individual layers deposited for an identical deposition duration, at two different cycles. The lateral growth rate of nickel is reduced throughout the deposition ( $w_{\text{Ni}} = 178 \text{ nm} \rightarrow 143 \text{ nm}$ ), which is as expected since the current density gradually decreases during the multilayer deposition process. However, the rate of copper is increased significantly ( $w_{\text{Cu}} = 132 \text{ nm} \rightarrow 192 \text{ nm}$ ). On the contrary, the vertical growth rates are slightly decreased for both materials ( $t_{\text{Ni}} = 154 \text{ nm} \rightarrow 132 \text{ nm}$ ,  $t_{\text{Cu}} = 145 \text{ nm} \rightarrow 132 \text{ nm}$ ). Hence, it can be concluded that the increased average pitch shown in Figure 2.11(c) is attributed to the gradual increase of the copper deposition rate near the substrate; the effect due to the nickel deposition rate change is comparably negligible. This counterintuitive rate change trend of copper is attributed to the superior leveling effect of the commercially-available copper electrolyte. The superconformal nature of copper deposition can be clearly observed within the dotted region of Figure 2.12; the thickness of the deposit at the “valley” formed between the merging multilayer surfaces is much larger than the copper thicknesses measured from other sites. Using a deposition bath with a controlled leveling effect seems critical to achieve both predictable deposition and smooth deposit.

## 2.4 Summary

An introduction to the TAME process was provided. The TAME process combined conventional microlithography and multilayer electrodeposition to enable the realization of various hierarchical structures. The achievable structure diversity of TAME surpassed that of the traditional studies using multilayer electrodeposition, since the TAME utilizes three-dimensional material growths. An automated dual-bath deposition system was designed to achieve thick ( $>100\ \mu\text{m}$ ) multilayer structures comprising multiscale (10~1000 nm) nanostructures. The multilayer growth was modeled assuming the growth was spatially isotropic while the rate was constant throughout the deposition. In general, this hypothesis was acceptable; the prediction of the final patterns resulting from a three-dimensional multilayer growth was feasible. Non-ideal aspects of the multilayer growth were characterized to explain the discrepancies between the model and the actual growth.



## CHAPTER 3

### TAME-BASED SURFACE HIERARCHICAL STRUCTURES

#### 3.1 Backgrounds and Motivation

Multilayer electrodeposition, combined with conventional microlithography is an economic route to form surface structures comprising heterogeneous metallic layers of micro-, or nanoscale individual layer thicknesses. Three-dimensional structures with suspended electrodeposited layers are fabricated by a timed, selective etching of either metal layers from deposited multilayer structures. Selective etching of Fe-rich layers, from the multilayer structures comprised of Fe-rich layers sandwiched by nickel-rich layers, is studied (Figure 3.1(a)) [48] to result in the suspended structures. Similar structures have been fabricated based on a nickel (Ni)/copper (Cu) multilayer deposition followed by a selective removal of either nickel (Figure 3.1(b)) or copper; the selective removal is achieved either electrochemically [49], or chemically [31]. Batteries (Figure 3.1(c)) and capacitors exploiting the high surface-to-volume ratio of the suspended multilayer structures have been fabricated and characterized. These surface hierarchical structures are realized based on a one-dimensional, through-mold electrodeposition.

The TAME process extends this approach by utilizing three-dimensional growth. In this chapter, the route to various TAME surface hierarchical structures and their applications are discussed. Selected applications of such structures (i.e. nanoscale pattern transfer, superhydrophobic films) are demonstrated.

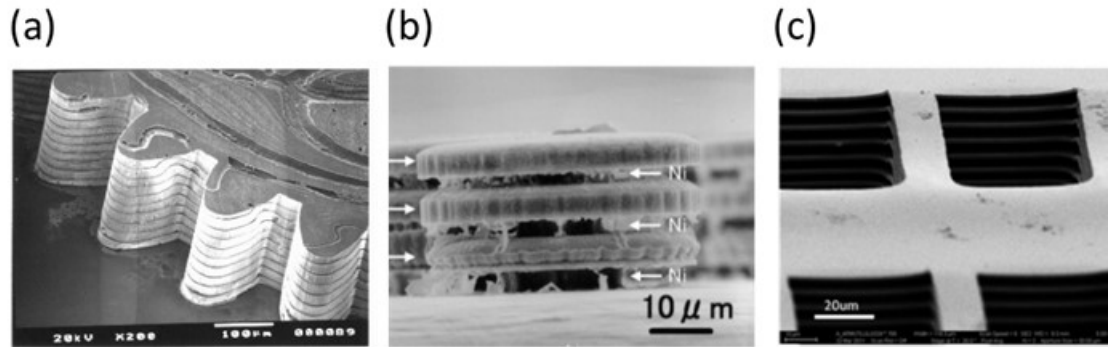


Figure 3.1 Surface structures fabricated based on electrodeposited multilayers. (a) NiFe multilayers with etched Fe-rich layers [48], (b) Ni/Cu multilayers with Ni being selectively etched [49], (c) Ni/Cu multilayers with Cu being selectively etched. The metallic scaffolds are used as a battery electrode [50].

### 3.2 Structures Based on Three-Dimensional Electrodeposition

The TAME process based on three-dimensional multilayer structures is detailed below. Template fabrication begins by preparing an insulating substrate; a silicon wafer is coated by a 1  $\mu\text{m}$ -thick silicon dioxide or a 250 nm-thick PMMA layer, as a sacrificial insulating layer. A conductive seed layer, typically copper (Figure 3.2(a),(b),(d)) or nickel (Figure 3.2(c)), is defined on the sacrificial layer. The seed layer is an electrically connected group of meshes with evenly spaced, uniform micrometer-scale “openings”. Depending on how a seed layer is defined on the substrate, the templates are categorized into two types. The seed layer of a Type 1 template is patterned either by a subtractive process (i.e. Ti (30 nm)/Cu (5000 nm~1  $\mu\text{m}$ )/Ti (30 nm) sputtering followed by a wet chemical etching (Figure 3.2(a),(b)) or an additive process (i.e. through-mold electrodeposition of nickel (Figure 3.2(c)). The seed layer of a Type 2 template is defined by patterning an additional sacrificial photoresist layer on the copper layer (Figure 3.2(d)), thereby masking portions

of the copper layer with nonconductive photoresist. A multilayer electrodeposition process follows; the desired individual layer thicknesses are defined by controlling the individual layer deposition time. The conformal, three-dimensional deposition is continued until at least the exposed insulating surfaces of the microscale openings are completely covered. The deposition may continue beyond this point to thicken the multilayer.

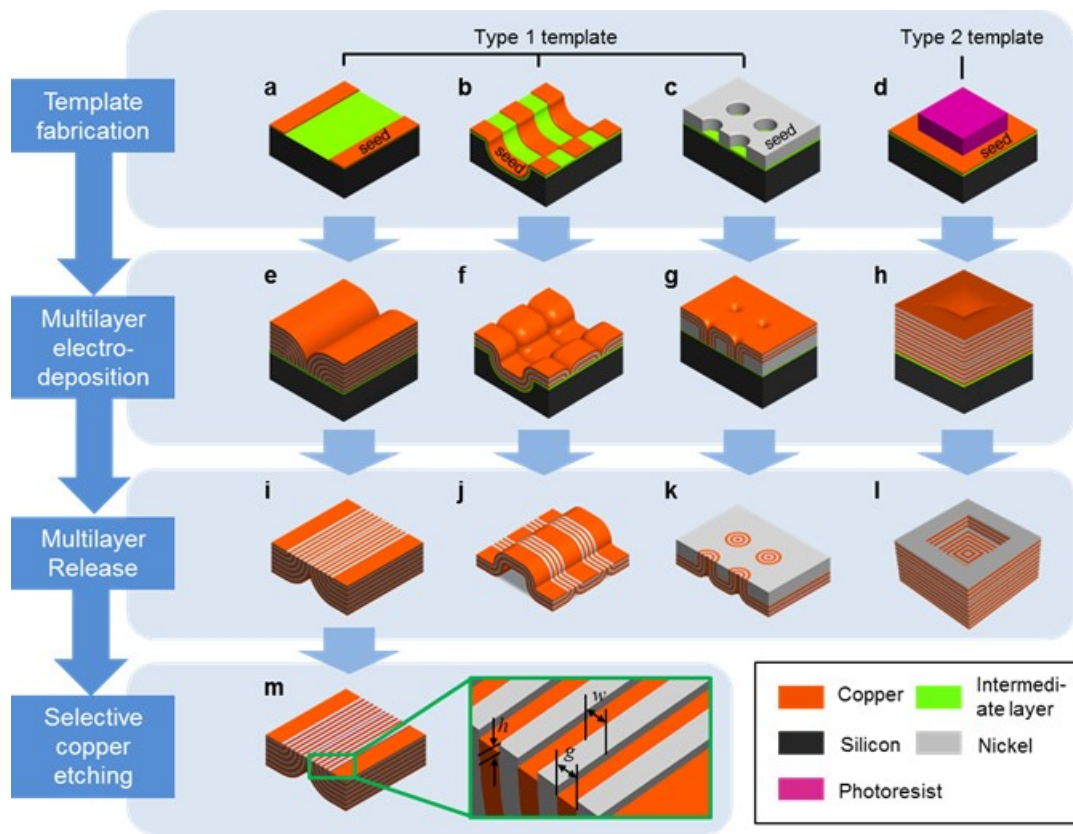


Figure 3.2 TAME process based on three-dimensional multilayer electrodeposition.

Post-deposition, the multilayers are released from the substrate (Figure 3.2(i)-(l), note that the figures are flipped upside down). This is achieved either by a complete removal of the insulating sacrificial layer (e.g. removal of silicon dioxide layer using concentrated hydrofluoric acid), or peeling off the multilayer structure from the sacrificial layer using a tweezer. The latter is preferred since the multilayers could be rapidly released from the substrate regardless of their size and design; in this case, soft-baked PMMA (950 PMMA A4, MicroChem, baked at 180 °C for 2 min) is an appropriate choice as the sacrificial layer, since the adhesion between the patterned seed layer and the PMMA film is sufficiently strong to withstand the built-in stress of the deposited multilayers, yet still sufficiently weak to allow the deposits to be peeled off from the substrate with ease. These release processes do not damage the electrodeposited structure, hence, the revealed surface is smooth ( $R_a < 10$  nm) while the topography inversely replicated from the template is preserved.

A subsequent, timed selective copper etch defines the elevation of the nickel with respect to the copper ( $h$ ) (Figure 3.2(m)), thereby forming a surface relief structure. The widths of protrusions ( $w$ ) and trenches ( $g$ ) correspond to the individual thicknesses of nickel and copper (that are denoted as  $w_{Ni}$  and  $w_{Cu}$  in Chapter 2), respectively. In general, the cross-sections of the protrusions as well as the trenches are nearly rectangular when  $h$  is similar to, or smaller than  $w$  and  $g$ . The relationship between the deposition/etching parameters and the widths of the nanostructures ( $w, g$ )/heights of the nanostructures ( $h$ ) is summarized in Figure 3.3. The growth rates of nickel and copper at typical current densities of  $10 \text{ mA cm}^{-2}$  and  $15 \text{ mA cm}^{-2}$  are  $2.58 \text{ nm s}^{-1}$ , and  $4.24 \text{ nm s}^{-1}$ , respectively. The copper etch rate of the thiourea-based etchant is  $\sim 100 \text{ nm/minute}$ .

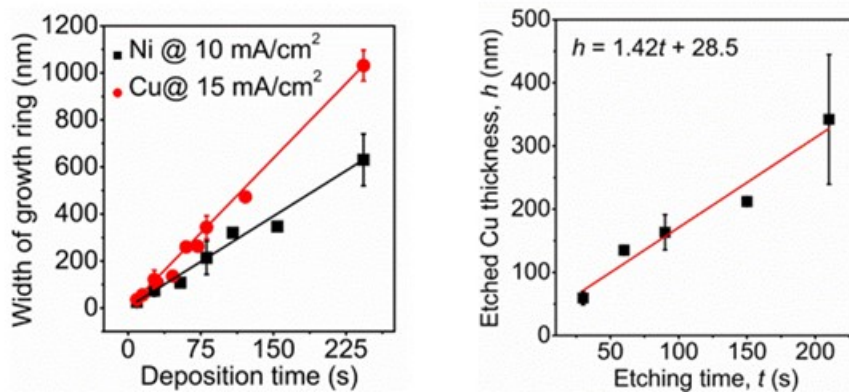


Figure 3.3 Widths of the growth rings as a function of individual layer deposition time (error represents  $\pm$ three standard deviations); etched copper thickness as a function of etching time (error represents  $\pm$ one standard deviation).

The TAME process is a scalable approach to nanostructures, since the nanostructures are simultaneously grown from every part of the seed layer that is distributed over an area of arbitrary size. Nanopatterned surfaces with large surface areas (up to 50 cm<sup>2</sup>) is produced through a few hours of multilayer deposition, since the processing time is defined by minimum total multilayer thickness required to laterally deposit over the desired insulating surfaces exposed through the meshed seed layer, regardless of the desired total nanopatterned surface area. Based on the TAME process, nanostructures of high spatial densities are arranged within lithographically designed positions while their geometries and sizes are controlled. The categories of achievable TAME structures based on the three-dimensional multilayer growth are discussed below.

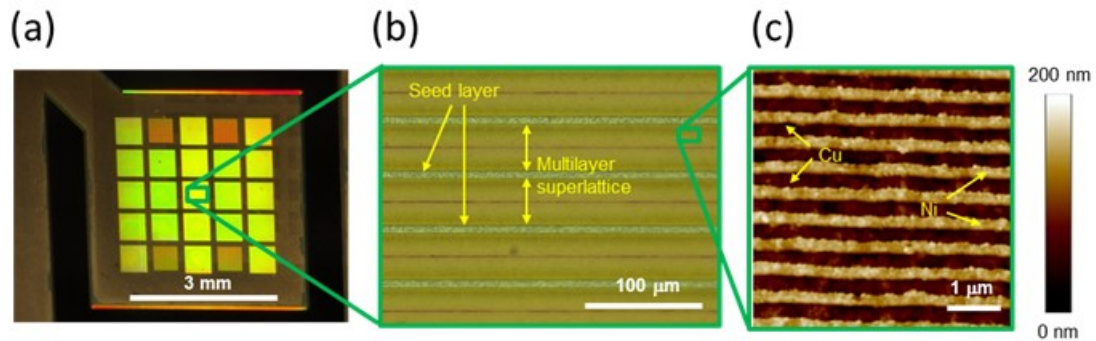


Figure 3.4 Planar surface relief structures based on TAME process using a Type 1 template. (a),(b) Optical and (c) AFM images of released and etched multilayer structures.

Planar TAME structures are fabricated using a Type 1, planar template (Figure 3.4) without any pre-defined topography. A single sample die is shown in Figure 3.4(a); twenty identical samples are fabricated in a single TAME process. Each spacing between a pair of seed patterns ( $40\ \mu\text{m}$ ) is occupied with 75~80 periods of Ni/Cu ( $w = 200\ \text{nm}$ ,  $g = 300\ \text{nm}$ ,  $h = 75\ \text{nm}$ ) (Figure 3.4(b),(c)) that are formed within the multilayer deposition.

Non-planar TAME structures having size-hierarchical topography are fabricated using a Type 1 non-planar template, or a Type 2 template. Figure 3.5 (a)-(c) shows the nanoscale features achieved based on the multilayer structures fabricated through the process depicted in Figure 3.2 (b),(f),(j), that are independently oriented with respect to the microscale topography inversely replicated from the template. Small defects can be formed at the centers of the each nanostructure array of which sizes are defined by the depth of the pre-defined microstructures and the orientation of the patterned seed layer with respect to the microstructures, as depicted in Figure 3.5(d). On the contrary, Figure 3.5(e),(f) shows

structures obtained through the process depicted in Figure 3.2(d),(h),(l), that are inherently concentric and self-aligned to the replicated topography.

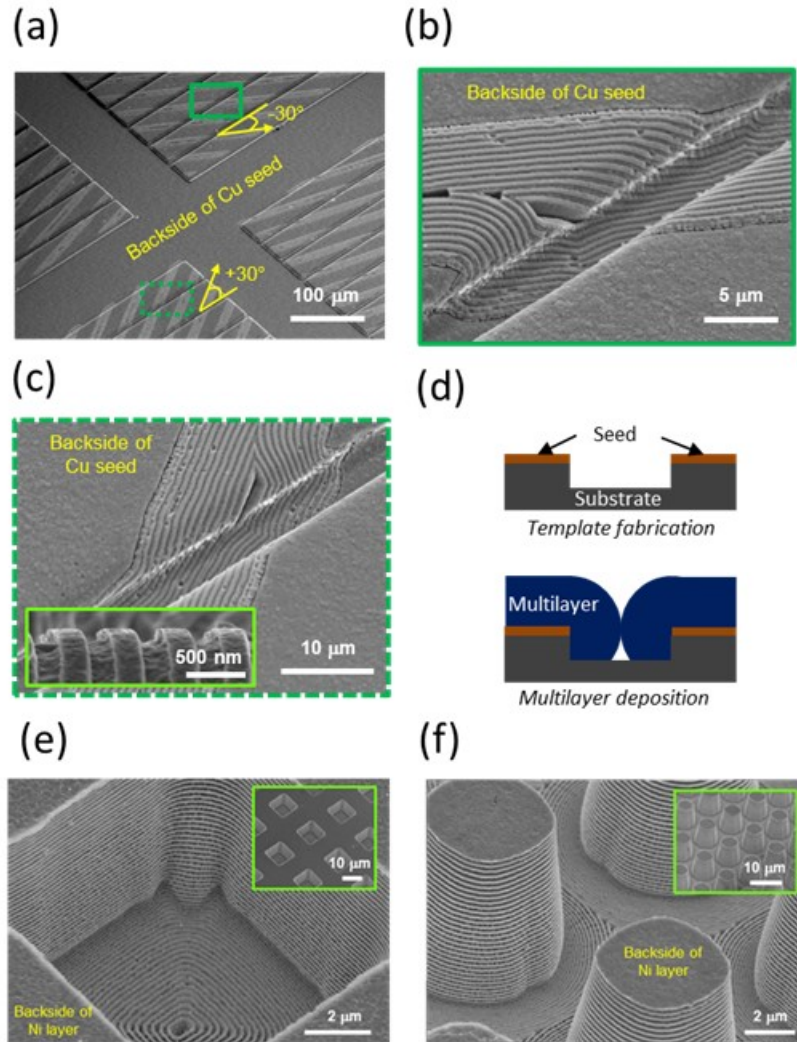


Figure 3.5 Non-planar TAME structures. (a)-(c) Surfaces from a non-planar, Type 1 template ( $w = 250$  nm,  $g = 250$  nm,  $h = 160$  nm). The nanostructures (light grey) shown in the top and bottom part of (d) are oriented  $-30^\circ$  and  $+30^\circ$  with respect to the larger-scale topography, respectively. (b) and (c) are magnified images of (a). (d) Defect formation within the merged multilayers. (e), (f) Nanopatterned surfaces from a Type 2 template ( $w = 50$  nm,  $g = 125$  nm). The insets show low magnification views.



For both types of hierarchical structures, nanoscale features can be defined not only on the planar surfaces, but also along the sidewalls that are rounded (Figure 3.5 (a)-(c)) or nearly vertical (Figure 3.5(e),(f)). Note that the throughput of such sidewall patterning using standard focused ion beam milling is relatively limited due to its serial nature.

The structural diversity can be further improved by employing various three-dimensional template structures created by established techniques (e.g. V-shaped silicon trenches formed by anisotropic, potassium hydroxide etching, thermally-reflowed photoresist structures, and angled photoresist structures achieved by grey scale photolithography). In addition, nanostructures with high structural aspect ratio can be achieved by a selective removal of copper through the desired volume of the material. In particular, vertically aligned “nanowall arrays” are demonstrated based on thick, through-mold electrodeposited nickel as a seed layer. Vertical orientation of the nanostructures is achieved even for such tall structures, since the removed thickness of the copper is smaller than the thickness of the seed layer (Figure 3.6). Nanostructures with aspect ratios higher than 1:100 (Figure 3.6(c)) can be easily fabricated.

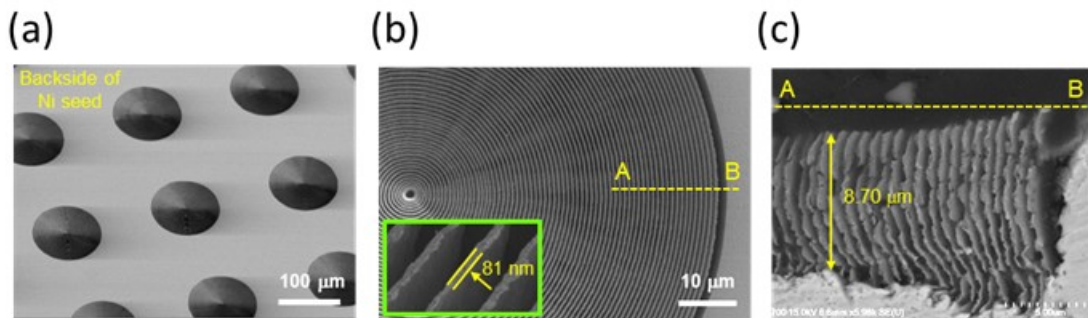


Figure 3.6 Vertically-aligned nanowalls ( $w = 80$  nm,  $g = 500$  nm,  $h = 8$  μm). (b) is a magnified, topside view of (a). (c) is a cross-sectional view of A-B shown in (b).



From the perspective of nanofabrication technology, the TAME process offers a few advantages compared to conventional, beam-based lithography: First, TAME-based nanofabrication is scalable; second, nanopatterns can be formed on non-planar surfaces; third, structures of very high aspect ratios are easily synthesized (although the stiction between the nanostructures may limit the ultimate achievable aspect ratio). Restrictions on the TAME process include that non-conductive materials cannot be utilized as the multilayer materials, and therefore the surfaces directly achieved from this process are mostly limited to metals; however, subsequent, post-deposition processes could be employed to achieve functional surfaces with improved material diversity.

### **3.3 Application: Nanoscale Pattern Transfer**

#### **3.3.1 Backgrounds and Motivation**

Nanoscale pattern transfer techniques, such as nanoimprinting [6] and nanoscale polymer replication [51], are scalable top-down routes to nanofabrication. However, the fabrication of a master mold still relies on the use of costly nanolithography tools, such as EBL. Hence, there have been numerous attempts to perform nanoscale pattern transfer using structures achieved directly from bottom-up approaches. For an example, self-organized, wrinkled polymer substrate can be used as a master mold for a soft lithography process [52]. TAME process is an excellent route to representative pattern transfer techniques since nanostructures with predictable geometries, positions, and orientations can be formed without standard nanolithography. By using the multilayer structures as master molds, the TAME structures could be translated into desired materials, thereby greatly improving the versatility of TAME-based processes.

### 3.3.2 Nanoimprinting

A nanoimprinting process uses physical contact between a master mold and a layer of polymer resist to create a thickness contrast within the resist. This contrast can be translated into the underlying substrate by subsequent etching steps. Nanoimprinting can be categorized into a few types, such as thermal imprinting [26], room temperature imprinting [53], and UV-imprinting [54]; because the TAME structures are opaque, the last option is not available unless the structures are replicated into a UV-transparent material (such as PDMS). Planar TAME structures (Figure 3.4) with nanopatterned area larger than 1 cm<sup>2</sup> are utilized as imprinting master molds.

A thermal nanoimprinting process is performed using a commercially available imprinter (NX2600, Nanonex). A multilayer structure freshly released from the substrate undergoes a copper selective etch to create nickel protrusions of moderate vertical aspect ratio (1:1~2:1). A nanoimprinting resist (NXR 1025, Nanonex) is spun-cast to form 125 nm~250 nm-thick coating. After the nanoimprinting resist is applied to a silicon substrate and soft-baked, the imprinting is performed at 133 °C, 350 psi for 5 minutes. The temperature is set approximately 80 °C higher than the glass transition temperature of the resist (~55 °C). The result is the imprint resist being detached from the substrate, and transferred to the master almost completely. Figures 3.7(a), (b) show the transferred resist before, and after a reactive ion etch (RIE); it is interesting that the surface of the nickel protrusions can be electrically isolated from each other. This could be a useful template for nanowire fabrication based on an edge-selective electrodeposition [55]. However, such resist transfer is undesirable for nanoimprint lithography.

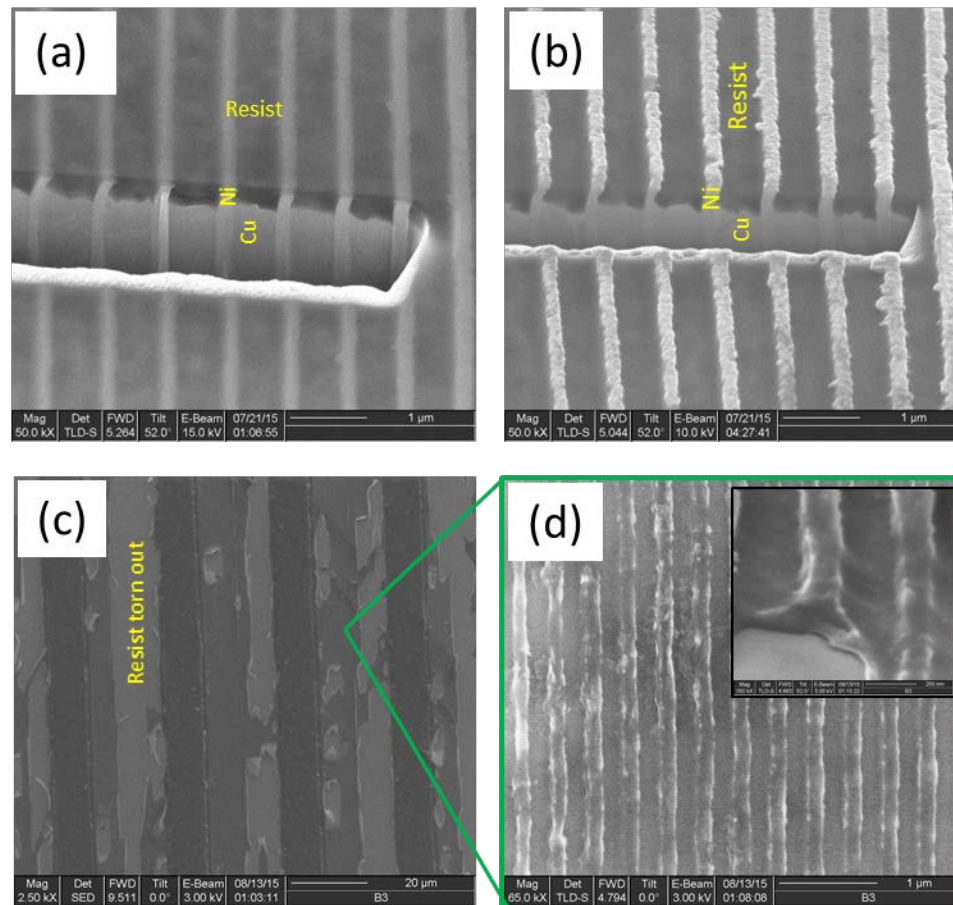


Figure 3.7 Thermal nanoimprinting. (a) NXR 1025 Imprint resist completely transferred to the mold. (b) Ni protrusions exposed after the RIE. (c) Imprinted resist partially torn out from the substrate. (d) Magnified images.

Since such de-molding issues are common in pattern transfer techniques, many approaches have been developed to decrease the surface energy [mN or N/m] of the mold surface, and thereby, facilitate the separation of the master and the resist [51, 56-60]; this is achieved by applying a mold release agent to the mold by various means (e.g. spin coating [57], vapor priming [51]), so that a very thin film with low surface energy is created on the mold. Note that the thicknesses of these films should be as small as possible, in order

to not change the mold geometry by the film deposition. Vapor deposited, tridecafluoro-1,1,2,2-tetrahydrooctyl-1-trichlorosilane (TFOCS) is used as a mold release agent [51]. An oxygen plasma before the silanization is performed since it is known to increase the density of covalent bonding sites between the surface and the evaporated silane [58]. The decomposition temperature for this compound is relatively high ( $> 350\text{ }^{\circ}\text{C}$ ), and therefore, the coating is stable at the imprinting process temperature. A few drops of TFOCS are dropped inside a vacuum chamber, while the sample is attached under the lid upside-down. The vacuum is held for more than 30 minutes. After the sample is taken out from the chamber, it is rinsed in DI water for around 10~30 seconds to remove the excess amount of the deposited silane. After the process, the surface of the multilayer is hydrophobic (Water contact angle =  $110^{\circ}$ ). The nanoimprinting results with the TFOCS-treated sample are only partially successful; a significant portion of the resist is torn off from the substrate (Figure 3.7(c),(d)). The relatively poor imprinting quality may result from the orientation of the protruded nickel partially deviating from being normal to the surface (This can be observed from Figure 3.7(a)).

As an alternative, room temperature nanoimprinting has been performed. This process is originally developed for imprinting a material coated on a temperature-sensitive substrate (e.g. Mylar)[53]. A softer polymer resist, LOR 3A (MicroChem), is employed for this purpose. It is natural that a relatively high pressure is required during the process since the polymer resist is not liquefied during the process. Metallic TAME structures are suited to such a process since they are relatively robust and mechanically flexible compared to silicon masters.

A TAME master mold is used to form an imprint within a 250 nm-thick LOR resist (soft baked at 150 °C for 1 min). A press is used to induce approximately 10 MPa on the master mold. The resulting imprint (Figure 3.8) is almost perfect without negligible part being damaged from the de-molding although the master mold is not treated in TFOCS. Straight (Figure 3.8(a),(b)), as well as rounded features (Figure 3.8(c)) are clearly visible through the entire area (1.5 cm<sup>2</sup>) of the imprint.

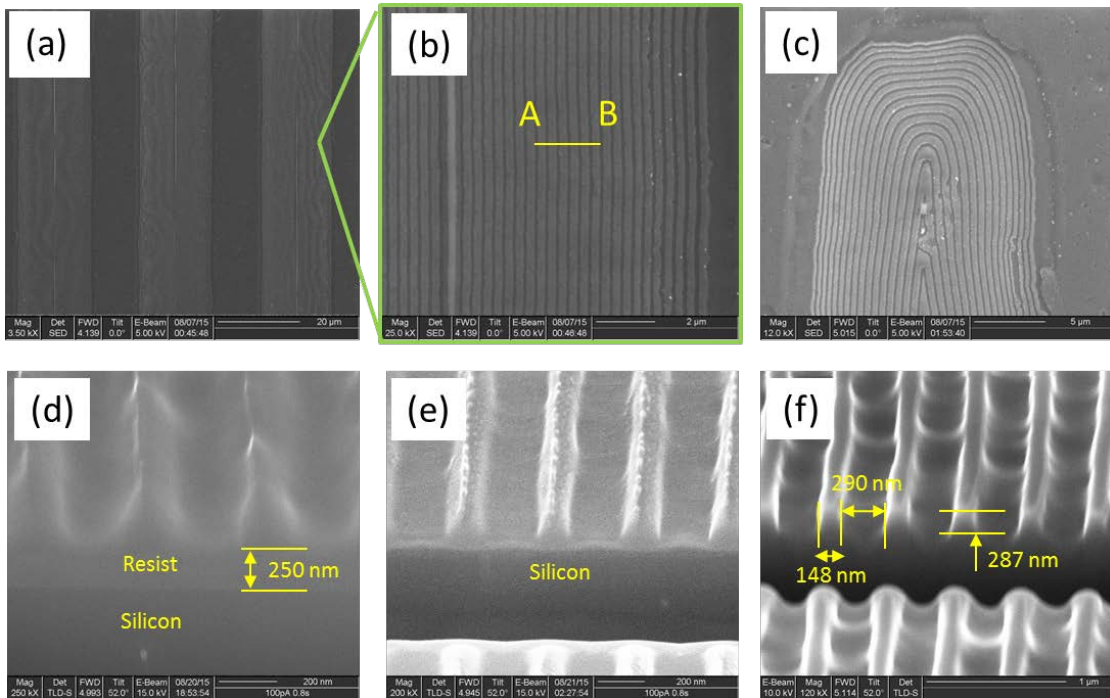


Figure 3.8 Room temperature nanoimprinting. (a)-(c) Top view. Cross-sectioned view between A-B, (d) before and (e) after the RIE. (f) Etched silicon substrate.

The clean de-molding is attributed to the minimal adhesion between the resist and the mold due to the resist not being fully liquefied. Such patterns could be transferred to

the underlying substrate through the removal of the residual resist (Figure 3.8 (d)) using an anisotropic oxygen RIE. After the silicon surfaces are exposed, the silicon is etched via  $\text{CH}_3$  chemistry to demonstrate nanoimprint lithography (Figure 3.8(e),(f)). Considering the geometry of the master mold, the protrusion widths of the patterns transferred to the silicon substrate should be 257 nm, which is approximately 100 nm larger than the measured widths from the actual sample (Figure 3.8(f)). This is mainly because of the residual layer being relatively thick (250 nm). The width of a pattern has laterally decreased by 50 nm from each side during the residual layer removal, although the oxygen RIE process is anisotropic. The thickness of the residual layer after an imprint process could be reduced by (1) using a resist layer with optimized thickness and (2) securing a conformal contact between the master and the substrate during the process. .

### **3.3.3 Replica Molding**

PDMS replica molding is a representative pattern transfer technique; the resulting soft replica are not only useful in subsequent nanofabrication processes (e.g. soft lithography, UV-imprint lithography [51]), but also in creating functional devices (e.g. superhydrophobic surfaces, nanofluidic channel for DNA sequencing). The characteristics of PDMS are suited to micro/nanoscale replica molding; the cured PDMS exhibits (1) low surface energy (22~25 mN/m [61]), and it is (2) elastomeric in nature. In addition, the volume of uncured PDMS does not significantly change after the curing process since the material does not contain solvents. PDMS is highly air-permeable; the air trapped between the dispensed PDMS and the substrate can be easily de-gassed, allowing a nearly perfect replication of complicated substrate topography.

The molding process is performed using a Sylgard 184 A/B kit (Dow Chemical). The “A” and “B” resin and crosslinking components are mixed (weight ratio = 10:1) and de-gassed in a vacuum chamber. The mixture is poured on a TAME master and cured at 70 °C at least 4 hours. The cured PDMS film is carefully peeled off from the master. A Type 1 planar multilayer structure with small nanostructure height is utilized for the molding ( $w = 400 \text{ nm}$ ,  $g = 400 \text{ nm}$ ,  $h < 100 \text{ nm}$ ) (Figure 3.9(a),(b)). The replication is achieved without any issues (Figure 3.9(c),(d)).

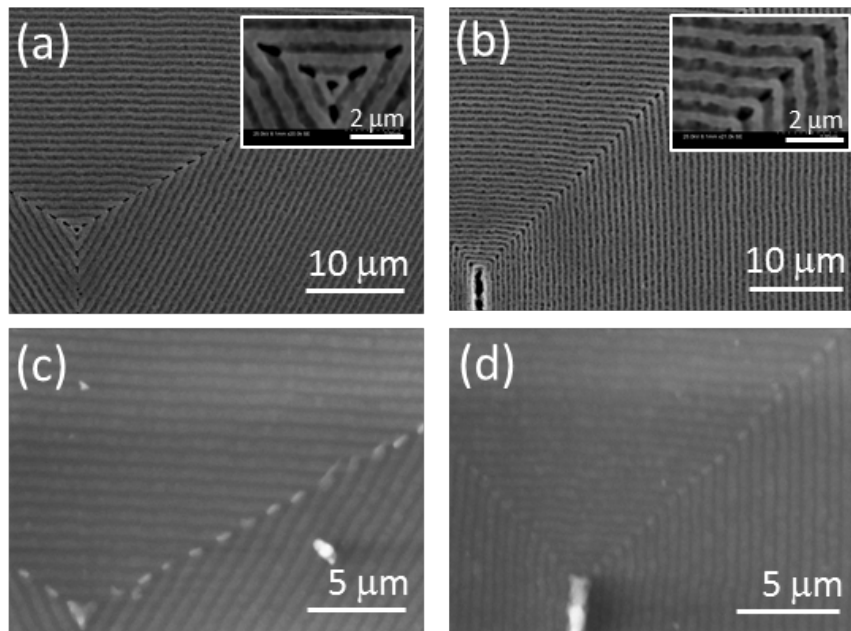


Figure 3.9 PDMS molding using planar TAME structures (a), (b) Master molds after the replication. (c), (d) Respective replica.

Typically, nanostructures with low aspect ratio (as shown in Figure 3.9(a),(b)) are precisely replicated. This can be confirmed from the rough features of the protrusions of the molded

PDMS, that result from the surface roughness of the etched copper of the master (Figure 3.9(c),(d)).

However, when the molding is performed with the multilayer structures with larger nanostructure heights (e.g.  $w = 300$  nm,  $g = 300$  nm,  $h = 500$  nm), or in other words, larger vertical aspect ratios, the replication may not be successful. The nanoscale features are replicated either imperfectly (the structure height significantly less than expected while the corners being rounded, Figure 3.10(a)), or deformed during de-molding (Figure 3.10(b)). Similar reports have been already presented; one main reason of imperfect PDMS trench filling (which results in an imperfect replication) is known to be the high viscosity of PDMS. The replicated PDMS nanostructures tend to deform easily (especially during the de-molding process), and stick together due to its low modulus [62].



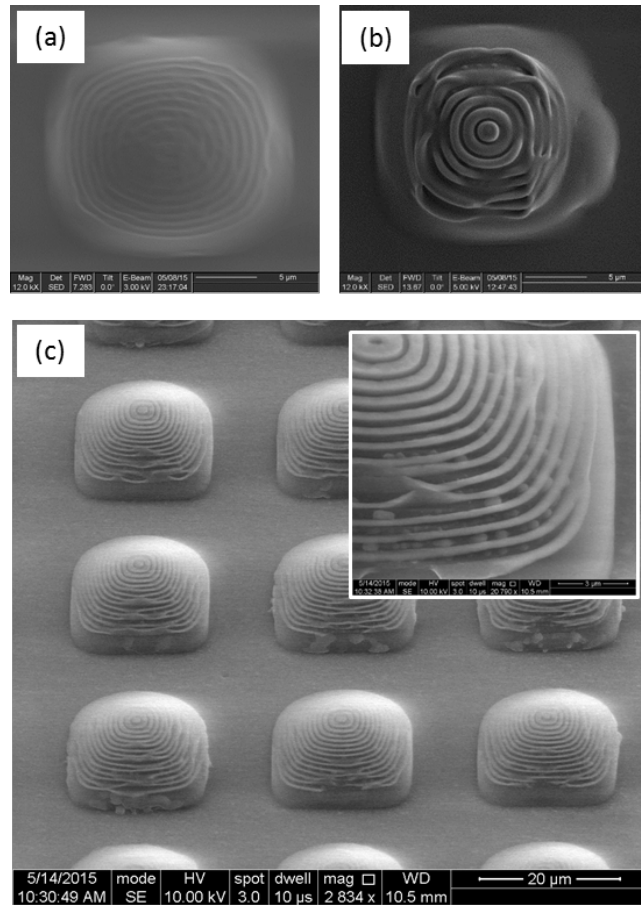


Figure 3.10 Molding results with (a), (b) conventional soft PDMS (top view) and (c) h-PDMS.

Table 3.1 Mechanical properties of soft and hard PDMS.

| Elastomers           | Tensile modulus (MPa) | Elongation at break (%) | Toughness (MPa) |
|----------------------|-----------------------|-------------------------|-----------------|
| s-PDMS (Sylgard 184) | 1.8                   | 160                     | 4.77            |
| h-PDMS               | 8.2                   | 7                       | 0.02            |

A solution to these issues is to use the PDMS with relatively higher Young's modulus, which is referred to as hard PDMS, or h-PDMS. The physical properties of both types of PDMS are listed in Table 3.1 [62]. The Sylgard PDMS is referred to as "soft PDMS" or s-PDMS to differentiate from h-PDMS. h-PDMS is frequently used to fabricate elastomeric master stamps for nanoimprinting, or transfer printing. Sub-100 nm structures that are initially patterned within a silicon wafer can be accurately replicated into h-PDMS. h-PDMS alone suffers from the demolding issue, since it is easily cracked during the process (because of its low elongation at break and mechanical toughness); hence, a composite molding process based on a thin, spun-cast h-PDMS and a thick (~3 mm) soft PDMS is generally accepted as a method to achieve h-PDMS replica without any demolding issues [62].

h-PDMS molding is performed to create hemispheric hierarchical surface structures; the master mold design is identical to the one used to create the structures shown in Figure 3.9(a), (b). The molding begins with an h-PDMS precursor preparation. After 3.4 g of (7-8% vinylmethylsiloxane)-(dimethylsiloxane) copolymer, 2 drops of 2,4,6,8-tetramethylcyclotetrasiloxane, 1 drop of platinum divinyltetramethyldisoxane (dissolved in xylene) is thoroughly mixed and de-gassed, a single gram of (25~30% methylthydrosiloxane)-(dimethylsiloxane) copolymer (i.e. crosslinker) is added. The mixture is immediately dispensed on the multilayer structures, and a short vacuum infiltration (1~3 min) follows to ensure the infiltration of the polymer into the nanostructures. Then, the sample is spun at 1000 rpm, so that the resulting h-PDMS is around 30  $\mu\text{m}$  thick. The sample is baked in an oven at 55  $^{\circ}\text{C}$  until the h-PDMS is cured, yet still tacky on the surface (5~8 min). The pre-vacuumed s-PDMS is poured on to the

cured h-PDMS, and the sample is baked for 4 hours at 70 °C in addition. Demolding is performed manually while the sample is still warm [62]. The resulting structures show microscale protruded structures of which widths and heights are nearly identical to that of the sacrificial photoresist structures patterned on the template. The nanostructures of the h-PDMS replica show sharp corners, and they do not collapse together even though some of the structures are bent due to the shear stress induced during the demolding (Figure 3.10(c)).

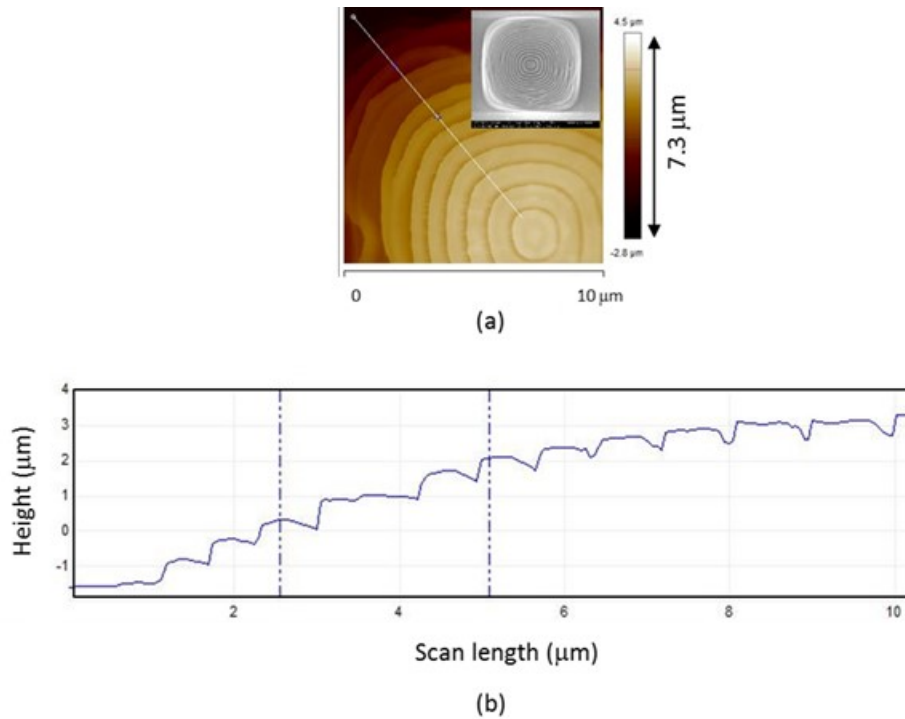


Figure 3.11 AFM scan of dual-scale h-PDMS structures

It should be noted that the detailed characterization of such hierarchical structures is not trivial due to their complex architectures. An AFM scan is performed on the resulting dual-scale topography (Figure 3.11). The average pitch of the nanostructure pitch can be

determined by the number of the nanoscale protrusions and the hemispheric geometry of the microstructures (for example,  $\overline{w + g} = 790$  nm for the presented structures). The height of the nanostructures ( $h = 450\sim 500$  nm) can be determined using AFM scanning; note that the correct depth measurement is possible only from the trenches formed at the topside of the microstructures. The measurement difficulties further increase for the structures with higher aspect ratio (i.e. nanoscale, narrow trenches and extruded protrusions). The approaches to characterize such structures (e.g. laminations) are further detailed in Chapter 4.

### **3.3.4 Summary**

In summary, the nanoscale features of the TAME structures were successfully transferred to a number of common materials used in micro/nanofabrication (e.g. imprint resists, soft and hard PDMS). Room-temperature nanoimprinting was developed to pattern substrate materials. Apart from the imprinting-based lithography, direct material transfer using multilayer master molds will be an appropriate approach for nanopatterning. Planar, and non-planar hierarchical PDMS structures were replicated from the multilayer master molds. h-PDMS was used to replicate nanostructures with moderate aspect ratio (1:1~2:1), where using conventional PDMS was not a proper option.

## **3.4 Application: Superhydrophobic Surfaces**

### **3.4.1 Backgrounds and Motivation**

Superhydrophobicity is known to be essential for the survival of many biological systems. This property is usually characterized by an exceptionally high water contact

angle ( $> 150^\circ$ ) with a low sliding angle ( $< 10^\circ$ ), i.e., the angle at which a droplet (of a certain volume) starts to roll-off from the surface. For an example, superior water-repellence of a lotus leaf efficiently removes any dirt deposited on the surfaces [63] with water droplets being rolled-off from them; this is referred to as “self-cleaning.” Also, the superhydrophobic nature of a water strider’s legs allows them to move on the water surface [64]. Such water repellent characteristics are beneficial for commercial applications that are designed to interact with outdoor environments. For example, a superhydrophobic coating on a solar cell will prevent the device from the gradual degradation of the conversion efficiency resulting from the deposited dusts, or dirt [65]. Due to its practical importance, there has been an extensive effort not only to understand the origin of this property, but also to synthesize such surfaces in an economic manner. To achieve a superhydrophobic surface, applying the material with low intrinsic surface energy, as well as controlling its structural texture is important; even with the material with the lowest surface energy ever known (i.e. Teflon, 20 mN/m), superhydrophobicity is not achieved if the material is perfectly smooth [66]. In particular, it has been understood that structures with multi-scale architectures are likely to exhibit “stable” hydrophobicity [67] (the meaning of “stable” in this context will be discussed below). The developed approaches for the realization of superhydrophobic, multiscale structures can also be categorized into the three types: bottom-up/bottom-up, top-down/top-down, and hybrid, analogous to Chapter 1.

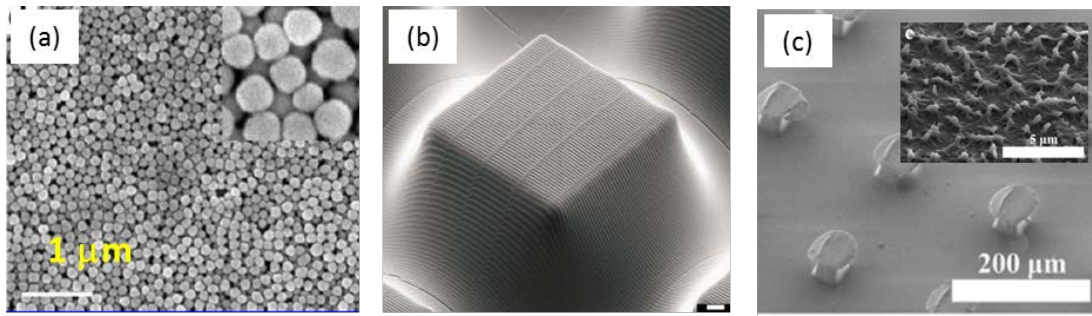


Figure 3.12 Examples of superhydrophobic surfaces. (a) Transparent, fluorosilane coated, silica nanoparticles [68]. (b) Hierarchical structures achieved by dual-scale E-beam lithography [69] (c) UV-curable polyurethane micropillar with anodized aluminum patches (assembled on top of the pillars) [70].

The bottom-up/bottom-up approaches are typically based on the synthesis of particles (e.g. silica) or colloids of desired shapes and sizes (Figure 3.12(a)). The superiority of these approaches lies in their simplicity. Application of such materials to the surfaces with three-dimensional geometries (e.g. meshes) is straightforward, e.g., dip coating or spin coating using an all-in-one solution. However, the resulting surfaces may not be structurally robust enough to retain its water-repellency after undesirable external forces (e.g. abrasion, adhesive tape test) are induced to the surface [68]. Another intrinsic limitation of this approach is that the optimization of the property is relatively difficult due to the spontaneous nature of the synthesis.

The top-down/top-down approaches have been also demonstrated to achieve superhydrophobic surfaces. Both micro- and nanostructures can be directly defined lithographically [69] (Figure 3.12(b)), or through a sequential pattern transfer process using proper masters. For example, the nanostructures can be defined by nanoimprinting on the “pre-imprinted” microstructures (Figure 1.1). Compared to the bottom-up approaches,

these approaches exhibit mainly two advantages: First, they possess higher achievable structural diversity since the geometries of micro- and nanostructures are not restricted by the bottom-up assemblies; second, the relationship between the wettability that result from the specific structure is relatively straightforward. Hence, it is easier for a top-down/top-down approach to create desired structures with designed wettabilities; for example, surfaces with varying wettability in different orientations (i.e. anisotropic wettability [19]), or at different locations (i.e. surface wettability gradient [71]) have been realized. However, the nanostructure fabrication is usually enabled at the expense of the use of conventional nanolithography, and multi-step processing is required to realize size-hierarchy; these are the critical hurdles toward commercialization. A hybrid approach employs a bottom-up assembly for the nanostructures; however, the integration of those structures within the pre-fabricated microstructures still needs additional processes (Figure 3.12(c)).

In summary, the economic, realization of robust superhydrophobic structures is important, as well as achieving superior non-wetting properties. This can be enabled by the TAME process. First, a single-step replica molding using the TAME structures based on a Type 2 templates enables the realization of dual-scale, highly transparent non-wetting structures. By using the TAME structures as hierarchical master molds, and directly replicating the structures via h-PDMS molding, the fabrication process is greatly simplified.

Second, a robust, flexible metallic superhydrophobic structures are directly realized through a surface silanization of TAME master mold structures. Compared to common materials (i.e. silicon, polymer), the metallic surfaces could be useful in relatively harsh

environment applications (e.g. underwater maneuvering with minimized solid-water interface drag [72]).

### 3.4.2 Design and Fabrication

The fabricated TAME structures are either “hole” type (Figure 3.5(e)), or “mesh” type (Figure 3.5(f)) depending on the types of the desired superhydrophobic surfaces. The hole-type structures are used to create hierarchical PDMS structures via replica molding (Figure 3.13(a),(b)). The fabrication of a PDMS hierarchical structure begins with the preparation of a Type 2 template. A 250 nm-thick PMMA is chosen as a sacrificial layer. The seed layer is a sputtered sandwich of Ti(30 nm)/Cu(6000 nm)/Ti(30 nm). The thicknesses of the photoresist (AZ 4620, Shipley) layers can be varied between 8  $\mu\text{m}$ ~30  $\mu\text{m}$ . As-patterned photoresist pillars exhibit nearly vertical sidewalls; however, the template can be heated at 150 °C for 5 min to reflow the photoresist, and thereby, achieve rounded topographies. Multilayer deposition follows until the all the insulating surface is covered. After the multilayer structure is manually peeled off from the substrate, the seed layer is removed by sequential removal of Ti (with a diluted hydrofluoric acid), Cu (with a combination of phosphoric acid-based, non-selective etchant and thiourea-based, copper selective etchant), and Ti. The photoresist is completely removed by sonication in a photoresist remover (Remover PG, MicroChem) at 70 °C for 30 min. An oxygen plasma descum process for 10 min follows to ensure the complete photoresist removal. After the copper is etched as desired in a sonication bath for 1 min, the sample is again oxidized in the plasma chamber, and a silanization of the metal surface is follows thereafter. h-PDMS replication process is performed as discussed in Chapter 3.2.



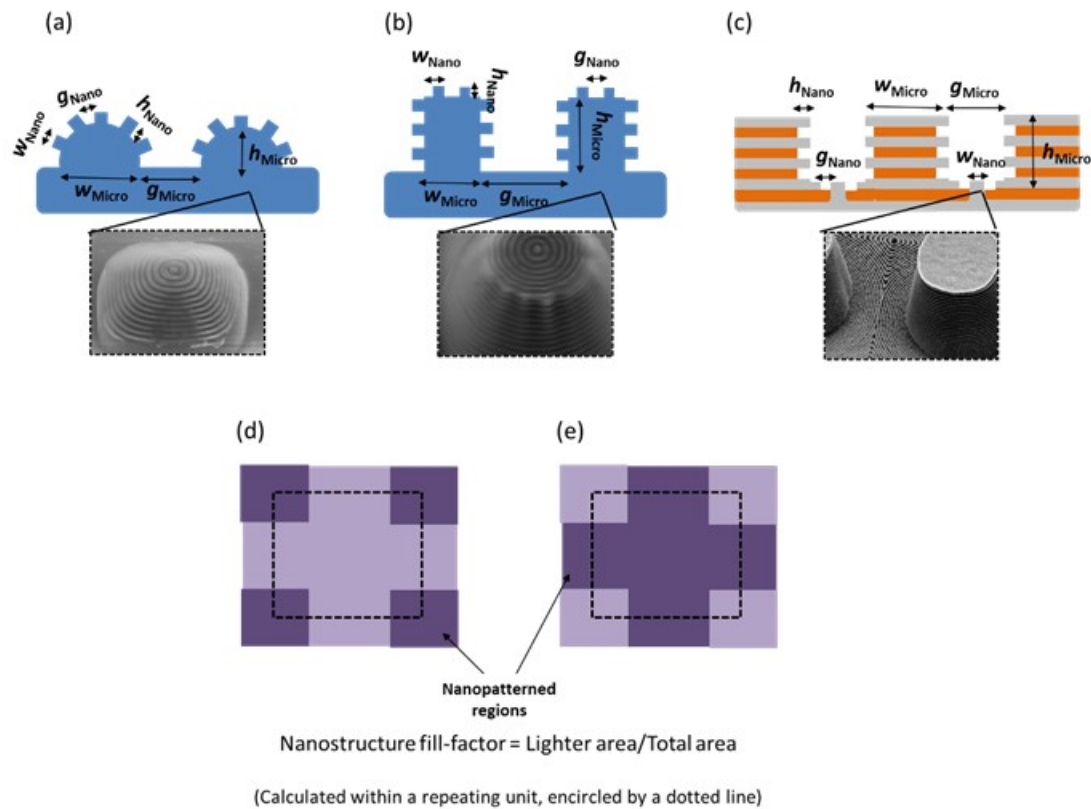


Figure 3.13 Superhydrophobic structures prepared in this experiment. (a) PDMS hierarchical structures with semihemispheric micropillars, (b) PDMS hierarchical structures with rectangular micropillars, and (c) metal hierarchical structures. (d), (e) Depicts the portion of the nanopatterned regions (dark) within PDMS and metal hierarchical structures, respectively.

The hydrophobic metallic hierarchical structures (Figure 3.13(c)) are formed by coating TFOCS on the mesh-type TAME structures. The TFOCS vapor deposition process is performed as described in Chapter 3.2.1.

### 3.4.3 Role of Structural Hierarchy on Non-Wetting Properties

Wetting properties of planar, microscale, and dual-scale structures are characterized to understand the role of structural hierarchy on non-wetting properties. PDMS hierarchical structures with semihemispheric micropillars (Figure 3.13) are replicated from hole-type masters with rounded corners ( $w_{\text{Nano}} = 350 \text{ nm}$ ,  $g_{\text{Nano}} = 350 \text{ nm}$ ,  $h_{\text{Nano}} = 500 \text{ nm}$ ;  $w_{\text{Micro}} = 15 \text{ }\mu\text{m}$ ,  $g_{\text{Micro}} = 15 \text{ }\mu\text{m}$ ,  $h_{\text{Micro}} = 8 \text{ }\mu\text{m}$ ). The samples with identical microscale geometries, but without the nanostructures are fabricated. This is enabled by overplating a single layer of nickel on an identically-designed template, and subsequently performing an h-PDMS replication process; the resulting structures are referred to as “single-scale structures.” The wettability of three types of the surfaces, the h-PDMS surfaces without any features (Planar), single-scale (Micro, or “M”), and hierarchical structures (Micro/Nano, or “MN”) are compared.

One of the easiest methods to determine the wettability of a structured surface is to measure its contact angle on the surface (Automated Goniometer, Model 200, Ramé-hart). If the surface is perfectly chemically homogeneous and smooth, ideally, a single contact angle (i.e. Young’s angle,  $\theta_0$ ) is defined. However, as far as wetting of a textured surface is concerned, more than one local energy minimum exists for the three phase system; in other words, a contact angle may be “chosen” by a droplet among several choices depending on the fraction of the solid-liquid contact area.

When the water droplet is in a complete contact with the solid substrate (Wenzel state, Figure 3.14), the contact angle is calculated as [68],

$$\cos\theta^w = r\cos\theta_0 \quad (3.1)$$

where  $r$  is the actual surface area of the substrate surface over the apparent surface area. On the contrary, the water droplet may sit “on” the protrusion of the roughened substrate, thereby achieving a liquid-solid-air composite state (Figure 3.14); this is referred to as a Cassie state, and the contact angle is calculated as a function of the solid-liquid contact area over the surface area underneath the droplet ( $f$ ) [68].

$$\cos\theta^c = f(\cos\theta_0 + 1) - 1 \quad (3.2)$$

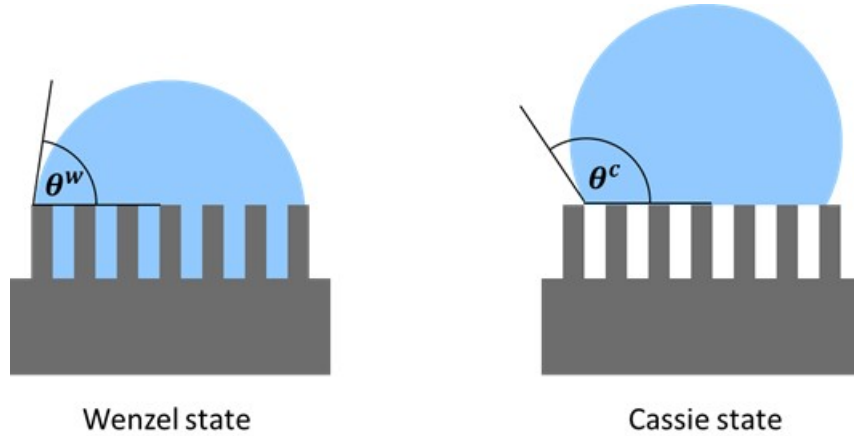


Figure 3.14 A droplet in Wenzel and Cassie states.

Achieving a stable Cassie state is very important for a superhydrophobic surfaces to be practical, because the reduced water-solid contact area leads to the reduced solid-water friction. Consequently, there is more chance for a water droplet to “roll-off” from the surface, which corresponds to self-cleaning [73]. Based on a thermodynamic analysis, it can be shown that the Cassie state is more likely to be energetically favorable compared to the Wenzel state, and therefore, thermodynamically stable, for single-scale surface

structures with (1) smaller periodicities and (2) higher aspect ratios [74]. A hierarchical structure which is comprised of such slender nanostructures hosted on the microstructures is even more desirable since the water-solid contact fraction is drastically decreased due to the presence of the microstructures while high Cassie state stability is still achieved by the nanostructures [67].

This is qualitatively confirmed from the measurement results (Figure 3.15). The SCA on the single-scale microstructures falls within the contact angles predicted by the Wenzel and Cassie models (Table 3.2). This means a stable Cassie state is not achieved with the single-scale structures even at a low liquid pressure ( $\sim 100$  Pa) induced by a droplet with a small volume ( $5 \mu\text{L}$ ). Even though a droplet was in Cassie state (Figure 3.14, right), a small vibration or water pressure would change the state to Wenzel (Figure 3.14, left). On the other hand, high SCA of  $160^\circ$  measured from the hierarchical structures corresponds to the Cassie model. Hence, these structures are likely to exhibit non-wetting, superhydrophobicity. Figure 3.15 shows a cartoon depicts a water droplet on the hierarchical structure, forming a Cassie state.

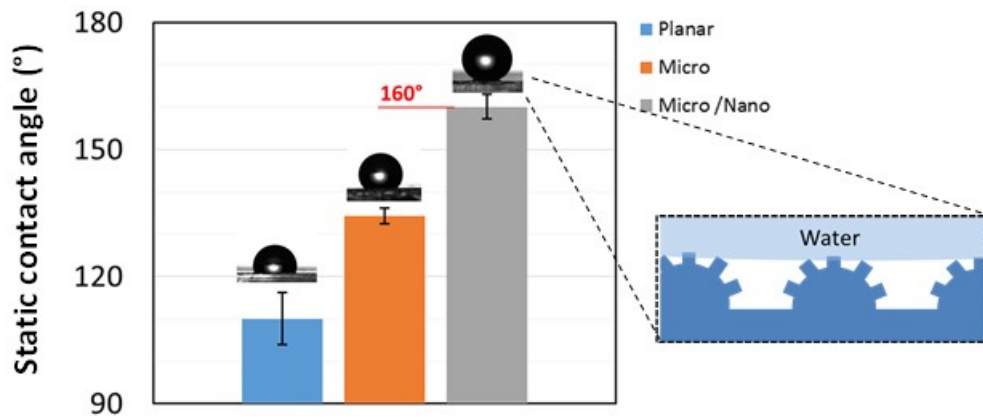


Figure 3.15 Static contact angle comparison between planar, single-scale, and hierarchical structures.

Table 3.2 Calculated static contact angle using Wenzel and Cassie model

|                                   | Micro (°) | Micro/Nano (°) |
|-----------------------------------|-----------|----------------|
| $\theta_0$                        | 110       | 110            |
| $r$                               | 1.53      | 1.75           |
| $f$                               | ~0.25     | ~0.125         |
| $\theta^w$                        | 121.6     | 127.8          |
| $\theta^c$                        | 146.6     | 156.6          |
| <b>Static contact angle (SCA)</b> | 134.4     | 160.0          |

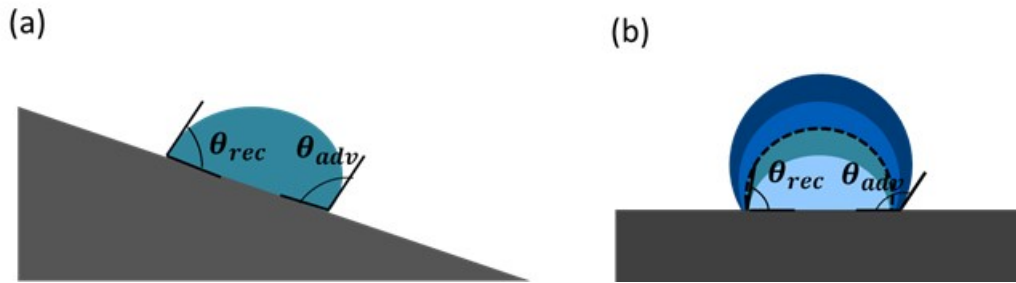


Figure 3.16 Contact angle hysteresis.

Contact angle hysteresis (CAH) is another important metric frequently utilized to evaluate the superhydrophobicity of a surface, because this is directly related to the sliding angle. When a droplet begins to roll down a slope, the angle between the substrate and the droplet-front can be defined, which is referred to as an “advancing angle ( $\theta_a$ )”; similarly, a “receding angle” is defined from the backside of the droplet ( $\theta_r$ ) (Figure 3.16(a)). A more reliable approach to measure an advancing angle, which is employed in this experiment, is to place a droplet (5  $\mu\text{L}$ ) on the substrate and gradually adding a small unit volume of water (0.25  $\mu\text{L}$ ) to the droplet until the contact angle stops increasing (usually the total volume of the droplet exceeds 10  $\mu\text{L}$  at the end of a measurement (Figure 3.16(b)). The volume is gradually reduced in similar fashion until the contact angle stops decreasing; the corresponding angle is regarded as a receding angle. CAH is defined by the difference between the two.

$$\text{CAH} = \theta_a - \theta_r$$

For a droplet that begins to move at a sliding angle ( $\alpha$ ), on top of a smooth, homogeneous surface, the Furmidge equation is satisfied [75],

$$\frac{mg \sin(\alpha)}{w_d} = \gamma(\cos\theta_r - \cos\theta_a) \quad (3.3)$$

where  $m$  [kg] is the droplet mass,  $g$  is the acceleration of the gravity ( $9.81 \text{ m/s}^2$ ),  $w_d$  [m] is the width of the droplet-substrate contact area,  $\gamma$  is the surface tension of the liquid (i.e. water,  $72.8 \text{ mN/m}$ ). Hence, it is natural to conclude that a surface with small CAH would lead to a lower sliding angle (small  $\cos\theta_r - \cos\theta_a$  represents small  $\alpha$ ).

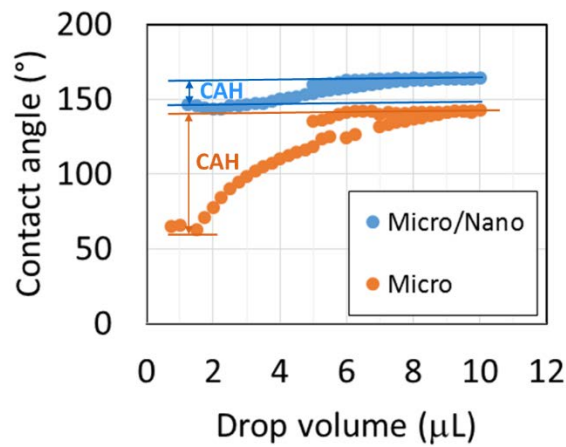


Figure 3.17 Contact angle hysteresis measured from a hierarchical structure.

Figure 3.17 shows how the contact angle changes as the droplet volumes are changed throughout a CAH measurement. A small CAH measured from the hierarchical structure (the same sample measured in Figure 3.15) is a direct proof of the minimized solid-water friction due to a stable Cassie state. In comparison, the CAH measured the

single-scale structure ( $80^\circ$ ) is much larger due to the large friction between the water completely wetting the microstructures.

Sliding angle of a given droplet volume ( $10\ \mu\text{L}$ ) of water on a sample is measured by putting the sample on a custom stage, and manually tilting the stage until the droplet begins to roll. The sliding angle measured on the hierarchical structure is small ( $12^\circ$ ) corresponding to the calculation ( $9^\circ$ ) based on Equation 3.3, while the water droplet on the single-scale structure does not roll-off the sample even after the sample is placed upside down (therefore, the sliding angle cannot be defined). The difference between the calculation and the measured angle may result from the difficulties of estimating  $w_d$  for rough, hierarchical surface, as well as relatively imprecise nature of the manual measurement.

In summary, PDMS structures replicated from proper TAME structures exhibit high SCA ( $160^\circ$ ), low hysteresis ( $\sim 10^\circ$ ) with low sliding angle ( $12^\circ$ ), all three of which are considered as important criteria of superhydrophobicity. Wetting property differences between a singular microstructure and a corresponding hierarchical structure are significant, even though both structures are comprised of the same material, h-PDMS. This shows that the realization of structural hierarchy is crucial for the fabrication of non-wetting surfaces.

#### **3.4.4 PDMS Superhydrophobic Surfaces with Uncompromised Optical Transparency**

TAME based approach enables a single-step realization to superhydrophobic surfaces with important additional functionalities that may be useful in practical applications. The first example is a superhydrophobic film with high optical transparency. For some devices (i.e. hand-held devices, solar cell panels), the coating should not



compromise their optical properties while exhibiting reasonable self-cleaning properties. An approach to satisfy such contradictory requirements is to reduce the portion of the areal projection of the nanostructures, i.e. reduce the nanostructure “fill-factor” (Figure 3.13), by increasing the gap between the microstructures; this is achieved by using a Type 2 template with increased gap between the photoresist pillars. In order to achieve a stable Cassie state with such “sparse” structures, the overall height of the hierarchical structure should be also increased. Therefore, thicker photoresist patterns are used to achieve replica with corresponding microstructures. The patterned photoresist is not reflowed in contrast to the samples shown in the previous chapter. Microstructures of larger height and sharp (i.e. abrupt) corners are effective in achieving highly stable Cassie state without increasing the nanostructure fill-factor.

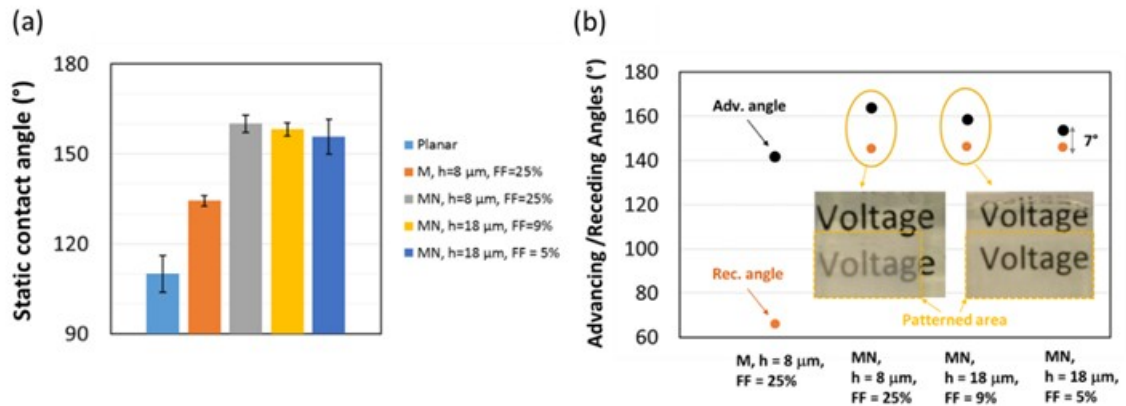


Figure 3.18 SCA and CAH of various h-PDMS structures with different designs. “h,” the height of micropillars ( $h_{\text{Micro}}$ ), FF is an acronym for fill-factor. Nanostructure geometries are designed to be identical for all the samples.

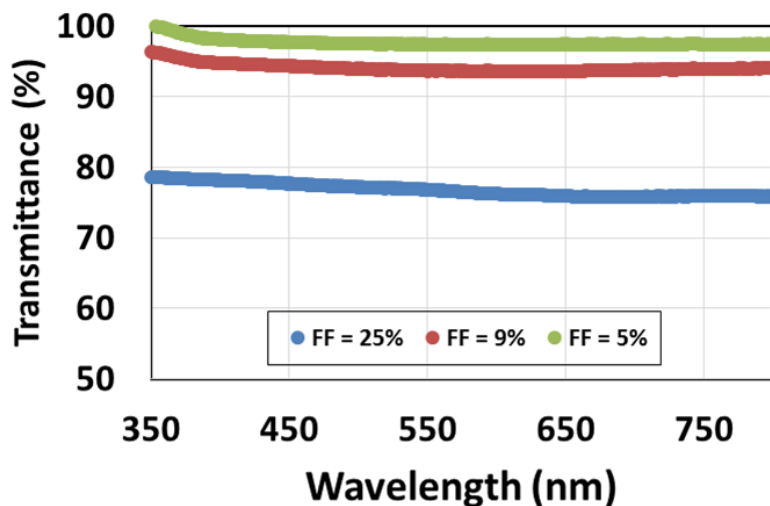


Figure 3.19 UV-vis spectroscopy of the samples with different nanostructure fill-factors. A featureless, planar block of h-PDMS with same thickness (3 mm) is used as the reference.

PDMS hierarchical structures with rectangular micropillars of varying periodicities (and thereby, varying nanostructure fill-factors as defined in Figure 3.13(d)) are fabricated ( $w_{\text{Nano}} = 350 \text{ nm}$ ,  $g_{\text{Nano}} = 350 \text{ nm}$ ,  $h_{\text{Nano}} = 500 \text{ nm}$ ;  $w_{\text{Micro}} = 20 \text{ }\mu\text{m}$ ,  $g_{\text{Micro}} = 40, \text{ or } 60 \text{ }\mu\text{m}$ ,  $h_{\text{Micro}} = 18 \text{ }\mu\text{m}$ ), and their SCA and CAH are analyzed. Figure 3.17 shows that the samples with fill-factor lower than 10% still exhibit high static contact angle ( $> 150^\circ$ ), as well as low hysteresis ( $< 10^\circ$ ); note that the results from the hierarchical structure presented in Figure 3.17 are also plotted together (Figure 3.18, center). Figure 3.18 (b) compares the transparency of the samples with different fill-factors. The letters hidden under the sample with larger nanostructure fill-factor are seen rather dull due to the light being scattered from the hierarchical structures. This is negligible for the structures with lower fill-factor. Optical transparency of the samples is measured using a UV-vis spectroscope, Cary 5000 UV-Vis-NIR, Agilent Technologies (Figure 3.19). The samples with nanostructure fill-factor lower than 10% exhibit transmittance higher than 90% throughout the visible

spectrum. The structures with even lower fill-factors will exhibit improved transparency, however, the density of the topography might not be sufficient to achieve a stable Cassie state [70]. By a careful design of micro- and nanostructures, optimal hierarchical structures that satisfy both superior transparency and superhydrophobicity could be realized.

### **3.4.5 Improved Hydrophobicity of Silane-Treated Metallic TAME Structures**

Metallic TAME structures have potential in the related applications apart from their utility as nanofabrication master molds. Typically, an electrodeposited metal surface (i.e. copper) is hydrophilic (SCA = 55 °); however, the surface of the TAME metallic structures become hydrophobic after TFOCS vapor treatment. The layout design for the template is different from that of the replicated PDMS structures (Figure 3.13); this is to minimize the solid-water contact area when the fabricated TAME structure undergoes wetting. Unlike the replicated structures, the TAME structures do not have nanostructures formed on top of the protrusions. Instead, the nanostructures are formed along the sidewalls and bottom of the trenches.

Figure 3.19 shows SCA and CAH measured from the single-scale structures (the multilayer structures before being copper selectively etched), and corresponding hierarchical structures ( $w_{\text{Nano}} = 350 \text{ nm}$ ,  $g_{\text{Nano}} = 350 \text{ nm}$ ,  $h_{\text{Nano}} = 500, 1500 \text{ nm}$ ;  $w_{\text{Micro}} = 20 \text{ }\mu\text{m}$ ,  $g_{\text{Micro}} = 40 \text{ }\mu\text{m}$ ,  $h_{\text{Micro}} = 18 \text{ }\mu\text{m}$ ) after the TFOCS treatment. The contact angle measurement of the TFOCS-treated, polished silicon substrate is shown as a reference.

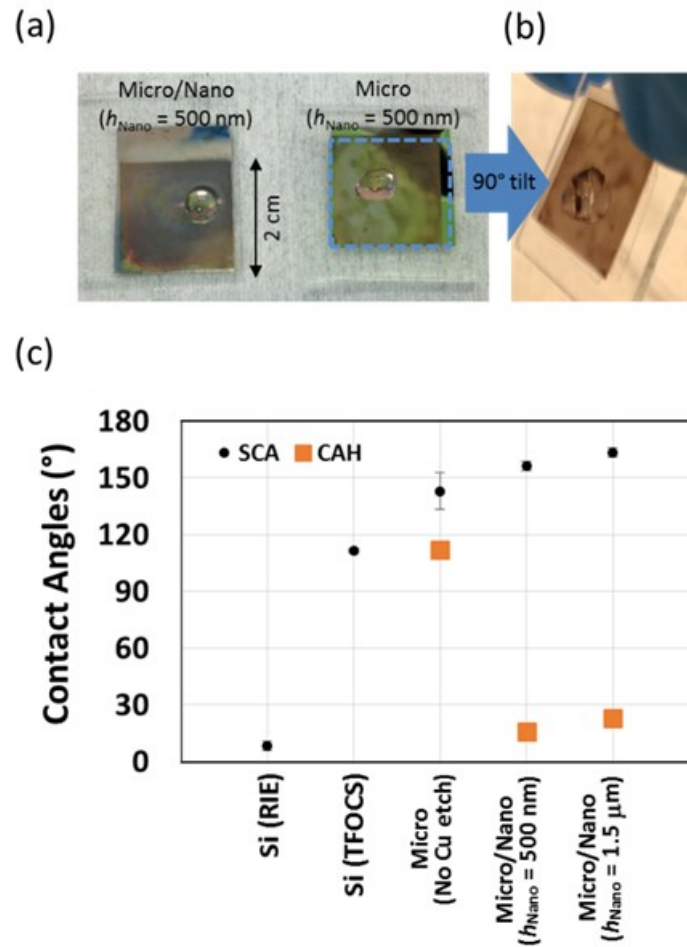


Figure 3.20 Wetting properties of TFOCS-treated metallic TAME structures

The results are very similar to those from the PDMS replica; both high SCA (158 °) and relatively low CAH (18 °) and sliding angle (15 °) are observed only from the hierarchical samples. Figure 3.19 (b) shows a water droplet clung to the single-scale sample held normal to the surface, that corresponds to the high contact angle hysteresis. Note that the multilayers with different nanostructure protrusion heights, 500 nm and ~1.5 μm, show similar SCA and CAH. This means the droplets on both surfaces are in the Cassie state; in other words, the droplets are well supported by the nanostructures, and thereby, the

fractions of the solid under the droplets are nearly identical for both cases. Although not studied extensively, the robustness of these metal structures are expected to be higher than most of the structures based on conventional materials (i.e. silicon, polyurethane, PDMS), yet being mechanically flexible. Also, non-wetting characteristics of the structures could be retained even after applying high mechanical pressure (e.g. shear, abrasion), since the nanostructures are present within the recessed regions of the microstructures. Hence, these structures could be utilized to package a device of which operation is performed within relatively “severe” environments (e.g. high temperature, high mechanical pressure or shear stress), and still requires stable non-wetting surface properties.

### **3.5 Summary**

The TAME process extends achievable structural diversity through a multilayer electrodeposition. A three-dimensional growth of a multilayer leads to various surface nanostructures of which positions, geometries and orientations are controlled by that of the template. The metallic TAME structures can be transferred to conventional materials that are frequently used in micromachining, i.e., silicon and PDMS, via nanoimprint lithography and polymer molding, respectively. The TAME structures with very high structural aspect ratios can be realized through a selective copper removal for an extended period.

Surface hierarchical structures with diverse functionalities (e.g. enhanced Raman signal, microfluidics with reduced drag, batteries with high energy/power densities) could stem from the TAME process. As an example, film-type superhydrophobic surfaces have been demonstrated. The advantage of the TAME-based fabrication compared to alternative

approaches are mainly two-fold: First, hierarchical PDMS structures are fabricated based on a single step replica molding using an optically transparent, elastomeric, and inherently hydrophobic material, h-PDMS. The fabricated structures exhibit superhydrophobicity, while the transparent nature of the material not being compromised. Second, the metallic TAME structures that exhibit non-wetting properties are realized after a vapor silanization. The flexible, robust nature of the structures may lead to a new application area for the non-wetting surfaces (e.g. underwater maneuver). The structural hierarchy of both metallic TAME structures and replicated PDMS structures plays a critical role in achieving non-wetting properties.

# CHAPTER 4

## TAME-BASED VOLUMETRIC HIERARCHICAL STRUCTURES: NANOLAMINATIONS

### 4.1 Backgrounds & Motivation

The TAME-based fabrication approach can be naturally extended for the realization of various volumetric hierarchical structures. In this work, micro-, or nano-scale laminations (i.e. nanolaminations) are developed as an example.

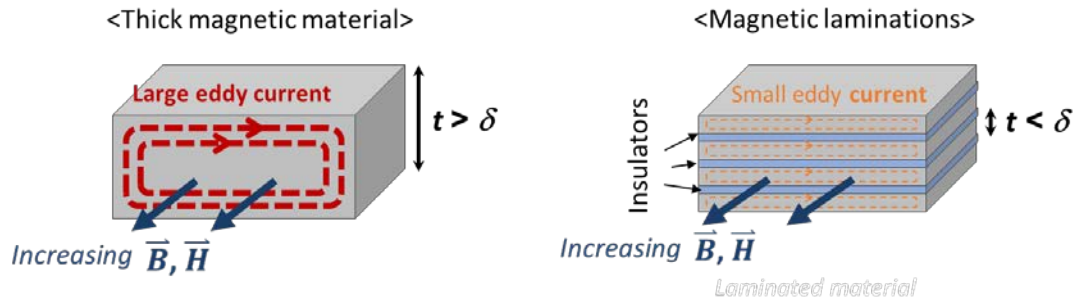
Lamination of electrically conducting, soft magnetic materials is a general way to mitigate eddy current loss within the materials without compromising their power handling capacity. For a magnetic material exposed in a time varying magnetic field, a skin depth [m] is defined as,

$$\delta = \sqrt{\frac{2}{\omega\mu_0\mu_r\sigma}} \quad (4.1)$$

where  $\omega$  is angular frequency [rad/sec],  $\mu_0$  is permeability of vacuum [H/m],  $\mu_r$  is relative permeability, and  $\sigma$  is electrical conductivity [S/m]. If a magnetic material thicker than the skin depth is exposed in a time varying magnetic field, an eddy current flows within the material that acts to cause a substantial decrease of the magnetic flux within the material. Instead of flowing uniformly, the flux is confined within the “skin” of the material. Further, the eddy current causes, an undesirable ohmic electrical power loss.

Hence, by forming layers of magnetic material with thicknesses less than the skin depth of the material at operating frequency, and laminating the layers with minimized

interlayer conductivity, thick magnetic materials of large total volumes can be achieved while the eddy current losses being completely suppressed within the thin, individual layers (Figure 4.1).



#### 4.1 Magnetic materials exposed to a time varying magnetic field.

Traditionally, silicon steel sheets have been employed as the magnetic core materials, while varnish, paper, or clay compounds have been adopted as the interlayer insulation materials [76, 77]. The alternating layers of the steel sheets and insulations are mechanically pressed and clamped together to achieve laminations (Figure 4.2). Such laminations have been utilized for macroscale electrical machines, such as alternators and transformers.

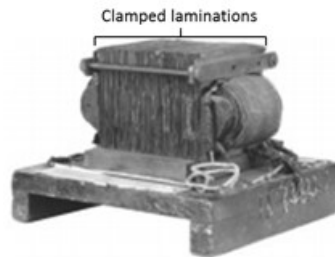


Figure 4.2 Transformer built from Westinghouse, circa 1885. A clamped, laminated core is shared by two inductor coils.



Recently, there has been a considerable effort to miniaturize DC-DC converters as the demand for the multifunctional, hand-held devices (i.e. cell phone) is highly increased. To meet the multi-Watt power handling requirement while the converter size is minimized, typically, the passives (i.e. capacitors and inductors) need to be operated at (1) high frequency (over 1 MHz), while achieving (2) proper level of volumetric energy density within (3) minimized form factors. For an inductive component to meet these requirements, a proper magnetic core material needs to be developed. A conventional solution is to use ferrite materials that exhibit low eddy current losses at such high frequencies (due to their low electrical conductivities); however, they are not the best candidate for converter miniaturization because of their relatively low saturation magnetic flux density. The inductor operation is usually limited to low magnetic flux density ( $< 50$  mT), and thus, the ultimate achievable compactness of the devices is also limited.

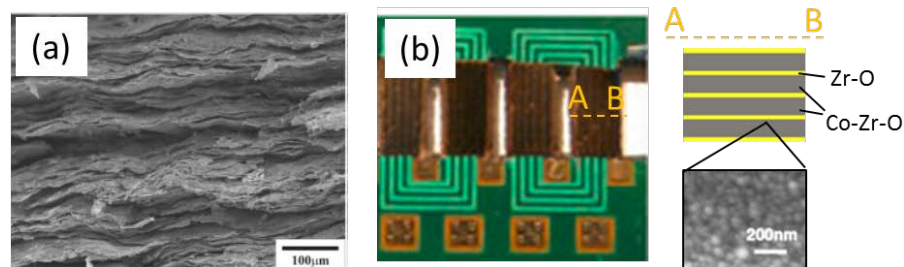


Figure 4.3 Examples of the state-of-the-art lamination processes. (a) Fe/SiO<sub>2</sub> laminations formed by pressing [78]. (b) CoZrO/ZrO sputtered laminations [79]. The picture on the left shows race-track inductors with the laminations. The SEM on the lower right shows the nanogranular morphology of a CoZrO film.

On the contrary, laminations comprised of the thin soft magnetic, metallic alloys can be operated at relatively higher flux (due to their higher saturation flux density), and therefore, higher energy density compared to the ferrites, if the eddy current loss can be suppressed by lamination. However, the realization of the laminations that operate at high frequencies is not trivial since the skin depth of a typical soft magnetic material at a high frequency is only a few micrometers. Also, the interlamination thicknesses should be defined as thin as possible, so that the volume fraction of the magnetic material packed within the laminated structure is maximized.

A bottom-up route of the submicron iron (Fe) laminations with silicon dioxide ( $\text{SiO}_2$ ) insulations has been demonstrated by pressing  $\text{SiO}_2$ -coated, Fe/polymer composites [78] (Figure 4.3(a)). The spherical Fe particles are deformed and planarized during the process, while the electrical insulation between the squeezed Fe particles is supported by the coating materials. After the process, the material can be operated at 50 MHz without significant eddy current loss. Although the fabrication process is relatively simple, the compatibility of this lamination process to conventional micromachining is somewhat questionable (e.g. the induced mechanical pressure during the lamination exceeds 1 GPa); hence, the integration of such core material into small, micromachined components (such as windings) with various geometries may not be straightforward.

Another option is an alternating, sequential deposition of magnetic and insulating materials based on a physical vapor deposition tool (e.g. sputtering); the laminations with controlled nanoscale thicknesses can be achieved, while their overall geometry is defined by conventional micromachining [79] (Figure 4.3(b)). Such laminations exhibit reduced eddy current loss even at high frequencies over 100 MHz, while their fabrication

procedures are CMOS compatible; however, high material built-in stress, as well as relatively slow deposition speed (e.g. a few angstrom per second) may limit the maximum achievable thicknesses of the material, which may restrict the achievable magnetic energy capacity per given footprint.

The TAME-based nanolamination process demonstrated in this chapter achieves batch-scale fabrication of thick (i.e. tens-of-micrometers), soft magnetic metallic laminations based on CMOS compatible processes. The fabrication process starts with a TAME process where the permalloy/copper metallic multilayers are built through predefined photoresist molds. Permalloy is chosen as the magnetic material, since its compatibility to the TAME process is validated and its saturation flux density is relatively high (~1.2 T) (and therefore, proper for high flux operation). At the end of the process, the multilayers are electrically isolated by selective removal of copper, forming air-insulated laminations comprised of thin magnetic layers anchored by polymeric insulating structures. Polymer infiltration techniques are demonstrated in order to fill the air gaps between magnetic layers, thereby reinforcing interlayer insulation as well as improving mechanical robustness of the laminated structures. Such polymer infiltration into air gaps with very high aspect ratio (>1:100) has been performed with polyvinylalcohol (PVA) and PDMS. The resulting laminated structures are comprised of alternating layers of permalloy, and non-magnetic, electrically-insulating insulations, both of which thicknesses are well-defined based on the electrodeposition parameters, while their overall geometries (i.e. toroid, rectangle) are well-defined by conventional lithography.

The following subchapters begin by a detailed description of the TAME-based nanolamination process. Two methods that are critical to validate the lamination process

are developed. Various laminations based on different individual magnetic layer thicknesses and different interlamination insulation materials are fabricated and characterized at high frequencies ( $> 1$  MHz) to verify suppressed eddy currents. A selected sample is operated at high frequency ( $> 1$  MHz)/ high flux density ( $> 0.1$  T), and their losses at such conditions are analyzed to explore their potential in miniaturized DC-DC converters.

## **4.2 Nanolamination Process**

### **4.2.1 TAME Process and Polymer Anchor Fabrication**

The nanolamination approach begins with a TAME process based on a through-mold, one-dimensional multilayer deposition. A multilayer structure comprised of alternating structural permalloy ( $\text{Ni}_{80}\text{Fe}_{20}$ ) and sacrificial copper sublayers is sequentially electrodeposited within a lithographically-defined photoresist mold (Figure. 4.4(a)). Permalloy is chosen as the soft magnetic structural material mainly because of its relatively high saturation flux density ( $B_s = 1.2$  T) and low coercivity (1~5 Oe). The deposition of permalloy is achieved only at a specific current density, i.e.,  $10 \text{ mA/cm}^2$ ; the composition of the deposit is affected by the current density, e.g., higher current density results in the deposit with higher nickel content [80]. The deposition rate of the permalloy is  $8 \text{ }\mu\text{m/hour}$  at  $10 \text{ mA/cm}^2$ .

A series of post-TAME processes follows. The polymeric anchors are fabricated within the multilayer structures. The main role of the anchors is to provide mechanical support for the free-standing laminations that are created after the subsequent sacrificial copper removal process. The anchors need to be good electrical insulators so as to not add

any conductive route for eddy currents between individual magnetic layers. Figure 4.4(b)-(e) depicts anchoring procedures employing two different kinds of insulating polymers: SU-8 (Microchem) and PDMS (Dow Corning).

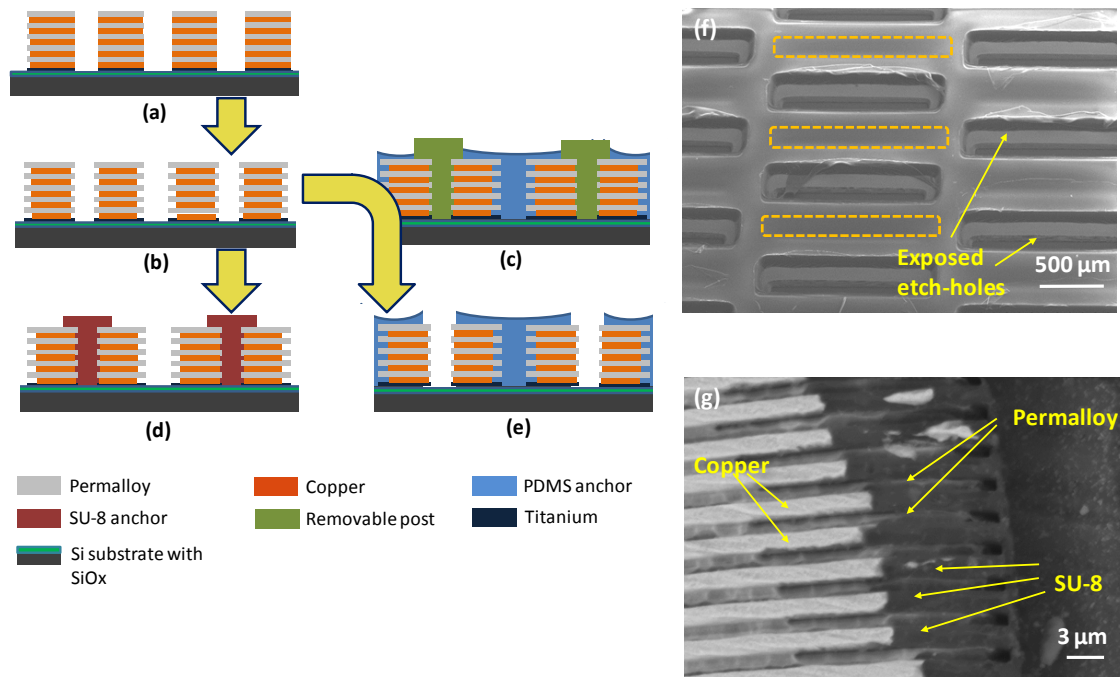


Figure 4.4 Polymer anchoring process. The sequence (a),(b),(d) depicts fabrication of SU-8 anchors, whereas (a), (b), (c), (e) represents PDMS anchoring process: (a) Electrodeposited multilayer structures, (b) partial etch of the multilayer structures to form microscale lateral trenches, (c) spin-cast of PDMS on photoresist post structures, (d) SU-8 anchor formation, and (e) removal of the photoresist post structures. Fig. 2.8(f) and (g) are SEM images of polymeric anchors. (f) Top view of PDMS anchors fabricated by spin-cast micromolding. The locations of anchors are highlighted by dotted rectangles. (g) Cross-sectional view of an SU-8 anchor coupled to a multilayer structure of 1.5 μm-thick permalloy and 1.5 μm-thick copper.

Beginning with the fabricated multilayer structures, the process involves a short selective etching of copper to create approximately 5 to 10 μm-deep microscale lateral trenches on the sidewall of the multilayer structures (Figure 4.4(b)). The copper selective

etchant used in the lamination process is a concentrated ammonium hydroxide solution, saturated with copper sulfate (etch rate: 0.5~1  $\mu\text{m}/\text{min}$ ). Then, a subset of the etch holes are filled with polymer and the polymer is crosslinked. The definition of the subset of etch holes is done in a material-specific manner. For SU-8, either a blanket manual dispense which fills all of the etch holes is performed, or spin-casting followed by photolithography is performed to selectively open some etch holes (Figure 4.4(d)).

Patterning of PDMS anchors is performed based on spin-cast micromolding [81]. In this process, photoresist post structures thicker than the multilayer structures are formed in some of the etch holes using traditional photolithography. Then, PDMS is dispensed, and de-gassed to fill the non-resist-containing holes as well as to cover the post structures. The sample is spun at a high speed (4000 rpm) to leave only a thin layer of PDMS on top of the protruding resist posts (Figure 4.4(c)). Removal of the photoresist posts effectively 'lifts-off' these thin PDMS residues, while leaving PDMS in the non-resist-containing etch holes, thereby anchoring the free-standing laminations. The sidewalls of the etch holes that originally contained photoresist are now exposed after an acetone rinse and available to facilitate sacrificial copper removal (Figure 4.4(e)). Figure 4.4(f) shows patterned PDMS anchors present in alternating etch holes of the multilayer structures. Figure 4.4(g) is a cross-section view of a polymeric anchor (SU-8), demonstrating that the SU-8 is interlocked with the multilayer structure.

## 4.2.2 Selective Copper Removal and Sample Drying

After the polymer anchors are fabricated, a selective, complete removal of sacrificial copper layers from the permalloy/copper multilayer structures is performed (Figure 4.5). As the multilayers are immersed into a selective copper etchant, the copper is etched beginning from the sidewalls of the multilayers that do not possess the polymeric anchors as well as from the periphery of the multilayer structures. It is very important to validate the complete removal of copper after this process; however, direct imaging of the etched multilayers alone cannot verify the removal. The estimation of the etching time is also difficult, because the copper etch rate may decrease as the etching progresses, and also because the rate may not be spatially uniform. From Figure 4.5, it is observed that the copper layers deposited within the final deposition sequences are etched almost twice as faster than the layers deposited at the earliest sequences; this suggests the concentration of the by-products resulting from the etching might be increased in the vicinity of the substrate, and thereby, the etching is locally inhibited.

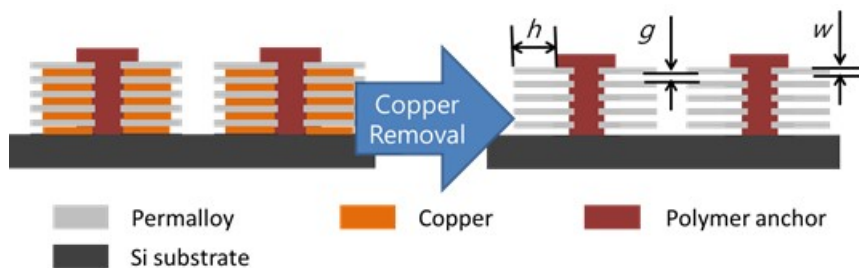


Figure 4.5 Selective copper removal.

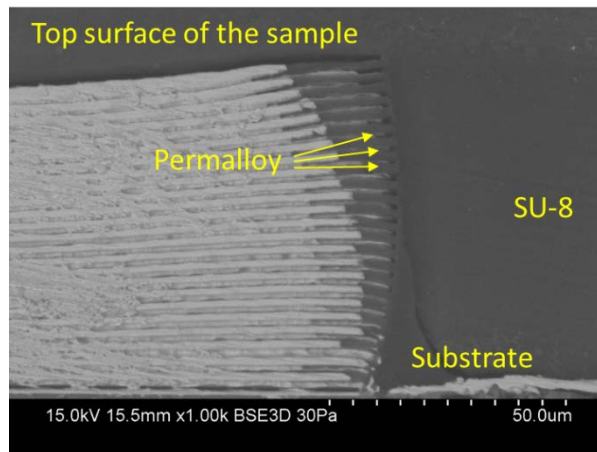


Figure 4.6 Cross-section view of a multilayer sidewall after SU-8 anchoring. This is a low magnification view of the Figure 4.4(g).

Two approaches have been developed to verify the complete copper removal: One relies on the weight loss measurement of the multilayers throughout the etching; the other relies on the electrical measurement of the coil-wound multilayers, periodically performed throughout the etching. The weight loss measurement begins by preparing the freestanding, SU-8 supported multilayers; the samples are detached from the substrate by removing the underlying silicon dioxide layer with a hydrofluoric etch. Various types of samples with different geometries (e.g. toroidal multilayers of different inner/outer diameters and etch hole geometries/densities, rectangular multilayers) are used in the experiments; however, the volume ratio of the copper and permalloy within the samples are set the same (i.e. 1:1).



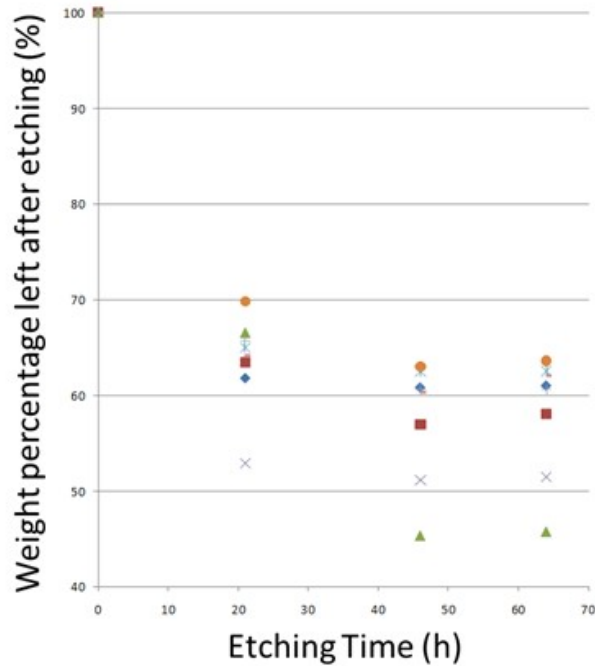


Figure 4.7 *In-situ* weight measurement result for 9 samples with different designs. The y-axis represents the remaining weight percentage of the samples after a certain period of copper etching. Typically, the weight of each sample is several tens-of-milligrams.

The weight ratios between the two materials are also very similar due to their similar densities (i.e.  $8.96 \text{ g/cm}^3$  for bulk Cu,  $8.70 \text{ g/cm}^3$  for bulk permalloy). After the weight of each sample is measured prior to the etching, the samples are immersed in the blue etchant. The samples are periodically removed from the etchant, rinsed with DI water, isopropyl alcohol (IPA), and dried in an oven. The weight measurements are followed immediately after the drying, and the samples are again immersed in the etchants. This is repeated at least until the sample weights are not changing with respect to the etching time. The Figure 4.7 shows the measured sample weights throughout the etching. It is observed that the measured weights of the samples do not change after  $\sim 40$  hours of etching. Considering

that the volume ratio of permalloy and copper may slightly differ from 1:1, and that the volumetric portion of the SU-8 anchors may differ from sample to sample, the measured sample weights after the copper removal (i.e. 45%~65%) are as expected. The etching time required for the complete copper removal can be estimated for the samples with various geometries.

The copper removal can be also estimated by an *in-situ* electrical measurement of the multilayers throughout the etching process. For this measurement, a multilayer sample detached from the substrate is packaged into a laser-micromachined polymer bobbin, as shown in Figure 4.8. As a result, an inductor is formed. The height of the bobbin is designed to exceed that of the packaged sample, so that a wire (i.e. Litz wire) can be wound around the sample without making any contact to the sample. The notches patterned along the periphery of the bobbin (Figure 4.8) are designed so that the wire can be manually wound with uniform density.

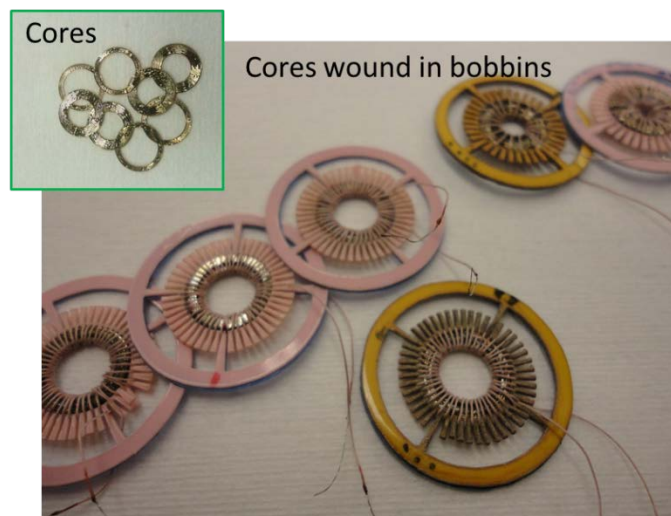


Figure 4.8 Multilayers packaged into polymeric bobbins, forming inductors. Litz wire wound around each magnetic core can be observed.

The inductor is immersed in the ammonia-based, copper selective etchant. While the copper within the sample is being etched, the bobbins, as well as the wire, remain intact. The sample is periodically removed from the etchant, thoroughly rinsed in DI water, and the inductance of the inductor is measured as a function of frequency. The measurement is performed while the sample is still immersed in the DI water bath; this is to prevent the water from drying, and thereby, minimizing the probability of stiction between the released laminations. Before the etching, the inductance of the inductor decreases as the frequency increases, due to the presence of substantial interlamination eddy currents. As the copper is etched, eddy currents within the multilayer sample are reduced (and high frequency performance is improved). The end point of the release process can be determined as the time after which

the inductance of the inductor either: (1) no longer falls with frequency for frequencies at which the skin depth is greater than the lamination thickness; or (2) no longer changes with etching time for the frequencies at which the skin depth is less than the lamination thickness.

A sample measurement result is shown in Figure 4.9. The copper within the sample is estimated to be completely removed between 20~39 hours after the etching began. It is observed that the etching time can be as short as 3 h or as long as 48 h depending on the shape of the multilayer structures and the distribution of etch holes not occupied by polymeric anchors. Once the etch time for a given multilayer geometry has been established using this technique, this etch time can be taken as a process parameter for complete copper removal.

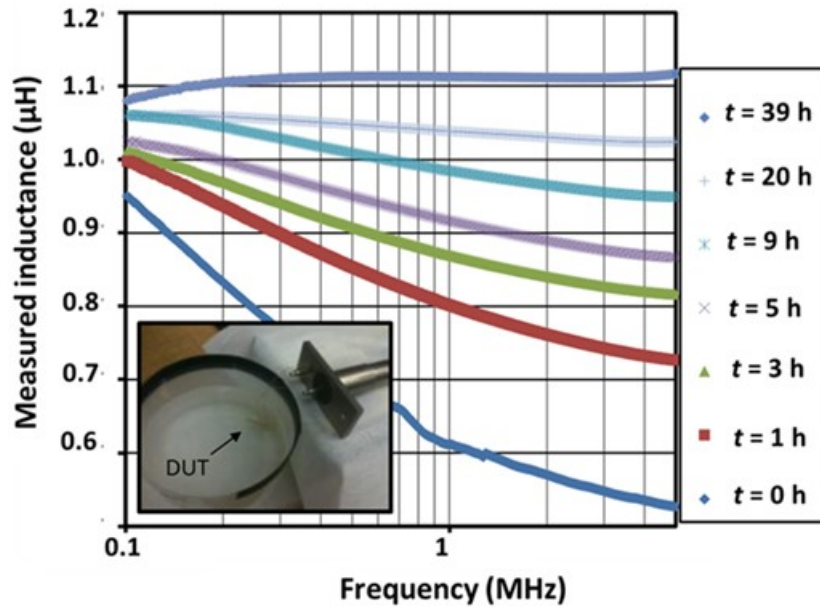


Figure 4.9 *In-situ* electrical measurement result for a multilayer sample. The inset shows the device-under-test (i.e. inductor) immersed in the rinsing DI water, of which two ports are connected to the impedance analyzer (right). The toroidal multilayer sample is comprised of 40 pairs of permalloy ( $1\ \mu\text{m}$ )/copper ( $1\ \mu\text{m}$ ), of which outer, and inner diameter are 8 mm and 6 mm, respectively.

After the complete removal of copper, the samples are rinsed in isopropyl alcohol (IPA) for 5 minutes, and rapidly dried in a convection oven at  $70\ ^\circ\text{C}$  to minimize stiction between the permalloy layers. The resulting structure, comprising individual lamination layers separated by air and held in place by polymeric anchors, is referred to as "air-insulated laminations". Fabricated air-insulated laminations exhibit very high aspect ratio. The aspect ratio of a single lamination (or air gap) is defined by the ratio of the thickness of the layer,  $w$  (or the gap between two individual layers,  $g$ ) to the distance between the periphery of the laminations and the nearest polymeric anchor ( $h$ ), as depicted in Figure

4.4. Aspect ratios of both permalloy layers and air gaps could be as high as 1:400 ( $w, g = 1.5 \mu\text{m}, h = 600 \mu\text{m}$ ). The minimum air gap achieved in this experiment is 500 nm with an aspect ratio of 1:300.

### 4.2.3 Polymer Infiltration Processes

From a structural perspective, air-insulated laminations differ from conventional core laminations, as the interlamination space of conventional laminations is typically filled by an insulating solid. The aspect ratio of the air-insulated laminations easily exceeds 1:100; hence, individual laminations are mechanically fragile. It may therefore be desirable to develop solid interlamination insulators, thereby, providing mechanical reinforcement of the laminations. It is important that the packaging processes should be performed (1) at low temperature so as to not oxidize the metallic laminations, (2) without depending on the expensive, high vacuum approach, such as atomic layer deposition.

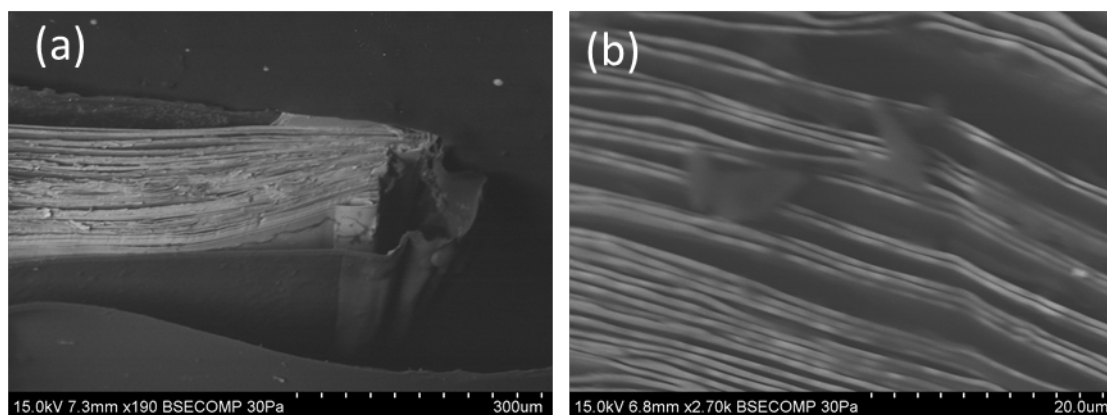


Figure 4.10 Parylene-deposited, air-insulated laminations. (a) The cross-sectioned view. A dark grey layer of parylene visible around the multilayer sample. (b) The magnified view. The infiltrated parylene is found only within a few sites. The gap between the individual laminations is designed to be a single micrometer.

As an initial attempt, parylene deposition is performed on the air-insulated laminations since the deposition is known to be conformal; however, the parylene seems to deposit only around the “skin” of the laminations, not within the trenches, as observed from the cross-sectioned images (Figure 4.10). Alternatively, two methods, i.e., PVA infiltration technique and PDMS infiltration technique, are developed.

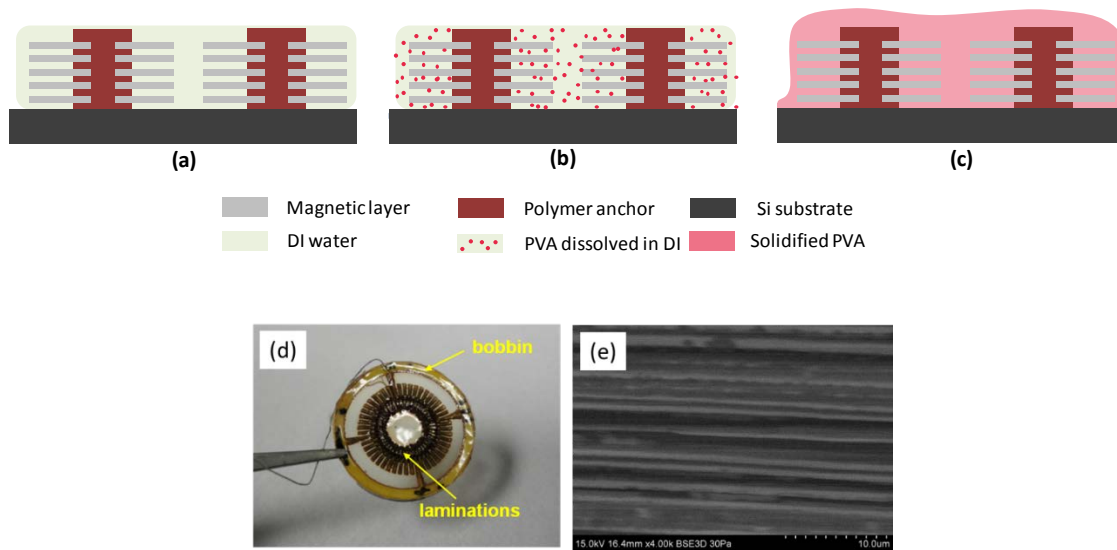


Figure 4.11 PVA-infiltrated laminations. (a) DI rinse of the multilayer structures, (b) addition of PVA into the rinse solution, and (c) drying or heating the sample to solidify PVA. (d) A picture of the PVA-infiltrated laminations packaged in a bobbin. (e) A cross-sectional image of the permalloy (light grey)/PVA (dark grey) laminations.

The PVA infiltration technique gradually substitutes the multilayer rinse solution by a solution containing the water-soluble polymer, PVA. Note that the sample is not dried prior to infiltration, which is beneficial in terms of preventing stiction between the sublayers. The Figure 4.11 illustrates the PVA infiltration process. Immediately after sacrificial copper etching is completed, the etched multilayer structure is removed from the etching bath, rinsed, and immersed in a deionized (DI) water bath without any intermediate

drying to remove copper etchant from the structure. A solution of PVA in DI water (1:5 by weight) is gradually added to the bath, approximately doubling the bath volume and allowing the dissolved polymer to diffuse into the gaps between the permalloy layers (Figure 4.11(b)). Finally, the sample is dried (or heated at 95 °C) until the PVA is solidified (Figure 4.10(c)). The Figure 4.11(d) shows the sample after the packaging.

The vacuum infiltration of PDMS is an established technique for filling porous structures with interconnected microscale pores [82]. The superior performance of PDMS in this application stems from not only its air-permeability but also its ability to be cast in a solventless fashion. To infiltrate the high aspect ratios of the air-filled laminations, PDMS is degassed under vacuum and dispensed onto the air-insulated laminations (Figure 4.12 (a),(b)). The PDMS used in this experiment is conventional Sylgard 184, i.e., soft PDMS. The PDMS/lamination composite is then placed in a vacuum chamber for 30 min at room temperature to ensure full PDMS infiltration (Figure 4.12(c)). The thickness of PDMS on top of the sample can then be adjusted by a subsequent spin-coating step. The sample is held for 48 hours at room temperature, or 4 hours in an oven at 70 °C, to fully cross-link the PDMS.

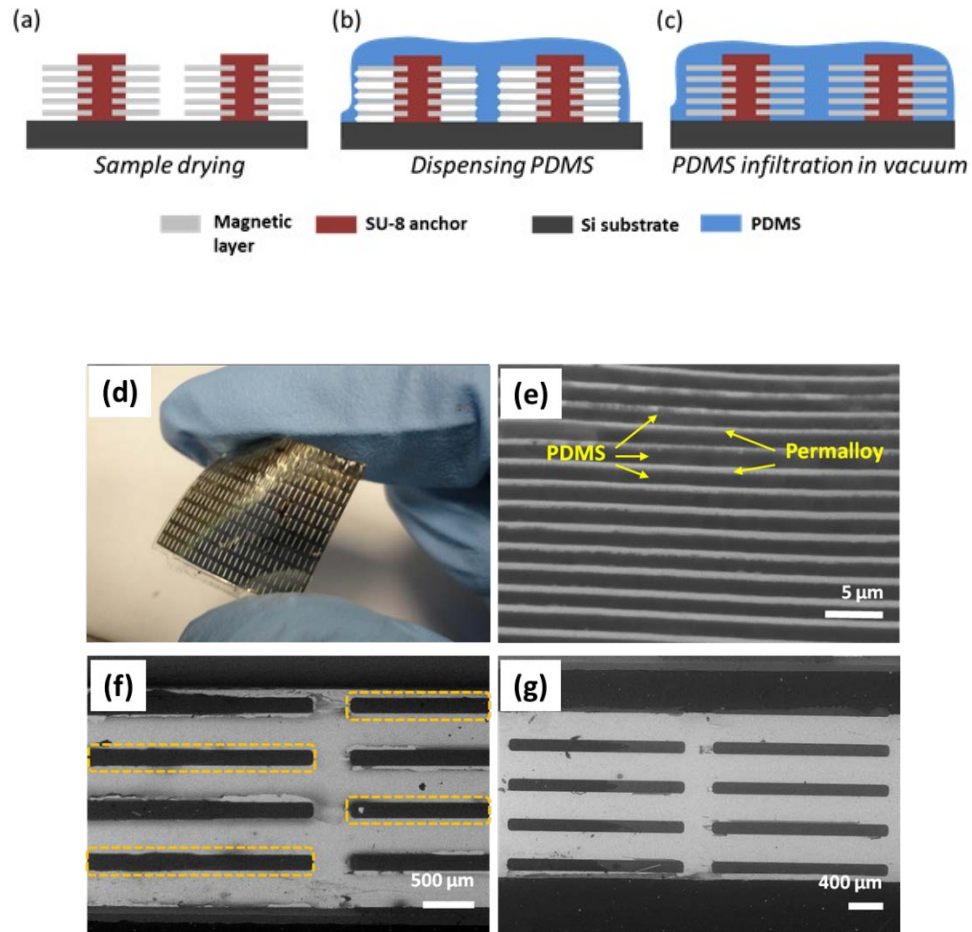


Figure 4.12 PDMS-infiltrated laminations. (a) Air-insulated laminations. (b) PDMS poured over the laminations. Note that the viscous PDMS is not fully infiltrated into the trenches. (c) Vacuum infiltration of PDMS. (d) An optical image of a freestanding PDMS-infiltrated permalloy laminations (lamination thickness and interlamination spacing of  $1.5\ \mu\text{m}$ ) (e) Cross-sectional image of the sample shown in (d). The PDMS-infiltrated structure is further dissected to show (f) a top view of the surface of a single layer of infiltrated PDMS and (g) the surface of the permalloy layer which was originally in contact with the PDMS layer shown in (f).

The PVA- and PDMS-infiltrated laminations are cross-sectioned to image the polymers filled in the laminations, respectively (Figure 4.11(e), and Figure 4.12(e)). In both cases, polymer layers (dark) can be observed between the permalloy layers (light



grey). In order to obtain better evidence of complete polymer infiltration, a portion of the multilayer structure was peeled back along a PDMS-permalloy interface to reveal a top view of the infiltration. The surface of an infiltrated PDMS layer is thereby exposed as shown in Figure 4.12(f); Figure 4.12(g) shows the surface of the permalloy layer which was originally in contact with the PDMS layer shown in Figure 4.12(f). The PDMS was infiltrated from the sites indicated by dotted lines (Figure 4.12(f)), and the interlamination region was completely filled up to the PDMS anchor regions. The perfect infiltration of the soft PDMS into such high aspect ratio trenches is unexpected from the results presented in Chapter 3.1. However, it should be noted that, unlike the surface relief structures shown in the previous chapter, all the trenches within an air-insulated laminations are “interconnected” to each other; initially trapped air between the dispensed PDMS and the sample has more chances to be de-gassed by the vacuum.

These two packaging approaches have pros and cons. The PVA infiltration technique could be utilized to achieve insulations between the laminations spaced by very thin gaps. However, the solvent may remain within the gaps of the laminated structure after the sample drying process, since the solvent near the entrances of the lateral trenches is likely to dry rapidly; the remaining solvent within the structure may result in the oxidation of the laminations. For this reason, other solvent/dissolved polymer pairs that are compatible with permalloy, such as SU-8 and propylene glycol methyl ether acetate (PGMEA), could be utilized as an extension of this approach. Using the PDMS infiltration technique, the trenches formed between the individual layers can be filled with the solid PDMS nearly perfectly. In addition, the elastomeric nature of the composite material might lead to new applications, such as magnetic sensors, or compliant electrodes. However, this

approach might not be useful in packaging the laminations with very narrow trenches (~100 nm) because of the relatively high viscosity of PDMS (850~1150 cSt, at room temperature).

### **4.3 Application: Magnetic Materials for High Frequency High Flux Operation**

In order to assess the utility of the fabricated laminations at high frequency (1-10 MHz)/high flux (> 0.1 T) operation, the laminations are packaged to form inductors, and a series of electrical characterizations are performed.

First, the laminated inductors with different interlamination insulation materials and individual lamination thicknesses are prepared, and their inductances are measured as a function of operation frequency at a relatively low flux density (2 mT). By comparing the results to the theoretical inductances calculated based on perfect interlayer insulation assumption, the quality of the various insulations are assessed, and thereby, the lamination processes are validated.

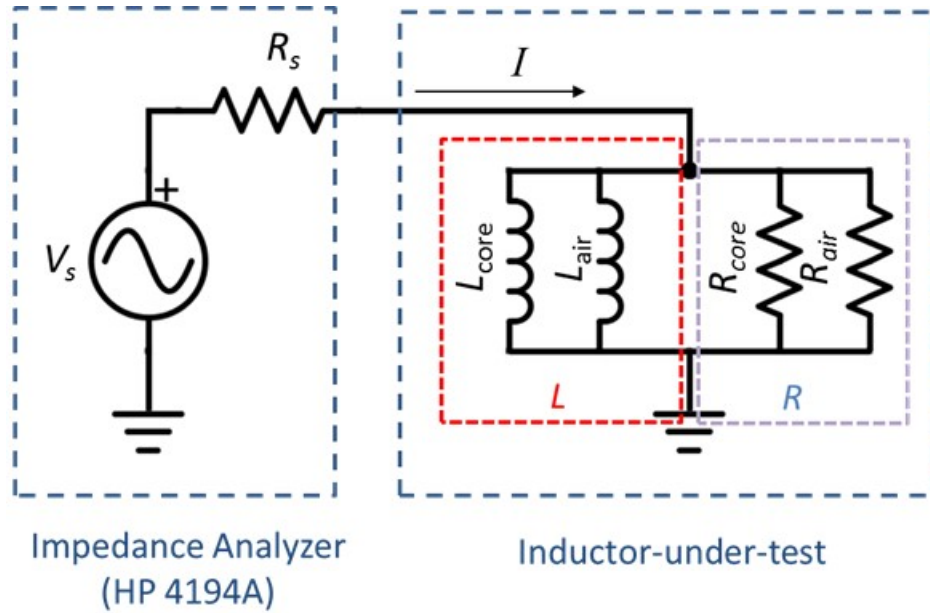
Second, the actual power losses resulting from the hysteresis and eddy current are calculated as a function of frequency and operating flux density; the comparison between the two losses enables the lamination insulation assessment. The analysis is performed with the measurement results at high flux densities over 0.1 T where most ferrites cannot be operated. This demonstrates the potential of miniaturized inductors of which sizes are much smaller than the ferrite-core devices, yet achieving similar level of power handling.

### 4.3.1 Electrical Characterization of the Inductors With Various Interlamination Insulations

The inductor characterization is performed using an impedance analyzer as depicted in Figure 4.13. Small, sinusoidal AC excitation voltages ( $V_s$ ) are supplied within the tool, and the impedance of an inductor is calculated based on the measured electrical current through the device ( $I$ ); the measurement is repeated for a series of voltage excitation with different amplitudes. The results (i.e. frequency-dependent inductances measured at various input voltages) are re-arranged so that the inductance as a function of frequency is parameterized by the inductor current, or the magnetic flux density within the laminated core using equation 4.2:

$$LI = NBA \quad (4.2)$$

where,  $L$  is the measured inductance [H],  $I$  is the measured inductor current [A],  $N$  is the number of turns,  $B$  is the calculated magnetic flux density [T], and  $A$  is the total cross-sectional area of the magnetic material [m<sup>2</sup>]. The inductances measured from the inductors of different geometries presented in this subchapter 4.3.1 are presented at a peak flux density of 2 mT. The core losses are not only a function of frequency, but also of flux density (detailed discussion in the subsequent chapters), and thus, the geometrical differences between the samples must be considered for a fair comparison.



4.13 Inductor under impedance measurement.

From the measured inductance of the inductor ( $L$ ), the inductance of an air-core inductor (i.e. a wire-wound bobbin with the identical winding geometry, yet without the laminations) is subtracted to estimate the contribution of the laminated material to the total inductance. This is referred to as a "core inductance ( $L_{eff}$ ).". The "core resistance." which represents the resistance resulting from the core loss, is similarly derived using the measured inductor resistance ( $R$ ). The circuit diagram in Figure 4.13 shows the result of such decomposition.

$$L_{core} = L - L_{air} \quad (4.3)$$

$$R_{core} = R - R_{air} \quad (4.4)$$

The core inductance is further normalized by dividing it by the value of the core inductance at the lowest frequency of interest, to calculate “normalized core inductance,”  $L_{n,meas}$ . The normalized core inductance of any laminated material is unity at the lowest frequency of interest (~100 kHz) and decreases as frequency increases, regardless of the total magnetic volume of the material and/or number of winding turns around the material.

The quality of a laminated structure (including the thickness uniformity of individual laminations and the interlamination insulation conductivity) is evaluated by comparing  $L_{n,meas}$ , and its theoretical value ( $L_{n,theo}$ ) which is calculated from a one-dimensional analysis of the electromagnetic diffusion in a packet of laminations with perfect interlamination insulation for sinusoidal excitation as below [83]:

$$L_{n,theo} = \frac{L}{L_0} = \left(\frac{\delta}{2b}\right) \left\{ \frac{\sinh\left(\frac{2b}{\delta}\right) + \sin\left(\frac{2b}{\delta}\right)}{\cosh\left(\frac{2b}{\delta}\right) + \cos\left(\frac{2b}{\delta}\right)} \right\} \quad (4.5)$$

where  $L$  is the effective inductance of the material [H],  $L_0$  is the low frequency effective inductance of the inductor [H],  $2b$  is the thickness of a single magnetic layer [m], and  $\delta$  is the skin depth [m] of the magnetic material at the operating frequency. Since the above equation was derived assuming perfect interlamination insulation, if the values of ( $L_{n,meas}$ ) are similar to those predicted by the above equations ( $L_{n,theo}$ ), confidence can be gained that the interlayer lamination insulation is performing appropriately.

Figure 4.14 shows both  $L_{n,meas}$  and  $L_{n,theo}$  at 5 MHz for the laminated structures with different interlamination insulation materials, with different individual magnetic layer thicknesses. A  $\mu_r$  of 1000 and a  $\sigma$  of  $1.43 \times 10^7$  [S/m] is used for the calculation [84], which are typical values of electrodeposited permalloy. It is observed that the discrepancy

between  $L_{n,theo}$  and  $L_{n,meas}$  for all the laminated structures presented is within approximately 6%; the discrepancy may be attributed to the combination of minor fabrication error (i.e. laminations fabricated slightly thicker or thinner than expected) and estimation of the material properties of permalloy (i.e. relative permeability and resistivity).

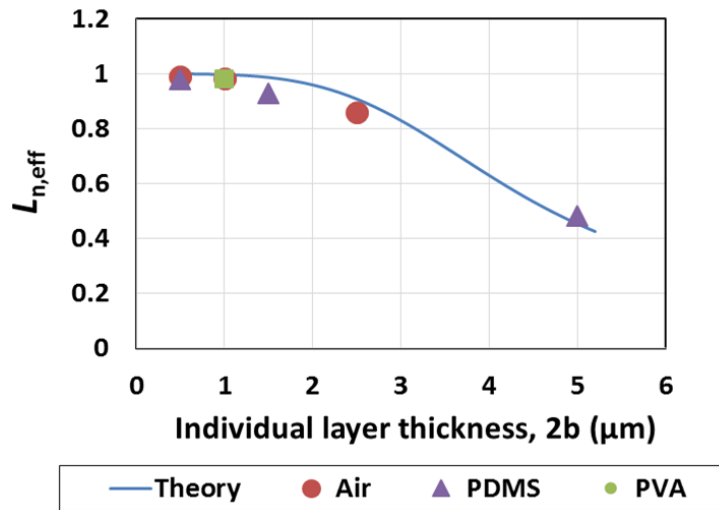


Figure 4.14 The measured normalized core inductance of fabricated laminated structures ( $L_{n,meas}$ ) and its theoretical calculation ( $L_{n,theo}$ ) for various lamination thicknesses, at 5 MHz. Interlamination thicknesses are identical to the layer thicknesses.

This indicates that the decrease of the normalized core inductance mostly depends on the thickness of individual laminations; in other words, the eddy current loss from the laminated structures results solely from the skin depth effect within the individual permalloy laminations, and not from interlamination conduction, for all three interlamination insulation materials (air, PVA, and PDMS). These results imply that the frequency-dependent behavior of these laminated structures are consistent with excellent interlamination insulation performance.

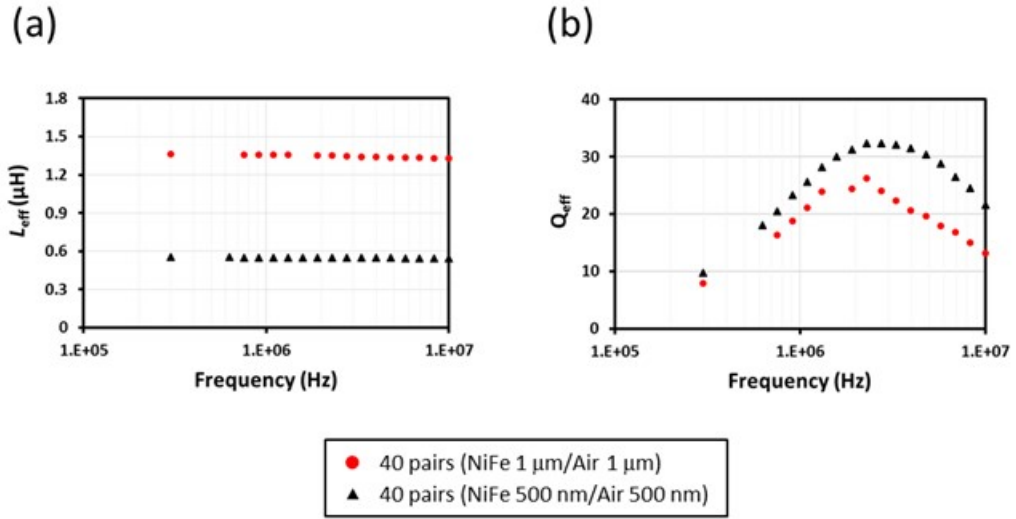


Figure 4.15 Characterization of two inductors (36 turns) at 2 mT. Both having toroidal air-laminated cores of outer diameter, 8 mm, and inner diameter 6 mm).

It is important to note that the eddy current loss of fabricated laminations with single, or submicron individual layer thicknesses is almost completely suppressed up to 10 MHz, while the total thickness (or volume) of the magnetic material is large enough to achieve sufficient inductance ( $> 500$  nH) to handle multi-Watt power (with reasonable winding density). Figure 4.15 shows such inductors as an example. The inductance of the inductor comprising single micrometer laminations is almost twice as large as that from the inductor comprising half micrometer laminations, since the number of the laminations is almost exactly doubled.

The core  $Q$  factors (i.e.  $Q_{core}$ ,  $Q$  factors representing the contribution of the magnetic cores) are calculated as:

$$Q_{core} = \frac{\omega L_{core}}{R_{core}} \quad (4.5)$$

For both inductors, the Q factors reach beyond 20 within 2~3 MHz (Figure 4.13(b)). This shows that the inductors with core laminations are effective in storing magnetic energy at such high frequencies, validating the TAME-based nanolamination process.

#### 4.3.2 High Frequency High Flux (HFHF) Inductor Characterization and Loss Analysis

It is important to verify that the presented nanolaminated soft-magnetic metal alloy cores can be operated at higher flux density than typical ferrites, while the eddy currents are still suppressed at high frequencies ( $> 1\text{MHz}$ ). To test the inductors at high flux ( $> 0.1\text{ T}$ )/ high frequency ( $> 1\text{ MHz}$ ), a special setup is prepared. Detailed description about the setup and its operation can be found in [32]. A sinusoidal input voltage from the function generator (Agilent 33120A) is amplified by an RF amplifier (BT00500-AlphaS, TOMCO), and then induced to the board having an inductor (i.e. device-under-test) and a capacitor connected in series (Figure 4.16). The input voltage into the board ( $V_{in}$ ), as well as the voltage across the inductor (i.e. output voltage,  $V_{out}$ ), are measured. The measured voltages are peak values.

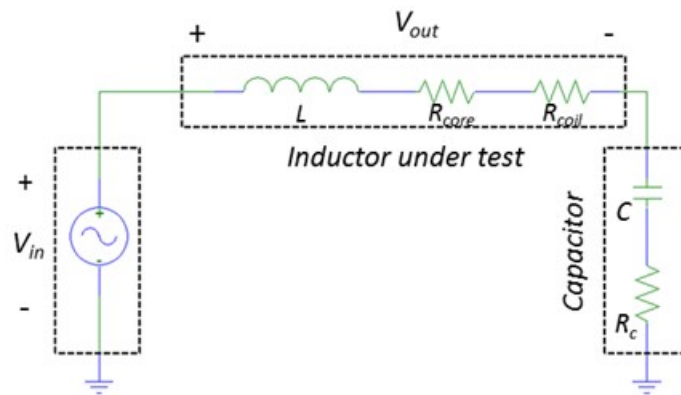


Figure 4.16 Schematic of the high flux measurement setup.



When the LC circuit acts as a purely resistive load, the circuit is operated at its resonance frequency ( $f_c = \frac{1}{2\pi\sqrt{LC}}$ ), which allows the calculation of its power dissipation as the product of the root-mean-square values of the LC circuit's current and measured voltage waveforms ( $V_{in}$ ,  $V_{out}$ ). The  $Q$  factor of the inductor ( $Q_L$ ) can be immediately calculated as the ratio between the  $V_{in}$  and  $V_{out}$  [85]:

$$\frac{V_{out}}{V_{in}} = \left| \frac{R_c + \frac{1}{j2\pi f_c C}}{R_{coil} + R_{core} + R_c} \right| = Q_L$$

Then, the  $R_{core}$  is calculated as a function of  $Q_L$  ( $R_c$  neglected):

$$R_{core} = \frac{2\pi f_c L}{Q_L} - R_{coil}$$

The inductor current is calculated using  $V_{out}$ :

$$I = 2\pi f_c C V_{out}$$

Hence, the power losses of the core is calculated to be:

$$P_{core} = \frac{I^2 R_{core}}{2} \quad (4.6)$$

Dividing the  $P_{core}$  by the total volume of the nanolaminated core results in the volumetric core loss,  $P_{v,core}$ . The sinusoidal peak flux density of the core is calculated from the voltage measured across a multi-turn ( $N_{pickup}$ ) secondary pick-up coil partially wound around the inductor, based on Faraday's law of induction,

$$B_{core} = \frac{V_{pickup}}{2\pi N_{pickup} f_c A}$$

where  $A$  is the total cross-sectional area of the magnetic materials. The flux within the core can be varied by modulating the input voltage.

After the core losses are extracted as a function of the flux at a single frequency, the capacitance of the capacitor is changed. The measurement is repeated at a new frequency where the LC circuit resonates. The volumetric power losses attributed to the core are calculated as a function of frequency and induced flux,  $P_{v,core}(f, B_{core})$ .

According to the classical electromagnetic theory [83], the volumetric loss from a magnetic material can be largely broken in to the hysteresis of the magnetic material and eddy current loss, of which are in proportion to the first, and the second power of operating frequency ( $f$ ), respectively:

$$P_{v,tot} = P_{v,hyst} + P_{v,eddy} = k_1 B^2 f + k_2 B^2 f^2 \quad (4.7)$$

or,

$$\frac{P_{v,tot}}{f} = \frac{P_{v,hyst} + P_{v,eddy}}{f} = k_h + k_e f \quad (4.8)$$

Hence, the volumetric power loss of the material, divided by the frequency, is linear to the operating frequency, and its slope ( $k_e$ ) and intercept ( $k_h$ ) can be mathematically defined.

Figure 4.17 shows how the measured volumetric core loss is decomposed into hysteresis and eddy current loss, by plotting  $P_{v,core}/f$  as a function of frequency and flux. The device-under-test was a 36-turn bobbin inductor with air-insulated laminations (i.e. 40 pairs of 500 nm-thick permalloy/500 nm-thick air). From Figure 4.17(a), the terms  $k_h$  and  $k_e$  are extracted, and multiplied by the  $f$  and  $f^2$ , to calculate the volumetric power loss

attributed to the hysteresis and eddy current, respectively; these are plotted with respect to the induced magnetic flux (Figure 4.17(b)). The extracted linear fitting lines from measured data of each peak flux density shows nearly zero-degree slopes (Figure 4.17(a)), and as a result the estimated eddy current loss is almost negligible compared to the hysteresis loss (Figure 4.17(b)). The portion of the eddy current loss to the total loss is around 1~3 %. Also, the measured hysteresis loss corresponds to the  $B^2$  fit, which corresponds to Equation (4.7), i.e., classical loss theory [83].

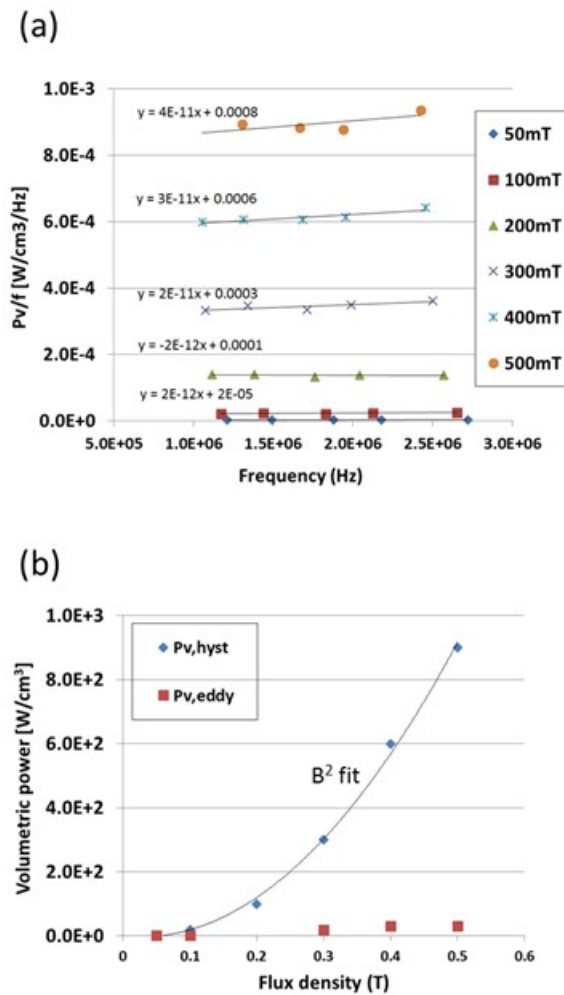


Figure 4.17 Measured volumetric core loss of a sample. (a) Total core loss with respect to frequency and induced flux density. The graphs are linearly fit to extract  $k_h$  and  $k_e$ . (b) Volumetric loss broke down to the hysteresis and eddy current loss.

These results show that (1) the laminated core can be operated up to 0.5 T (that is not achievable using commercially available ferrites with lower saturation flux density) within 1~5 MHz (2) without suffering from eddy current loss. The total volumetric loss of a laminated core ( $\sim 8.5 \text{ W/cm}^3$  @ 1MHz) is still larger than that of a typical ferrite core (e.g.  $0.5\sim 0.9 \text{ W/cm}^3$  @ 1MHz [86]) at a specific flux density of 0.05 T, due to larger hysteresis loss; however, in order to achieve ultimate compactness of a system (i.e. an inductor, or a converter using such inductor), an inductor should be operated at much higher flux density (0.1~0.5 T) where the typical ferrite cores may saturate and soft magnetic metal alloy cores are regarded as a better candidate. The hysteresis loss of nanolaminations could be further reduced by (1) using a magnetic material with smaller coercivity (e.g. CoNiFe) [87], or (2) optimizing the magnetic anisotropy based on an in-field magnetic layer electrodeposition [88].

Considering the total core volume ( $1.5 \text{ mm}^3$  including the air gaps), the total loss from the core exceeds 1 W when it is operated within 0.3~0.4 T. It is observed that the temperature of the sample is high enough to deform the plastic at such high flux operation; hence, the sample is cooled by pressurized air when the test exceeds 0.2 T. The temperature increase is not significant under 0.2 T (stable near room temperature) at which continuous operation has been feasible without any cooling. From the structural point of view, the air-insulated laminations are more desirable than the bulk ferrite cores since the individual laminations are (1) metallic, and (2) the surface-to-volume ratio of the overall laminated structure is very high. Although not attempted, the cooling performance comparison between a ferrite and a laminated core operating at a similar level of power dissipation could be interesting.

#### 4.4 Summary

The nanolaminations with various interlamination insulation materials (e.g. air, PVA, PDMS) were developed as an example of TAME-based volumetric hierarchical structures. While the overall geometry of a laminated structure (i.e. toroidal/rectangular shape with evenly distributed SU-8 anchors) was defined based on conventional lithography, the nanoscale thicknesses of individual laminations are controlled by the multilayer electrodeposition. The microstructures not only define the flux path, but also help improve the mechanical integrity of the nanostructures (i.e. SU-8 anchors patterned within the etch holes holding the laminations after the copper removal). The nanolaminations were thin enough to suppress the eddy currents within the material (i.e. permalloy), thus, greatly reducing the loss at high operation frequency ( $> 1\text{MHz}$ ). The nanolaminations were operated up to  $0.5\text{ T}$ ; this demonstrates the potential of the miniaturized inductors of which sizes are much smaller than the ferrite-core devices, yet achieving similar level of power handling. Such TAME structures could also exhibit interesting properties that result from the strong mechanical anisotropy between the metal and the insulating polymer (e.g. PDMS) that would lead to further applications, such as magnetic sensors, or soft robotics.

## CHAPTER 5

# TAME-BASED MICRODEVICE: INTEGRATED ON-CHIP MICROINDUCTORS WITH LAMINATED CORES

### 5.1 Backgrounds & Motivation

In Chapters 3 and 4, fabrication of various TAME-based structured materials and their properties are discussed. In this chapter, we present an example of TAME-based microdevice, i.e., integrated microinductors, by combining micromachined toroidal windings with the developed nanolaminations.

As discussed in Chapter 1, there is a large difference between the hierarchical structures realized by bottom-up/bottom-up approaches and hybrid approaches. The former exhibits difficulties in creating the hierarchical structures at the desired position of a substrate, although its facile, economic nature enables large-scale production of multi-scale structures. On the contrary, the positions and geometries of the structures resulting from the hybrid processes are usually well-defined through top-down lithography. Hence, such processes are effective in “bridging” between microsystems and nanostructured materials, thereby, realizing microdevices with minimized form factor.

The TAME process offers such an opportunity. Since the TAME-based structures are lithographically registered, the realization of a TAME-based device could depend on standard microfabrication technology. However, for a specific type of the TAME structures, the process design may be a challenge due to the compatibility between the co-fabricated microsystems with TAME-based processes. For an example, the integration of a nanolaminated core to microwindings is not trivial although this may demonstrate an ultimate level of the compactness of a core-integrated inductor. The copper removal

process, that is crucial in the nanolamination process, is likely to damage any pre-fabricated structures (e.g. seed layers and microwindings) made of copper.

This chapter is dedicated to the discussions regarding how such challenges found in the realization of TAME-based devices can be addressed. Fully-micromachined, monolithically-fabricated (i.e. fabrication of all the compartments of a device performed on a single substrate) inductors with laminated cores are developed as an example.

## **5.2 Monolithic Integration of Microwindings and Laminated Cores**

An inductor is comprised of an  $N$ -turn conductive coil, a magnetic core, and an electrically-insulating layer (i.e. core-coil insulation layer) between the two. To achieve the ultimate compactness of an inductor with a given magnetic core, the coil needs to be wound around the core as “tightly” as possible. This not only means the highest winding density [turn/cm] (Figure 5.1(a)), but also means the thinnest core-coil insulation (while it is thick enough to isolate the core from the coil) (Figure 5.1(b)). The latter criteria can be quantified by the ratio between the cross-sectional area of the core, to the total cross-sectional area of the core and the core-coil insulation; this is referred to as a “core fill-factor.” The winding density as well as the core fill-factor of a core-integrated, manually wound, bobbin inductor shown in Chapter 4 is only about 16 turns/cm, and 4%, respectively.

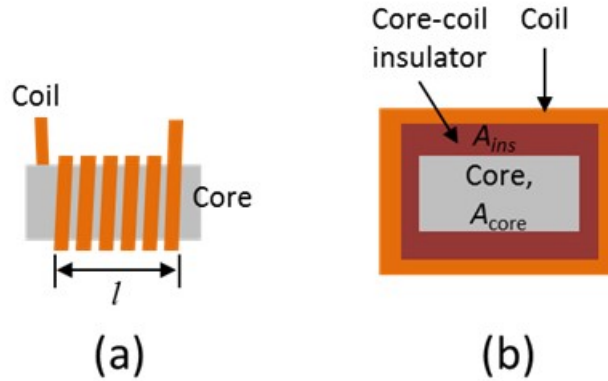


Figure 5.1 Definition of winding density and core fill-factor. (a) Schematic, top-view of an inductor. Winding density is winding turns divided by the core length. (b) Schematic, cross-sectional view of an inductor. When the cross-sectional area of the core and the insulator are  $A_{core}$  and  $A_{ins}$ , respectively, the core fill-factor is defined as  $A_{core}/(A_{core}+A_{ins})$ .

A drop-in core-winding integration approach has been developed (Figure 5.2) [90]. The fabrication of a laminated core and a microwinding is performed using two separate substrates. After the laminated cores are fabricated, the sample is detached from the original substrate and manually-dropped into the partially-fabricated microwindings. The integration is accomplished by finishing the winding fabrication. The winding density of the lithographically-defined coil of the integrated inductor exceeds that of the manually-wound inductor; however, the core fill-factor is still not maximized. This is mainly because of the precision of the manual core drop-in process is limited, and thus, the thickness of the core-coil insulation layer cannot be minimized.

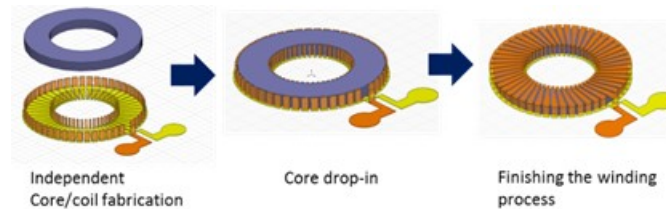


Figure 5.2 Drop-in core integration [90].



The co-fabrication of laminated cores and microwindings on a single substrate is designed to achieve the highest core fill-factor and the winding density, simultaneously. It is important to note that the post-processes performed on the laminated cores (e.g. photoresist casting and heating) may deform the thin, free-standing individual laminations that result in either degradation of magnetic properties and/or increase of interlayer conductivity between individual laminations, thereby increasing the eddy current loss within the core. Hence, from the structural point of view, it is desirable that the process finished as the (air-insulated) laminations are formed; this means the coils and the core-coil insulations need to be compatible to the sacrificial copper removal process.

The monolithic fabrication of the core and the microwindings, and thereby, the realization of a miniaturized microinductor is enabled by using silver as a winding material. The electrodeposited silver windings passivated in SU-8 exhibits superior compatibility to the copper removal process using the ammonical selective etchant. The copper removal process is the final process step in the inductor fabrication, reducing the possibility of post-processing-induced damage to the laminated core. Further, silver winding inductors may result in an increased inductor  $Q$ -factor due to its superior electrical conductivity compared to copper. The fabrication process, results, and characterization of the integrated inductors with air-insulated core laminations are followed. The compactness of the monolithically-integrated inductors are compared to the manually-wound and dropped-in-core inductors.

## 5.3 Design and Fabrication

### 5.3.1 Inductor Design

A pair of multi-turn solenoidal windings (i.e. 20 turns) are coupled with a rectangular laminated core, comprising a transformer. A solenoidal geometry is selected so that the characteristics of the integrated inductors can be directly compared with the manual-wound inductors. The solenoidal inductors are also beneficial compared to spiral inductors although the fabrication is more difficult; the inductance enhancement from the magnetic material can be maximized through this geometry.

The overall device design is shown in Figure 5.3. Figure 5.3(a) is a schematic top view of an integrated inductor with a rectangular laminated core. Figures 5.3(b) is schematic cross-sectional views of the inductor before and after the core release. Note that insulating SU-8 structures are (1) isolating the laminated core from the windings, (2) passivating the windings from the outer environment, and (3) anchoring the individual core laminations after the core release. The winding density (i.e. 4 turns/mm) is chosen considering the limitation of the lithography. The total thickness of the structure is designed to be around 100  $\mu\text{m}$  based on the maximum achievable thicknesses of the spun-cast photoresists employed in the process.

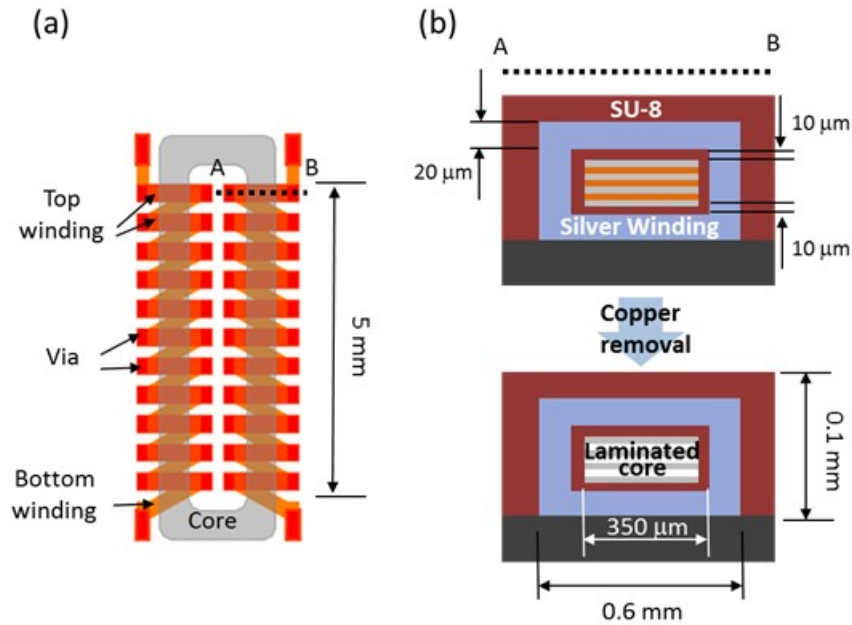


Figure 5.3 Inductor design. Schematics from (a) top-view and (b) cross-sectional view.

### 5.3.2 Materials

The monolithic fabrication of the integrated inductor is based on several repetitions of the steps: (1) Through-mold electrodeposition; and (2) SU-8 passivation. A thick negative photoresist, NR21-20000P (Futurrex) is chosen as the plating mold material, since it is compatible not only to the permalloy/copper multilayer electrodeposition, but also the electrodeposition of silver. Since the silver is deposited in a potassium hydroxide-based solution ( $\text{pH} = 12$ ), positive photoresists are not compatible with the process. The electrodeposition of silver is performed in a base electrolyte comprising silver potassium cyanide (70 g/L), potassium cyanide (110 g/L), potassium hydroxide (sufficient amount to tune the bath pH to 12) dissolved in DI water. The sputtered seed layer is a sandwich of

titanium, silver (rather than copper), titanium, with thicknesses of 30 nm, 250 nm, and 30 nm, respectively. The electrodeposition is performed at a current density of 2.5 mA/cm<sup>2</sup>. The deposition rate is 6 μm/hour; note that the rate is faster than the copper deposition by two-fold, since it takes only one electron to reduce a silver ion to silver metal. SU-8 is chosen as a core-coil insulation material because of its high chemical stability and photopatternability.

### 5.3.3 Fabrication Process

The integrated inductor fabrication procedure begins by sputtering a silver seed layer on a silicon wafer insulated with 1 μm-thick silicon dioxide. A through-mold electrodeposition of 15~20 μm-thick silver is performed for the bottom conductor fabrication (Figure 5.4(a)). After the mold is dissolved by an acetone rinse, the silver seed layer is blanket etched with diluted SC-1 (ammonium hydroxide/hydrogen peroxide) etchant.

The passivation of the bottom conductors follows by patterning a spun-cast SU-8 layer (Figure 5.4(b)). The SU-8 spin casting is performed in two steps: a non-viscous SU-8 solution (SU-8 2005, MicroChem) is first spun-cast on the sample wafer, and immediately after the first spin coat, a relatively viscous SU-8 (SU-8 2025, MicroChem) is spun on the sample to achieve a desired thickness of the SU-8 insulating layer. Without the first step, air bubbles can be trapped within the viscous SU-8 layer and the pre-defined topographies (e.g. sharp corners). The subsequent soft-bake may expand the trapped bubbles, causing a significant deformation of the insulating layer.

The exposure dose for the SU-8 is 50~60 % of the recommended value considering the superior UV reflectivity of silver; this is important since the SU-8 needs to be patterned so that the sites for the vertical conductors (or vias) are clearly exposed without being clogged by any over-crosslinked resist. Immediately after the SU-8 bottom conductor passivation layer is patterned, the sample is heated at 170 °C min for 5 min for a hard-bake. The hard bake temperature is set 20 °C higher than the soft bake temperature of the NR photoresist (which is used as a plating mold material); the hard bake is performed to (1) improve the adhesion between the SU-8 and the substrate, and (2) remove the solvent remaining in the patterned SU-8 so that the material becomes insensitive to the subsequent photoresist soft bake processes. After the SU-8 is hard-baked, an oxygen descum process follows to ensure complete removal of residual SU-8. Finally, the sample is rinsed in a diluted ammonium hydroxide solution to remove the oxidized silver; this should be performed immediately before the deposition of a new seed layer. Such silver conductor patterning and SU-8 passivation processes are similarly repeated in the subsequent fabrication steps.

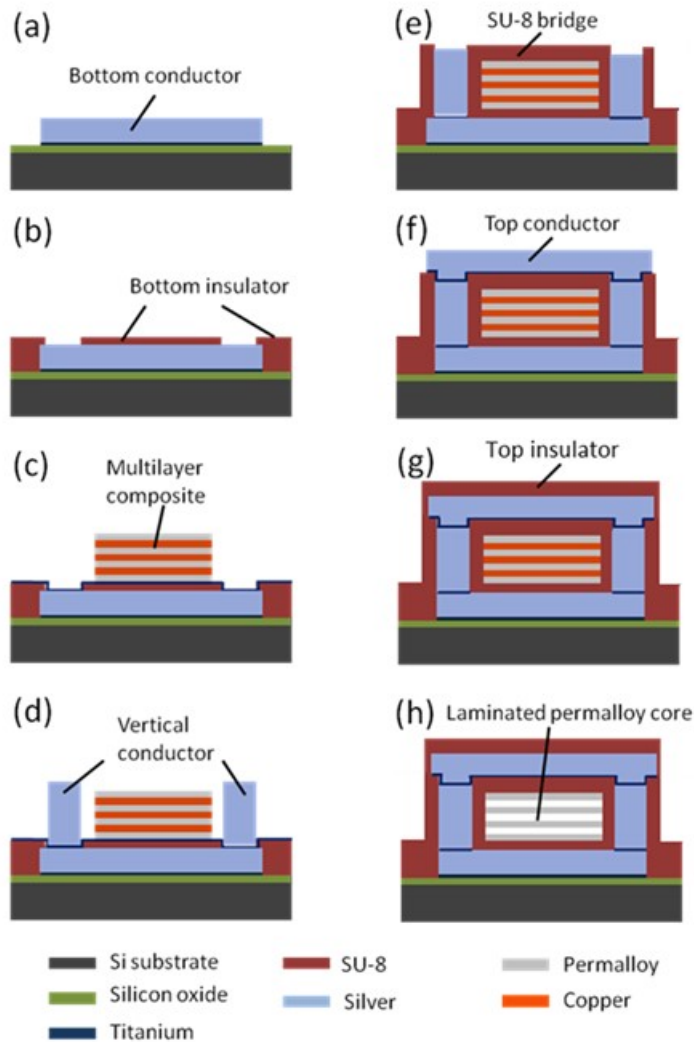


Figure 5.4 Fabrication sequence.

A TAME process is performed using a 50  $\mu\text{m}$ -thick, spun-cast NR mold to build a multilayered core, 40  $\mu\text{m}$  in total thickness comprised of alternating layers of 1  $\mu\text{m}$ -thick permalloy and 1  $\mu\text{m}$ -thick copper (Figure 5.4(c)). Vertical conductors are through-mold electrodeposited (Figure 5.4(d)), followed by patterning of SU-8 bridges which passivate the sidewalls of the vertical conductors as well as a portion of the top side of the

permalloy/copper multilayer core (Figure 5.4(e)). After the top conductors are plated along the bridges (Figure 5.4(f)), it is again passivated with SU-8 (Figure 5.4(g)). After this step, the silver windings are completely encapsulated with SU-8. Finally, the core is released by a selective removal of copper from the multilayers (Figure 5.4(h)) as described previously, and air-insulated laminations are created within the silver microwindings. Considering the width of the multilayer core (350  $\mu\text{m}$ ), and the geometry of the SU-8 bridges, the copper removal process is performed for 5~6 hours.

### 5.3.4 Fabrication Results

Figure 5.5 shows a series of SEM pictures taken during the process. Figure 5.5(a) shows a low magnification view of the fabricated silver bottom conductors. Figure 5.5(b) shows the vertical conductors embedded in the SU-8 bridges before the top conductor fabrication; note that an angled imaging is performed to show thin ( $< 10 \mu\text{m}$ ) SU-8 insulation layer covering the deposited multilayer. Figure 5.5(c) shows the sidewall of the deposited, solid multilayer structure.

Figure 5.5(d) shows the SU-8 bridges isolating the silver windings from the laminated core. Figures 5.5(e) and 5.5(f) show a bird-eye view of the inductor after the copper removal process. The windings are completely embedded inside SU-8 (dark grey). From Figure 5.5(f), the sideview of the released laminated cores is observed. Individual permalloy layers are well-separated without suffering from stiction after the release/sample drying process, validating that the layers are effectively anchored by the SU-8 bridge structures.

Figure 5.6 shows an optical image of a single die after the fabrication. Two pairs of integrated inductors are presented in a single die. Figure 5.6(b) shows an optical picture taken by a stereoscope. The windings are packaged inside the transparent SU-8 structures. A single inductor has a footprint of less than  $3 \text{ mm}^2$  (excluding the electrical pads) and a device thickness of  $\sim 100 \text{ }\mu\text{m}$ .

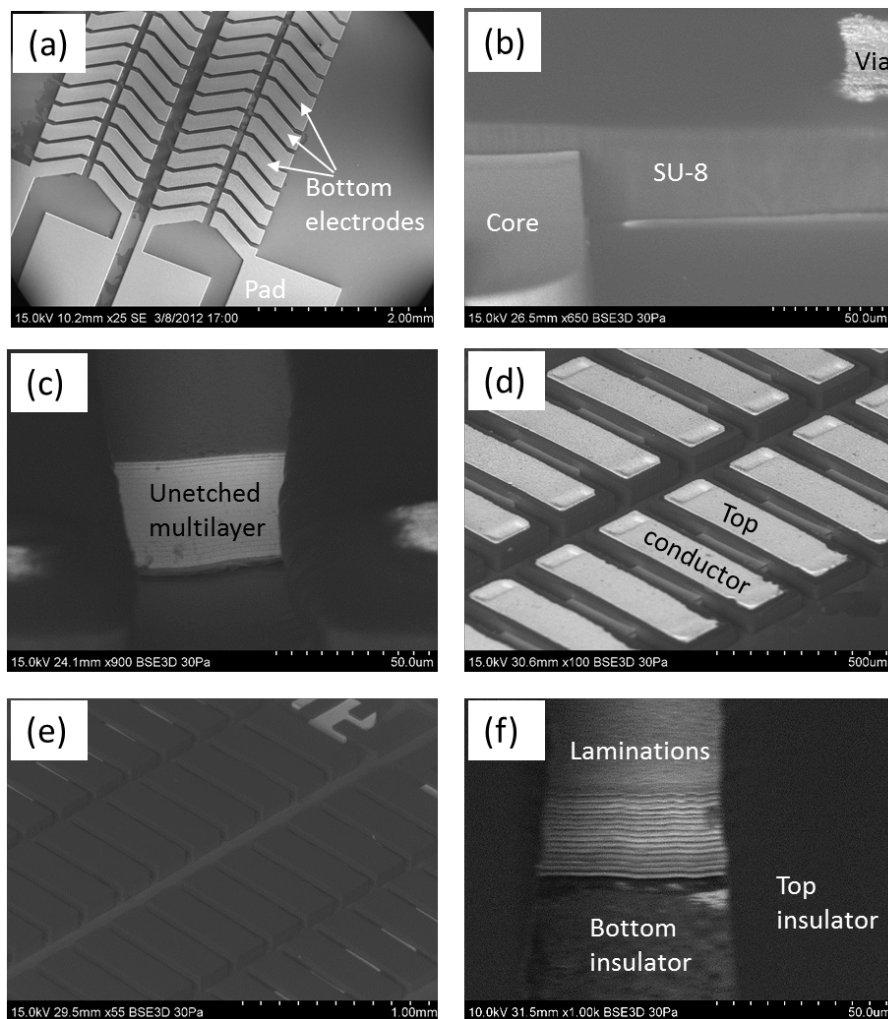


Figure 5.5 SEM pictures of the fabricated samples. (a) After the bottom conductor fabrication. (b), (c) After the vertical conductor formation. (d) After the top conductor fabrication. (e), (f) After the selective copper removal.



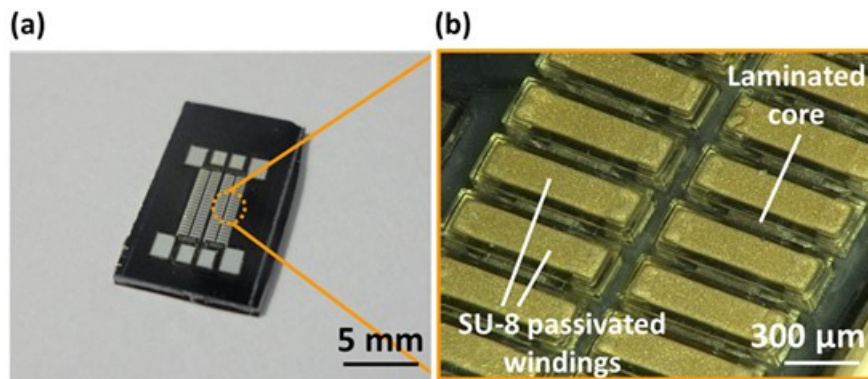


Figure 5.6 Optical images of the fabricated integrated inductors. (a) Image of a single die. (b) Closer view imaged with a stereoscope.

#### 5.4 Inductor Characterization

The inductors are characterized based on the impedance analyzer, similar to the measurement of the manual-wound inductors presented in Chapter 4; Figure 5.7 shows the measured inductances and  $Q$  of two inductors with the same design, at a 2 mT operating flux. To validate the formation of the air-insulated laminations, the measurement is performed before, and after the copper removal. Before the core release, both inductors exhibit low inductances ( $\sim 20$  nH) as well as low  $Q$  factor ( $< 1$ ) at frequencies above 5 MHz. This is due to the eddy current loss induced within magnetic cores thicker than the frequency-dependent magnetic skin depth. However, the inductance and  $Q$  factor of both inductors greatly increase after the copper release, as eddy currents can no longer flow in the air-insulated laminated core; the result is analogous to the *in-situ* measurement discussed in Chapter 4. The inductances of both inductors are very similar ( $> 100$  nH), proving a successful fabrication.

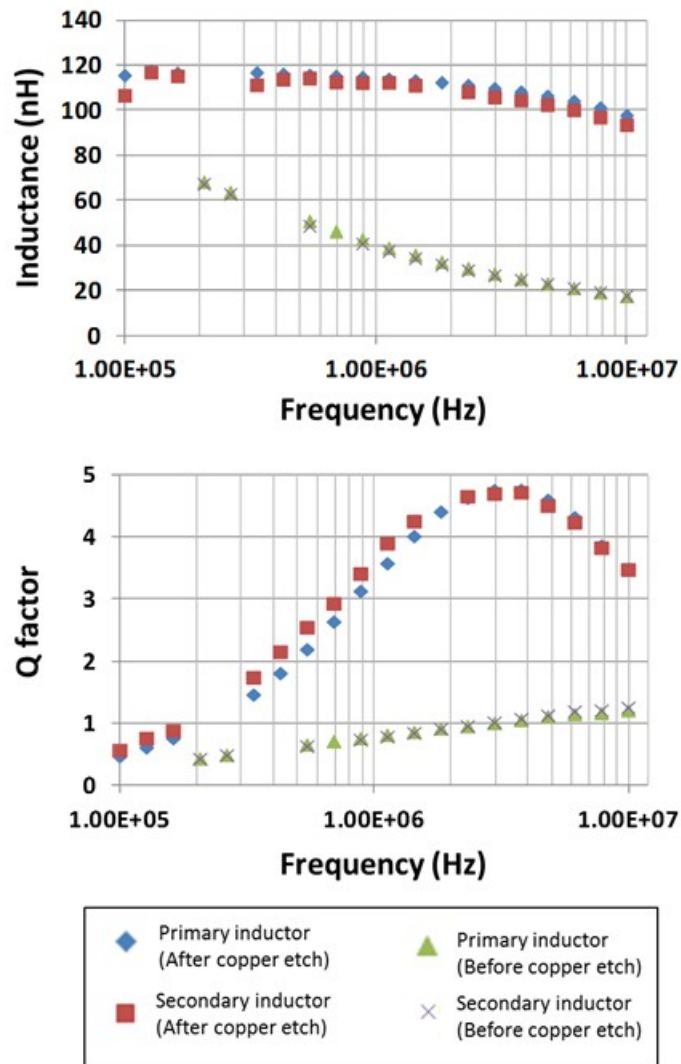


Figure 5.7 Inductance and  $Q$  of a pair of integrated inductors sharing a same laminated core. The measurement is performed before, and after the copper removal.

An air-core inductance of the inductor ( $L_{air}$ ) of 3.5 nH is calculated from the actual coil dimensions using the following equation:

$$L_{air} = \frac{\mu_0 A_{air} N^2}{l} \quad (5.1)$$

where  $l$  is the length of the inductor (5 mm),  $A_{\text{air}}$  is the cross-sectional area of the inductor without a core ( $350 \times 100 \mu\text{m}^2$ ), and  $N$  is the number of the coil turns (20 turns). For an integrated inductor, the inductance is:

$$L = \frac{(\mu_0 A_{\text{ins}} + \mu_{\text{eff}} \mu_0 A_{\text{core}}) N^2}{l} \quad (5.2)$$

where  $\mu_{\text{eff}}$  is the effective relative permeability of the laminated core. Note that the inductance improvement due to the core integration, which is characterized by  $L/L_{\text{air}}$ , is as high as 33 due to the compactness of the device. Ideally, the effective permeability should be 500, i.e., a half of the relative permeability of a single layer permalloy, since the volume portion of the air within the air-laminated core is 50%. However, based on the measured inductance (115 nH), the calculated effective permeability is only  $\sim 125$ .

Both micro- and macroscopic structural properties of the laminations seem responsible for the smaller effective permeability. It should be noted that the permeability of the reference, 1  $\mu\text{m}$ -thick, single permalloy film was measured from a vibrating sample magnetometer. The B-H loop of the magnetic material was measured by inducing a time varying field at a low frequency (60 Hz) while the sample was being fully saturated at peak field intensities. On the contrary, the operating condition of a laminated core in the impedance analyzer is very different; the material is subjected to a smaller peak flux of 2 mT, at much higher frequencies (500 kHz~10 MHz). According to the recent studies [91, 92], the shape of a hysteresis loop can vary with respect to excitation level and operation frequency; permeability measured at high frequency (and at low excitation) can be significantly smaller than the measurement results in near DC field, more than a factor of

2. An additional, excess eddy current loss due to the domain wall rotation is considered as a main reason for the dynamic nature of hysteresis [91].

Another potential reason behind the effective permeability decrease is an unexpected demagnetization within the magnetic laminations [93]. Demagnetization factor  $N_d$  of a core with a rectangular cross-section area is a function of the core geometry [93, 94]. The effective permeability of a laminated core after considering this effect is expressed as:

$$\mu_{eff,demag} = \frac{\mu_r}{1 + N_d(\mu_r - 1)} \quad (5.3)$$

where  $\mu_r = 500$  (note that the magnetic material is an air-laminated core), and  $N_d = 0.0035\sim 0.004$  [94]. Note that  $\mu_{eff,demag}$  can be as small as 167. In summary, a combined effect due to the microscopic domain structures and the macroscopic geometries of a laminated core could result in the reduction of the effective permeability by a factor of 4~5. Further studies are required to accurately model the effective permeability, and thus, enable the design of the core to achieve desired inductor performance.

The silver winding is designed to be embedded in SU-8, since the silver is observed to be etched in copper etchant (even though the rate is slow). To assess the validity of this approach, the sample with a complete encapsulation, and the sample without the top SU-8 insulation layer (hence, the top conductors being exposed) are immersed into the copper etchant. The samples are periodically taken out from the etchant, and the resistances of both samples at low frequency (~100 KHz) are measured (Figure 5.8). Compared to the resistance of the completely encapsulated sample (0.2  $\Omega$ , calculated silver resistivity = 3.2

$\times 10^{-8}$  [Ohm·m]) the resistance of the sample without SU-8 passivation is drastically increased throughout the process. The resistance exceeds 1 M $\Omega$  after 30 hours, indicating that the coil has lost its electrical connectivity.

Given that, the calculated silver etch rate in the copper etchant is approximately  $\sim 0.5$   $\mu\text{m}/\text{hour}$ ; this is around 60~100 times slower than the copper etch rate. This result suggests that the SU-8 passivation steps may be neglected to simplify the overall fabrication process by appropriately designing the core, SU-8 bridges and winding dimensions.

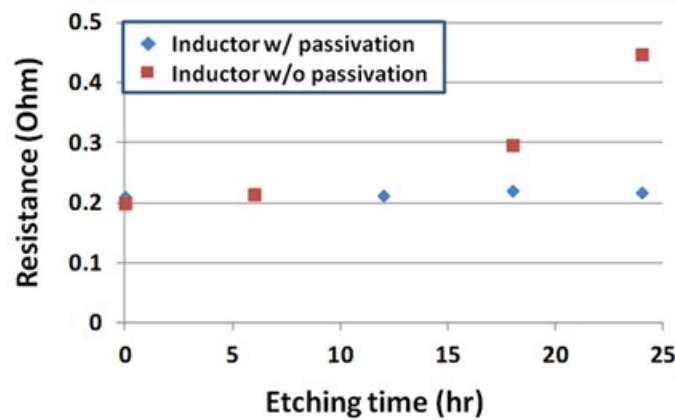
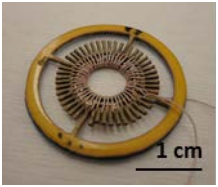
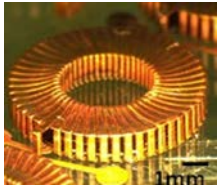
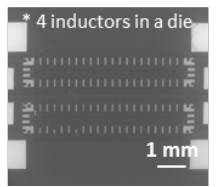


Figure 5.8 Inductor resistance versus sample immersion time in copper etchant.

The size, winding density, and core fill-factor of the various inductors (i.e. manually-wound polymer bobbin inductors, integrated inductors with dropped-in cores, and monolithically-fabricated inductors) are compared (Table 5.1). The inductances of the air-core inductors (i.e. the inductors with the identical winding design without the laminated cores inside) are measured from the actual samples, or calculated. These values

are compared to the inductances of the integrated inductors. The monolithically-fabricated inductor shows the largest inductance improvement due to the core integration (35-fold); this results from the large core fill-factor of 46%. The inductance per footprint, (42.1 nH/mm<sup>2</sup>) and per volume (421 nH/mm<sup>3</sup>) are also larger than that of the counterparts due to the improved compactness of the integration.

Table. 5.1 Specification of the inductors.

| Integration approach<br>Inductor specification | Manually-wound   | Micromachined (Drop-in CoNiFe core [90])  | Micromachined (Monolithic)   |
|--|--|---|--|
| Images   |  |  |  |
| Footprint (mm <sup>2</sup> )                   | 87   | 50  | 2.6  |
| Volume (mm <sup>3</sup> )                      | 87   | 50  | 0.26   |
| Winding density (turns/mm)                     | 1.6  | 2   | 4  |
| Core fill-factor (%)                           | 4  | 6   | 46   |
| Air-core inductance, $L_{\text{air}}$ (nH)     | 250 (measured)   | 210 (measured)  | 3.5 (calculated)   |
| Inductance of the inductor, $L$ (nH)           | 1600   | 1800  | 115  |
| Inductance improvement ( $L/L_{\text{air}}$ )  | 6.4  | 8.6   | 35   |
| Inductance per footprint (nH/mm <sup>2</sup> ) | 18.4   | 35.8  | 42.1   |
| Inductance per volume (nH/mm <sup>3</sup> )    | 18.4   | 35.8  | 421  |

The measured inductance, which is relatively small, can be scaled-up by various approaches. The first (obvious) option is to connect more inductors in series. The second option is to integrate thicker core laminations to achieve larger total magnetic volume per given footprint. For this approach, a removable photoresist of higher achievable thickness is required (e.g. removable plating mold with a few hundred-of-microns can be achieved with a photopatternable resist, AZ 15nXT). The third is to use the magnetic materials with higher permeability (e.g. CoNiFe), as discussed in Chapter 4. By combining a thick core laminations with a proper material, the inductance as well as the inductance density (i.e. inductance per given device footprint) can be simultaneously improved. However, using the material with the highest permeability is not always desirable for certain applications, e.g., switched-based DC-DC power conversion, since such material is saturated at relatively low excitation, and thus, unable to handle sufficiently high current. Based on the better understanding on non-linear, dynamic behavior of a magnetic material, an optimized design of an integrated inductor could be enabled for specific applications.

## 5.5 Summary

Monolithically-fabricated silver inductors with nanolaminated cores is demonstrated as an example of TAME-based devices. Fabrication of the microdevice was performed based on the carefully chosen set of materials (i.e. silver is selected as a winding material, SU-8 is selected as a core-coil insulation material), so as to achieve a proper compatibility between various processes including the nanolamination process.

The fabrication results showed that microwindings can be closely coupled to the TAME-structures; this is mainly because the positions of both windings and TAME

structures were lithographically defined. The distance between the winding and the core was only about 50  $\mu\text{m}$ , the value of which was set based on the margin required for the alignment of multiple mask layouts; the thickness of the spun-cast SU-8 core-coil insulator was approximately 10  $\mu\text{m}$ .

Such compact integration enabled a TAME-based microdevice of miniaturized footprint. The inductances of the integrated inductors at high frequency were corresponding to the suppressed eddy current losses, while the air-insulated laminations were co-fabricated with the tightly-wound microwindings. As a result, the inductance improvement due to the core integration was higher compared to the other types of core-winding integration approaches. In conclusion, a miniaturized, TAME-based device was achieved without compromising the functionalities of TAME structures. The batch-fabricated, miniaturized core integrated inductors are potential candidates for multiphase power conversion that uses a number of parallel power stages to drive a single load.



# CHAPTER 6

## CONCLUSION

### 6.1 Summary of Conducted Research

In accordance to the purpose of this research, the TAME process is developed as a controllable, yet scalable route to surface and volumetric hierarchical structures. The TAME process combines lithography-based template fabrication processes and conformal multilayer electrodeposition (Chapter 2.1). In order to create multilayer structures with multiple individual layers with arbitrary thicknesses, an automated multilayer electrodeposition process is developed. Multilayer structures of which individual layer thicknesses ranging between 30~5000 nm are demonstrated by using proper materials (i.e. nickel, permalloy ( $\text{Ni}_{80}\text{Fe}_{20}$ ), copper), deposition baths as well as deposition parameters (Chapter 2.2). A mathematical model based on an ideal growth hypothesis (i.e. isotropic, constant rate of nickel and copper) is developed to predict the TAME structures from initial process parameters (i.e. seed layer pattern, deposition parameters) (Chapter 2.3).

A three-dimensional growth, guided by a proper template, leads to the fabrication of large- area ( $> 10 \text{ cm}^2$ ) hierarchical surface relief structures of various architectures, of which nanostructure pitches are defined by the individual layer thicknesses of nickel and copper, and the microstructures defined by the template geometry (Chapter 3.1). Planar relief structures can be transferred to different functional materials (i.e. thermoplastics, silicon) by imprinting. Nanoimprinting lithography is demonstrated by using a room temperature-imprinted resist as a silicon etch mask (Chapter 3.2). Superhydrophobic films are demonstrated by using non-planar, hierarchical relief structures (Chapter 3.3). Through a single step replica molding using a hydrophobic elastomer, h-PDMS, both micro- and

nanostructures of the multilayers are accurately replicated. The structural hierarchy of the PDMS structures results in a superhydrophobicity which is characterized by high static water contact angle ( $> 150^\circ$ ), small hysteresis ( $10^\circ$ ), and small sliding angle ( $12^\circ$ ). In addition, the hierarchical, metallic TAME structures can be also used as superhydrophobic structures after the surfaces are treated by a vaporized silane (i.e. TFOCS). Such structures with superior mechanical robustness could be useful as non-wetting surfaces in a relatively harsh environments (e.g. underwater, high temperature) (Chapter 3.4).

A one-dimensional TAME process, combined with a complete copper removal, leads to the realization of a volumetric hierarchical structure, i.e., nanolaminations, where the individual layer thicknesses of a soft magnetic metallic permalloy as well as the interlamination insulations (i.e. air, PVA, PDMS) are significantly smaller than the skin depth of the material at high frequency ( $3\ \mu\text{m}$  at 10 MHz) (Chapter 4.2). Suppressed eddy currents within the laminations (with single micron-thick permalloy layers) are observed by operating the material at high frequency (1~10 MHz) and high magnetic flux (0.1~0.5 T). At such high flux, the power handling capacity of the laminated materials surpass that of conventional ferrites. The developed material could eventually lead to the ultimate miniaturization of switch-based power converters (Chapter 4.3).

Since the orientation and registration of the TAME structures are lithographically defined, they can be readily integrated into external microstructures to form microdevices. A monolithic fabrication approach is developed to co-fabricate toroidal microwindings and permalloy nanolaminations, and thereby, realize microinductors in batch-scale (Chapter 5.2). Silver was chosen as the winding material considering the compatibility with the lamination process, i.e., selective copper removal. The fabricated microdevices show

relatively high inductance density ( $42 \text{ nH/mm}^2$ ) compared to their counterparts (e.g. polymer bobbin-packaged, manually-wound inductor, microinductors with dropped-in laminated cores) with suppressed eddy currents up to high operation frequencies ( $> 1 \text{ MHz}$ ) (Chapter 5.3). With an appropriately designed fabrication procedure, various TAME structures could be packaged into microstructures of miniaturized form factors without their TAME functionalities being compromised.

## **6.2 Suggestions for Future Research**

The ultimate versatility of a fabrication technique would be achieved if an arbitrary structure with an arbitrary, desired material can be realized through the process in a reasonably economic manner. From such a perspective, future researches that may improve the versatility of the TAME process are discussed. Additional application domains that could benefit from the TAME processes are also suggested.

### **6.2.1 Patterning at Smaller Scale**

The presented dual-bath deposition technique may not be an optimum method to produce sub-50 nm scale structures. Undesirable effects from potential surface reactions including surface oxidation, or displacement reaction may dominate at such small size scales. In addition, the process time is increased drastically as the number of the deposition sequence required to achieve a specific total multilayer thickness is increased. The total process time  $t_p$  to build a multilayer structure as thick as  $r$  with a single periodicity,  $p$ , is calculated as below:

$$t_p = \frac{r}{2G_{\text{Ni}}} + \frac{r}{2G_{\text{Cu}}} + \frac{r}{2p} t_b$$

where  $G_{\text{Ni}}$  [nm/s] is the growth rate of nickel,  $G_{\text{Cu}}$  [nm/s] is the growth rate of copper, and  $t_b$  [s] is the "idle" time, defined as the amount of time that the sample is not subjected to the electrodeposition, per a pair of sequence of a nickel and a copper layer deposition. The term  $t_b$  includes wafer transition time through multiple numbers of baths as well as the rinsing process time. This equation shows that the deposition time could be dominated by the idle time for the deposition of multilayer structures with small periodicities. For these reasons, a single-bath deposition could be a better approach for the realization of the TAME structures with very small periodicities ( $p < 50$  nm).

It should be noted that the TAME process can be further extended by using a different type of selective, multilayer deposition technique with properly chosen template and sacrificial layer materials. For example, atomistic layer thickness control of epitaxial multilayer growths could result in very fine ( $p < 10$  nm) TAME structures at the expense of higher process cost.

### **6.2.2 Improving Structural Diversity with Extended TAME Process**

The TAME process is suited for the realization of anisotropic nanostructures (i.e. structures with very small width and large length, or vice versa) that are concentric to the microscale geometry of a template. The achievable structural diversity of the TAME process can be further improved.

First, a seed layer pattern that comprises initially isolated patterned conductors can be used to produce a surface relief pattern with non-concentric geometries. Figure 6.1 describes the TAME process based on such template.

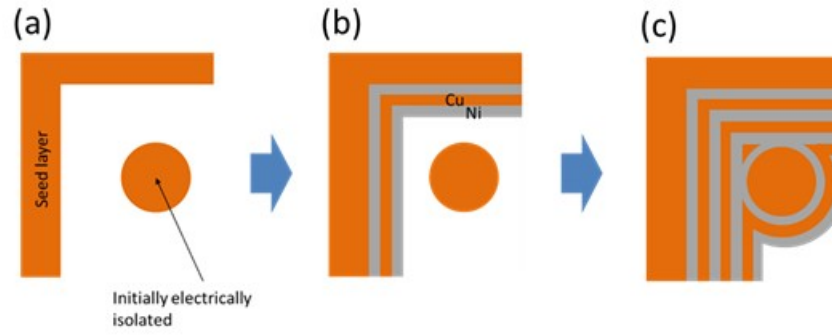


Figure 6.1 Extended TAME process based on a seed layer with initially isolated conductors

The multilayer structure growth begins only from the electrically connected patterns of the seed layer (Figure 6.1(a),(b)). After a multilayer structure with a specific total thickness is achieved, the initially isolated patterns are connected to the growing multilayers. The multilayer grows from the newly defined conductors throughout the subsequent deposition sequences (Figure 6.1(c)). This approach allows the realization of various types of nanostructures that are not concentric to a patterned geometry of a seed layer.

Second, a new process, i.e. isotropic wet etching, can be incorporated into a multilayer deposition unit cycle. Figure 6.2 depicts the process. First, the first layer of nickel is deposited on the copper seed layer (Figure 6.2(a),(b)). Second, the deposited nickel is selectively, and isotropically etched until only a portion of the material remains within the corner of the seed (Figure 6.2(c),(d)). The size of the remaining nickel structure

(or, a lateral dimension of the nickel) is, therefore, defined not only by the deposited nickel layer thickness, but also the etched thickness of the nickel. Then, a copper layer is deposited on the etched sample. The next cycle begins with a subsequent nickel layer deposition (Figure 6.2(e),(f)). This process enables the realization of “dot-like,” isotropic structures, where the distances between the isolated nickel structures are defined by the inter-nickel copper layer thicknesses. Dot-like protruded structures are formed after selective copper etching; “hole-like” structures can be also formed by selective etching of nickel. By using a thick, through-molded metal as a seed layer, high vertical aspect ratio pillar structures (or hole-type structures) could be formed.

These two examples of extended version of TAME process are also scalable; unlimited number of structural copies can be simultaneously formed within a single multilayer deposition process. These “thought experiments” show that non-concentric structures, or nearly isotropic structures can be top-down synthesized by extending the TAME process.

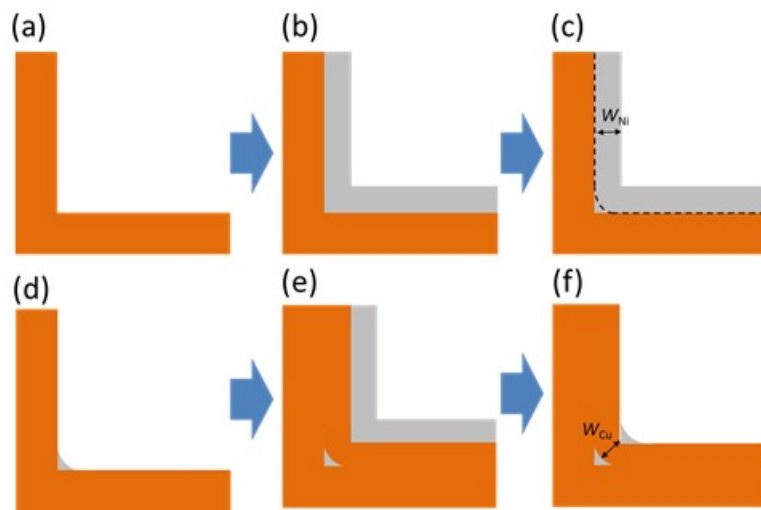


Figure 6.2 Isotropic nickel structures formed by an extended TAME process

### **6.2.3 Other Pattern Transfer Techniques**

In Chapter 3, pattern replication using PDMS is demonstrated. Not only the planar type TAME structures, but also their PDMS replica can be used as the master stamps for subsequent pattern transfer processes. Elastomeric, transparent nature of the PDMS structures are suited for UV-imprint nanolithography [54], or soft lithography [51], where relatively small pressure is required for a pattern transfer. Direct patterning of functional materials (e.g. metal colloids [95]) should be possible using the flexible molds. Pattern transfer techniques combined with various master patterns realized through the extended TAME processes could further improve the process versatility; a rich variety of processes based on TAME could be regarded as low-cost, generalized routes to controlled nanostructures.

### **6.2.4 Potential Applications**

The studies regarding the superhydrophobic surfaces could lead to a scalable route to non-wetting, patch-type structures with proper structural robustness. Such structures are also expected to be useful in microfluidic devices. First, hierarchical, superhydrophobic PDMS structures could reduce the solid-water drag of a pressure-driven flow, thereby, reduce the required pressure to operate a fluidic device [96]. Second, surfaces possessing a wettability gradient could be realized through optimal design of structural hierarchy. These structures would provide a guide to the dispensed droplets in open microfluidics, thereby, potentially useful in microscale material transport [71]. Third, hierarchical topographic cues are known to guide a designed, anisotropic cell (e.g. neuron) growth [97].

Integration of the TAME-based surface structures into microfluidics will foster related studies.

A polymer packaging, nanolamination technique based on PDMS infiltration is presented. The packaged material may exhibit many interesting mechanical and thermal volumetric properties. The PDMS-infiltrated laminations may exhibit much higher flexibility compared to a single layer permalloy sample with similar total metal thickness. The thermal resistance across the laminations will be considerably lower than the resistance along the sample due to dense metal-insulator interfaces. Characterization of these laminations in various physical regimes might reveal new applications for this material.

Table 6.1 Achievable TAME structures and their functionalities (Black/bold: Demonstrated in this thesis, Black/italic: Demonstrated, not being a subject of the thesis, Red: To be demonstrated).

|   | Fabrication process  |  | Structures  |  | Functionality   |
|---|--|--|---|--|---|
|   | TAME process   | Post-deposition process                                      | Microstructures   | Nanostructures                                       |   |
| <b>Surface hierarchical structures</b>    | Planar template + 3D Multilayer deposition                 | Selective copper etching, PDMS replication or nanoimprinting | Low-aspect ratio nanostructures within planar seed patterns |  | <b>Master molds,</b><br><i>Optical birefringence</i>    |
|   | Planar template with thick seed + 3D Multilayer deposition | Selective copper etching                                     | Low-aspect ratio nanostructures within planar seed patterns |  | <i>Supercapacitor[3], battery</i>                       |
|   | 3D template + 3D Multilayer deposition                     | Selective copper etching, PDMS replication                   | Pillars   | Concentric, low-vertical aspect ratio nanostructures | <b>Non-wetting surfaces</b>                             |
|   | 3D template + 3D Multilayer deposition                     | Selective copper etching, PDMS replication                   | Stripes   | Concentric, low-aspect ratio nanostructures          | <i>Anisotropic wetting</i>                              |
| <b>Volumetric hierarchical structures</b> | Planar template + 3D Multilayer deposition                 |  | Desired conductor geometry                                  | Conformal coating on the initial seed layer          | <i>Low conductor loss at high frequencies[20]</i>       |
|   | 3D template + 1D Multilayer deposition                     | Anchor fabrication + Copper removal + Polymer infiltration   | Toroids, rectangular  | Metal-insulator laminations                          | <b>Magnetic materials with suppressed eddy currents</b> |



Interesting optical, and electrochemical surface properties could be harnessed from the TAME structures, leading to various applications. Subwavelength optical properties (e.g. birefringence) could be induced from the as-fabricated, planar TAME surface relief structures. Vertically-aligned high aspect ratio TAME electrodes could be a useful template toward catalysts, supercapacitor, and batteries that could benefit from high surface-to-volume ratio of a structure. The electrodes with highly controlled nanostructures are desirable for these applications, because the prediction of chemical reaction rates is relatively feasible. This allows an optimal structural design for a desired application.

Table 6.1 shows a list of the achievable TAME structures; useful functionalities that may result from the respective structures are stated in the last column of the table. Only a portion of them has been subjects of extensive research (the ones written in bold being major topic of this thesis); further efforts on TAME process development could open a manufacturable route to materials and devices with distinct functionalities in various nanoapplication domains.

## REFERENCES

- [1] Y. Xiu *et al.*, “Hierarchical silicon etched structures for controlled hydrophobicity/superhydrophobicity,” *Nano Letters*, vol. 7, no. 11, pp. 3388-3393, 2007.
- [2] G. Duan *et al.*, “Hierarchical surface rough ordered Au particle arrays and their surface enhanced Raman scattering,” *Applied Physics Letters*, vol. 89, no. 18, pp. 181918, 2006.
- [3] A. Armutlulu *et al.*, “Supercapacitor electrodes based on three-dimensional copper structures with precisely controlled dimensions,” *ChemElectroChem*, vol. 2, no. 2, pp. 236-245, 2015.
- [4] M. Melzer *et al.*, “Imperceptible magnetoelectronics,” *Nature Communications*, vol. 6, 2015.
- [5] H. B. Yao *et al.*, “25Th anniversary article: Artificial carbonate nanocrystals and layered structural nanocomposites inspired by nacre: Synthesis, fabrication and applications,” *Advanced Materials*, vol. 26, no. 1, pp. 163-188, 2014.
- [6] L. J. Guo, “Nanoimprint lithography: Methods and material requirements,” *Advanced Materials*, vol. 19, no. 4, pp. 495, 2007.
- [7] K. Y. Suh, and H. H. Lee, “Capillary force lithography: Large-area patterning, self-organization, and anisotropic dewetting,” *Advanced Functional Materials*, vol. 12, no. 6-7, pp. 405-413, 2002.
- [8] M. K. Kwak *et al.*, “Towards the next level of bioinspired dry adhesives: New designs and applications,” *Advanced Functional Materials*, vol. 21, no. 19, pp. 3606-3616, 2011.
- [9] K. Efimenko *et al.*, “Nested self-similar wrinkling patterns in skins,” *Nature Materials*, vol. 4, no. 4, pp. 293-297, 2005.
- [10] K. H. Nam, I. H. Park, and S. H. Ko, “Patterning by controlled cracking,” *Nature*, vol. 485, no. 7397, pp. 221-224, 2012.
- [11] S. H. Ko *et al.*, “Nanoforest of hydrothermally grown hierarchical ZnO nanowires for a high efficiency dye-sensitized solar cell,” *Nano Letters*, vol. 11, no. 2, pp. 666-671, 2011.
- [12] V. Kitaev, and G. A. Ozin, “Self-Assembled Surface Patterns of Binary Colloidal Crystals,” *Advanced Materials*, vol. 15, no. 1, pp. 75-78, 2003.

- [13] I. Bitá *et al.*, “Graphoepitaxy of self-assembled block copolymers on two-dimensional periodic patterned templates,” *Science*, vol. 321, no. 5891, pp. 939-943, 2008.
- [14] J. Y. Cheng, A. M. Mayes, and C. A. Ross, “Nanostructure engineering by templated self-assembly of block copolymers,” *Nature Materials*, vol. 3, no. 11, pp. 823-828, 2004.
- [15] R. Ruiz *et al.*, “Density multiplication and improved lithography by directed block copolymer assembly,” *Science*, vol. 321, no. 5891, pp. 936-939, 2008.
- [16] F. Zhang, and H. Y. Low, “Anisotropic wettability on imprinted hierarchical structures,” *Langmuir*, vol. 23, no. 14, pp. 7793-7798, 2007.
- [17] H. Zhang, X. Yu, and P. V. Braun, “Three-dimensional bicontinuous ultrafast-charge and-discharge bulk battery electrodes,” *Nature Nanotechnology*, vol. 6, no. 5, pp. 277-281, 2011.
- [18] S.-J. Jeong *et al.*, “One-dimensional metal nanowire assembly via block copolymer soft graphoepitaxy,” *Nano Letters*, vol. 10, no. 9, pp. 3500-3505, 2010.
- [19] J.-H. Lee *et al.*, “Anisotropic, hierarchical surface patterns via surface wrinkling of nanopatterned polymer films,” *Nano Letters*, vol. 12, no. 11, pp. 5995-5999, 2012.
- [20] A. Rahimi, and Y.-K. Y. Yoon, "Low loss conductors for CMOS and through glass/silicon via (TGV/TSV) structures using eddy current cancelling superlattice structure." *IEEE Electronic Components and Technology Conference*, pp. 736-741, May 2014 (Orlando, FL, USA).
- [21] M. S. Onses *et al.*, “Hierarchical patterns of three-dimensional block-copolymer films formed by electrohydrodynamic jet printing and self-assembly,” *Nature Nanotechnology*, vol. 8, no. 9, pp. 667-675, 2013.
- [22] Y. Mai, and A. Eisenberg, “Self-assembly of block copolymers,” *Chemical Society Reviews*, vol. 41, no. 18, pp. 5969-5985, 2012.
- [23] Y. Liu *et al.*, “Mechanical properties of highly textured Cu/Ni multilayers,” *Acta Materialia*, vol. 59, no. 5, pp. 1924-1933, 2011.
- [24] M. Kolle *et al.*, “Mimicking the colourful wing scale structure of the *Papilio blumei* butterfly,” *Nature Nanotechnology*, vol. 5, no. 7, pp. 511-515, 2010.
- [25] N. A. Melosh *et al.*, “Ultrahigh-density nanowire lattices and circuits,” *Science*, vol. 300, no. 5616, pp. 112-115, 2003.

- [26] G.-Y. Jung *et al.*, "Circuit fabrication at 17 nm half-pitch by nanoimprint lithography," *Nano Letters*, vol. 6, no. 3, pp. 351-354, 2006.
- [27] R.-G. Huang *et al.*, "High performance ring oscillators from 10-nm wide silicon nanowire field-effect transistors," *Nano Research*, vol. 4, no. 10, pp. 1005-1012, 2011.
- [28] M. C. McAlpine *et al.*, "Highly ordered nanowire arrays on plastic substrates for ultrasensitive flexible chemical sensors," *Nature Materials*, vol. 6, no. 5, pp. 379-384, 2007.
- [29] C.-Y. Lim *et al.*, "Development of an electrodeposited nanomold from compositionally modulated alloys," *Journal of Applied Electrochemistry*, vol. 34, no. 8, pp. 857-866, 2004.
- [30] P. Mardilovich, and P. Kornilovitch, "Electrochemical fabrication of nanodimensional multilayer films," *Nano Letters*, vol. 5, no. 10, pp. 1899-1904, 2005.
- [31] S. Arai, T. Hasegawa, and N. Kaneko, "Fabrication of three-dimensional Cu/Ni multilayered microstructure by wet process," *Electrochimica Acta*, vol. 49, no. 6, pp. 945-950, 2004.
- [32] W. P. Gallé, "MEMS-based fabrication of power electronics components for advanced power converters," Ph D. dissertation, Department of Electrical and Computer Engineering, Georgia institute of Technology, Atlanta, GA, USA, 2012.
- [33] C. Ross, "Electrodeposited multilayer thin films," *Annual Review of Materials Science*, vol. 24, no. 1, pp. 159-188, 1994.
- [34] W. Blum, "The structure and properties of alternately deposited metals," *Transaction of American Electrochemical Society*, vol. 40, pp. 307-320, 1921.
- [35] A. Brenner, "Electrodeposition of Alloys: Principles and practice, number v. 1 in electrodeposition of Alloys: Principles and practice," Academic Press Inc., New York, 1963.
- [36] A. Haseeb, J.-P. Celis, and J. Roos, "Dual-Bath electrodeposition of Cu/Ni compositionally modulated multilayers," *Journal of the Electrochemical Society*, vol. 141, no. 1, pp. 230-237, 1994.
- [37] I. Ivanov, T. Valkova, and I. Kirilova, "Corrosion resistance of compositionally modulated Zn-Ni multilayers electrodeposited from dual baths," *Journal of applied electrochemistry*, vol. 32, no. 1, pp. 85-89, 2002.

- [38] G. Barral, and S. Maximovitch, "Preparation of Composition-Modulated Films by Alternate Electrodeposition from Different Electrolytes," *Le Journal de Physique Colloques*, vol. 51, no. C4, pp. C4-291-C4-297, 1990.
- [39] W. Wang, and R. N. Singh, "Fatigue crack growth in a Ni–Sn multilayered composite," *Materials Science and Engineering: A*, vol. 251, no. 1, pp. 184-191, 1998.
- [40] I. Kirilova, and I. Ivanov, "Corrosion behaviour of Zn–Co compositionally modulated multilayers electrodeposited from single and dual baths," *Journal of Applied Electrochemistry*, vol. 29, no. 9, pp. 1133-1137, 1999.
- [41] P. Pascariu *et al.*, "Microstructure, magnetic and magnetoresistance properties of electrodeposited [Co/Zn]<sub>50</sub> multilayers," *Journal of Superconductivity and Novel Magnetism*, vol. 24, no. 6, pp. 1917-1923, 2011.
- [42] Y. Jyoko, S. Kashiwabara, and Y. Hayashi, "Preparation and characterization of electrodeposited Pt/Co multilayers," *Journal of Magnetism and Magnetic Materials*, vol. 156, no. 1, pp. 35-37, 1996.
- [43] S. Esmaili, M. Bahrololoom, and K. Kavanagh, "Electrodeposition, characterization and morphological investigations of NiFe/Cu multilayers prepared by pulsed galvanostatic, dual bath technique," *Materials Characterization*, vol. 62, no. 2, pp. 204-210, 2011.
- [44] K. H. Lee, G. H. Kim, and W. Y. Jeung, "Epitaxial growth and magnetic properties of electrochemically multilayered [CoPtP/Cu]<sub>n</sub> films," *Electrochemistry Communications*, vol. 6, no. 2, pp. 115-119, 2004.
- [45] J.-W. Park, "Core lamination technology for micromachined power inductive components," Ph D. dissertation, Department of Electrical and Computer Engineering, Georgia institute of Technology, Atlanta, GA, USA, 2003.
- [46] M. Chandrasekar, and M. Pushpavanam, "Pulse and pulse reverse plating—Conceptual, advantages and applications," *Electrochimica Acta*, vol. 53, no. 8, pp. 3313-3322, 2008.
- [47] R. M. Haralick, S. R. Sternberg, and X. Zhuang, "Image analysis using mathematical morphology," *IEEE Transactions on Pattern Analysis and Machine Intelligence*, no. 4, pp. 532-550, 1987.
- [48] S. D. Leith, and D. T. Schwartz, "In-situ fabrication of sacrificial layers in electrodeposited NiFe microstructures," *Journal of Micromechanics and Microengineering*, vol. 9, no. 1, pp. 97, 1999.

- [49] S. Arai, T. Hasegawa, and N. Kaneko, "Fabrication of 3-D Ni/Cu multilayered microstructure by selective etching of Ni," *Journal of the Electrochemical Society*, vol. 150, no. 11, pp. C798-C801, 2003.
- [50] A. Armutlulu *et al.*, "A MEMS-enabled 3D zinc-air microbattery with improved discharge characteristics based on a multilayer metallic substructure," *Journal of Micromechanics and Microengineering*, vol. 21, no. 10, pp. 104011, 2011.
- [51] X.-M. Zhao, Y. Xia, and G. M. Whitesides, "Soft lithographic methods for nanofabrication," *Journal of Material Chemistry*, vol. 7, no. 7, pp. 1069-1074, 1997.
- [52] A. Horn *et al.*, "Ordering and printing virus arrays: A straightforward way to functionalize surfaces," *Small*, vol. 6, no. 19, pp. 2122-2125, 2010.
- [53] M. C. McAlpine, R. S. Friedman, and C. M. Lieber, "Nanoimprint lithography for hybrid plastic electronics," *Nano Letters*, vol. 3, no. 4, pp. 443-445, 2003.
- [54] M. Bender *et al.*, "Status and prospects of UV-nanoimprint technology," *Microelectronic Engineering*, vol. 83, no. 4, pp. 827-830, 2006.
- [55] M. Zach *et al.*, "Synthesis of molybdenum nanowires with millimeter-scale lengths using electrochemical step edge decoration," *Chemistry of Materials*, vol. 14, no. 7, pp. 3206-3216, 2002.
- [56] O. Azzaroni, P. Schilardi, and R. Salvarezza, "Metal electrodeposition on self-assembled monolayers: a versatile tool for pattern transfer on metal thin films," *Electrochimica Acta*, vol. 48, no. 20, pp. 3107-3114, 2003.
- [57] M. J. Lee *et al.*, "Antiadhesion Surface Treatments of Molds for High-Resolution Unconventional Lithography," *Advanced Materials*, vol. 18, no. 23, pp. 3115-3119, 2006.
- [58] S. Park *et al.*, "Anti-adhesive layers on nickel stamps for nanoimprint lithography," *Microelectronic Engineering*, vol. 73, pp. 196-201, 2004.
- [59] H. Sun *et al.*, "Anti-sticking treatment for a nanoimprint stamp," *Applied Surface Science*, vol. 254, no. 10, pp. 2955-2959, 2008.
- [60] C.-L. Wu *et al.*, "Anti-adhesion treatment for nanoimprint stamps using atmospheric pressure plasma CVD (APPCVD)," *Applied Surface Science*, vol. 261, pp. 441-446, 2012.
- [61] J. P. Rolland *et al.*, "High-resolution soft lithography: Enabling materials for nanotechnologies," *Angewandte Chemie*, vol. 116, no. 43, pp. 5920-5923, 2004.

- [62] T. W. Odom *et al.*, "Improved pattern transfer in soft lithography using composite stamps," *Langmuir*, vol. 18, no. 13, pp. 5314-5320, 2002.
- [63] A. Marmur, "The lotus effect: superhydrophobicity and metastability," *Langmuir*, vol. 20, no. 9, pp. 3517-3519, 2004.
- [64] X.-Q. Feng *et al.*, "Superior water repellency of water strider legs with hierarchical structures: experiments and analysis," *Langmuir*, vol. 23, no. 9, pp. 4892-4896, 2007.
- [65] Y.-B. Park *et al.*, "Self-cleaning effect of highly water-repellent microshell structures for solar cell applications," *Journal of Materials Chemistry*, vol. 21, no. 3, pp. 633-636, 2011.
- [66] G. Tzeng *et al.*, "The effects of roughening on teflon surfaces," *Surface and Coatings Technology*, vol. 89, no. 1, pp. 108-113, 1997.
- [67] Y. Su *et al.*, "Nano to micro structural hierarchy is crucial for stable superhydrophobic and water-repellent surfaces," *Langmuir*, vol. 26, no. 7, pp. 4984-4989, 2010.
- [68] L. Xu *et al.*, "Transparent, superhydrophobic surfaces from one-step spin coating of hydrophobic nanoparticles," *ACS Applied Materials & Interfaces*, vol. 4, no. 2, pp. 1118-1125, 2012.
- [69] J. Feng, M. T. Tuominen, and J. P. Rothstein, "Hierarchical superhydrophobic surfaces fabricated by dual-scale electron-beam-lithography with well-ordered secondary nanostructures," *Advanced Functional Materials*, vol. 21, no. 19, pp. 3715-3722, 2011.
- [70] T.-H. Kim *et al.*, "Simple and cost-effective fabrication of highly flexible, transparent superhydrophobic films with hierarchical surface design," *ACS Applied Materials & Interfaces*, vol. 7, no. 9, pp. 5289-5295, 2015.
- [71] T. Yasuda, K. Suzuki, and I. Shimoyama, "Automatic transportation of a droplet on a wettability gradient surface," *7<sup>th</sup> International Conference on Minaturized Chemical and Biochemcial Analysis Systems*, pp. 1129-1132. Oct. 2003 (Squaw Valley, CA, USA).
- [72] A. Marmur, "Underwater superhydrophobicity: Theoretical feasibility," *Langmuir*, vol. 22, no. 4, pp. 1400-1402, 2006.
- [73] Y. Lu *et al.*, "Robust self-cleaning surfaces that function when exposed to either air or oil," *Science*, vol. 347, no. 6226, pp. 1132-1135, 2015.

- [74] W. Li, and A. Amirfazli, "A thermodynamic approach for determining the contact angle hysteresis for superhydrophobic surfaces," *Journal of Colloid and Interface Science*, vol. 292, no. 1, pp. 195-201, 2005.
- [75] C. Furnidge, "Studies at phase interfaces. I. The sliding of liquid drops on solid surfaces and a theory for spray retention," *Journal of Colloid Science*, vol. 17, no. 4, pp. 309-324, 1962.
- [76] L. Bewley, and H. Poritsky, "Intersheet eddy-current loss in laminated cores," *Transactions of the American Institute of Electrical Engineers*, vol. 3, no. 56, pp. 344-346, 1937.
- [77] E. Taylor, "The measurement of interlaminar resistance of varnish-insulated silicon-steel sheet for large electrical machines," *Proceedings of the IEE-Part II: Power Engineering*, vol. 98, no. 63, pp. 377-385, 1951.
- [78] Y. W. Zhao, X. Zhang, and J. Q. Xiao, "Submicrometer laminated Fe/SiO<sub>2</sub> soft magnetic composites—An effective route to materials for high-frequency applications," *Advanced Materials*, vol. 17, no. 7, pp. 915-918, 2005.
- [79] J. Qiu, and C. R. Sullivan, "Design and fabrication of VHF tapped power inductors using nanogranular magnetic films," *IEEE Transactions on Power Electronics*, vol. 27, no. 12, pp. 4965-4975, 2012.
- [80] J.-M. Quemper *et al.*, "Permalloy electroplating through photoresist molds," *Sensors and Actuators A: Physical*, vol. 74, no. 1, pp. 1-4, 1999.
- [81] M. A. McClain, M. C. LaPlaca, and M. G. Allen, "Spun-cast micromolding for etchless micropatterning of electrically functional PDMS structures," *Journal of Micromechanics and Microengineering*, vol. 19, no. 10, pp. 107002, 2009.
- [82] Y.-H. Ha *et al.*, "Three-dimensional network photonic crystals via cyclic size reduction/infiltration of sea urchin exoskeleton," *Advanced Materials*, vol. 16, no. 13, pp. 1091-1093, 2004.
- [83] J. P. Barranger, *Hysteresis and eddy-current losses of a transformer lamination viewed as an application of the Poynting theorem*: National Aeronautics and Space Administration, 1965.
- [84] J. Y. Park, "Packaging-compatible micromachined magnetic devices: Integrated passive components and modules," Ph.D. dissertation, Department of Electrical and Computer Engineering, Georgia institute of Technology, Atlanta, GA, USA 1997.



- [85] Y. Han *et al.*, “Evaluation of magnetic materials for very high frequency power applications,” *IEEE Transactions on Power Electronics*, vol. 27, no. 1, pp. 425-435, 2012.
- [86] J. Kim, “Fabrication of nano-laminated soft magnetic metallic alloys through multilayer electrodeposition: Application to high-frequency and high-flux power conversion,” Ph D. dissertation, Department of Electrical and Computer Engineering, Georgia institute of Technology, Atlanta, GA, USA, 2015.
- [87] J. Kim *et al.*, “Electrodeposited nanolaminated CoNiFe Cores for ultracompact DC–DC power conversion,” *IEEE Transactions on Power Electronics*, vol. 30, no. 9, pp. 5078-5087, 2015.
- [88] J. Kim *et al.*, “Anisotropic nanolaminated CoNiFe cores integrated into microinductors for high-frequency dc–dc power conversion,” *Journal of Physics D: Applied Physics*, vol. 48, no. 46, pp. 462001, 2015.
- [89] J. Rodríguez-Carvajal, “Recent advances in magnetic structure determination by neutron powder diffraction,” *Physica B: Condensed Matter*, vol. 192, no. 1, pp. 55-69, 1993.
- [90] J. Kim *et al.*, “Microfabrication of toroidal inductors integrated with nanolaminated ferromagnetic metallic cores,” *Journal of Micromechanics and Microengineering*, vol. 23, no. 11, pp. 114006, 2013.
- [91] K. Chwastek, “Modeling of dynamic hysteresis loops using the Jiles–Atherton approach,” *Mathematical and Computer Modelling of Dynamical Systems*, vol. 15, no. 1, pp. 95-105, 2009.
- [92] M. Kuczmann, and G. Kovacs, “Improvement and application of the viscous-type frequency-dependent Preisach model,” *IEEE Transactions on Magnetics*, vol. 50, no. 2, pp. 385-388, 2014.
- [93] J. Mullenix, A. El-Ghazaly, and S. X. Wang, “Integrated transformers with sputtered laminated magnetic core,” *IEEE Transactions on Magnetics*, vol. 49, no. 7, pp. 4021-4027, 2013.
- [94] D.-X. Chen, E. Pardo, and A. Sanchez, “Demagnetizing factors for rectangular prisms,” *IEEE Transactions on Magnetics*, vol. 41, no. 6, pp. 2077-2088, 2005.
- [95] A. T. Fafarman *et al.*, “Chemically tailored dielectric-to-metal transition for the design of metamaterials from nanoimprinted colloidal nanocrystals,” *Nano Letters*, vol. 13, no. 2, pp. 350-357, 2012.
- [96] Y. C. Jung, and B. Bhushan, “Biomimetic structures for fluid drag reduction in laminar and turbulent flows,” *Journal of Physics: Condensed Matter*, vol. 22, no. 3, pp. 035104, 2010.

- [97] K. Yang *et al.*, “Multiscale, hierarchically patterned topography for directing human neural stem cells into functional neurons,” *ACS Nano*, vol. 8, no. 8, pp. 7809-7822, 2014.